






Universitat Autònoma de Barcelona

ADVERTIMENT. L'accés als continguts d'aquesta tesi queda condicionat a l'acceptació de les condicions d'ús establertes per la següent llicència Creative Commons:  http://cat.creativecommons.org/?page_id=184

ADVERTENCIA. El acceso a los contenidos de esta tesis queda condicionado a la aceptación de las condiciones de uso establecidas por la siguiente licencia Creative Commons:  <http://es.creativecommons.org/blog/licencias/>

WARNING. The access to the contents of this doctoral thesis it is limited to the acceptance of the use conditions set by the following Creative Commons license:  <https://creativecommons.org/licenses/?lang=en>

Thermal Conductivity And Advanced Optical Characterization of PEDOT:PSS Based Films

PhD Thesis

Minghua Kong

2022

Supervisors: Maria Isabel Alonso Carmona

Juan Sebastián Reparaz

Tutor: Maria Isabel Alonso Carmona

PhD program in Materials Science

Department of Physics

Autonomous University of Barcelona



**Universitat Autònoma
de Barcelona**



INSTITUT DE CIÈNCIA DE MATERIALS DE BARCELONA



CSIC
CONSEJO SUPERIOR DE INVESTIGACIONES CIENTÍFICAS

ABSTRACT

Nowadays, more than half of the primary energy of fossil fuels is lost worldwide as waste heat. Effectively recycling such waste heat is helpful to overcome the global energy crisis. Thermoelectrics can directly realize the two-way conversion between electricity and heat and provide a promising approach to solve the energy dilemma. High performance thermoelectric materials require high electrical conductivity (σ) and Seebeck coefficient (S), as well as low thermal conductivity (κ). Compared with organic materials, conventional inorganic materials are typically more efficient for energy conversion due to their high electrical conductivity and Seebeck coefficient, hence, leading to a figure-of-merit, $ZT=S^2\sigma/\kappa$, typically exceeding $ZT=1$. However, their high thermal conductivity, high cost, brittleness and toxicity restrict, in some cases, their further development. Organic materials have attracted substantial attention because of their remarkable advantages, such as intrinsically low thermal conductivity, abundance of raw materials, low weight, convenience to be processed, and structural flexibility.

In the present thesis we provide a comprehensive study on the optical and thermoelectric properties of PEDOT:PSS thin films. In particular, we focus on two relevant aspects: **(i)** the thickness dependent optical and thermal properties of PEDOT:PSS thin films, and **(ii)** the modification of their optical and thermoelectric properties through mixing with ZnO nanocrystals (ZnO NCs) and graphene quantum dots (GQDs).

In **Chapter 1**, we provide a general description on the fundamentals of thermoelectricity, providing the main approximations and equations to describe thermoelectric energy conversion. We also provide the guidelines to optimize the thermoelectric properties to maximize their energy conversion potential.

In **Chapter 2**, we highlight various fabrication methods of PEDOT:PSS films, in particular, we discuss the fabrication process of PEDOT:PSS thin films with a thickness gradient. Moreover, the synthesis procedure of ZnO NCs is reproduced based on previous publications, and the preparation methodology of ZnO NCs/PEDOT:PSS and GQDs/PEDOT:PSS hybrid films is presented. In **Chapter 3** we introduce the basics of the different optical and thermoelectric characterization methods used throughout this thesis.

Chapter 4 presents the optical properties of various PEDOT:PSS films obtained by drop casting and blade coating. All samples were studied using variable angle spectroscopic ellipsometry in the visible-UV spectral range. We discuss several differences observed in the optical spectra arising from different content of PSS, as well as the influence of DMSO treatment. We investigate the optical anisotropy of the complex refractive indices which arises from the in-plane arrangement of the PEDOT backbones and relate it to structural changes detected by Raman scattering. Finally, we have also studied the morphology of

the thin films and established that not only local structural changes of the chain conformation are significant in the interpretation of Raman spectra, but also the overall morphology of the composite films.

In **Chapter 5**, we focus on the optical and thermal properties of blade-coated PEDOT:PSS thin films. In order to tune the thermal conductivity of the PEDOT:PSS films, two strategies were adopted: **(i)** To fabricate thickness dependent PEDOT:PSS films. We studied samples with thickness gradients deposited on glass microscope slides, where the thickness of the PEDOT:PSS thin film changes along the deposition direction. We show that the thermal conductivity of PEDOT:PSS (AI 4083) films decreases remarkably by increasing the film thickness, which originates in the change in conjugated lengths distribution. **(ii)** To blend PEDOT:PSS with ZnO NCs and GQDs. We address the influence of the concentration of nanoparticles on the thermal conductivity.

Furthermore, we investigated the optical properties of PEDOT:PSS thin films blended with dispersed ZnO NCs and GQDs using spectroscopic ellipsometry. The data is analyzed within the framework of the Drude approximation, where the fitted parameters obtained from the Drude model provide further insights on the influence of nanoparticle concentration on the electrical properties. As the nanoparticle concentration increases, we observe the rising polaron band and the concomitant decreasing bipolaron concentration, indicating the dedoping of PEDOT chains. In addition, Bruggeman effective medium approximation model was also used to fit the relative volume ratio of the components of GQDs/PEDOT:PSS films.

Contents

ABSTRACT	i
I. Introduction	1
1.1 Overview	1
1.2 Figure of merit (ZT) and Carnot efficiency (η_{\max}).....	2
1.3 Seebeck coefficient (S)	4
1.4 Electrical conductivity (σ)	6
1.5 Thermal conductivity (κ)	7
1.6 Strategies to optimize TE properties.....	10
1.7 π -conjugated polymer: PEDOT:PSS.....	11
II. Material Synthesis and Samples Fabrication	15
2.1 Thick films: drop casting	15
2.2 Thin films: spin coating and blade coating	17
2.3 Thickness gradient in thin films	19
2.4 ZnO nanocrystals and nanowires synthesis	21
2.5 Fabrication of hybrid films: ZnO NCs/PEDOT:PSS and GQDs/PEDOT:PSS.....	23
2.6 Phase-separated films	25
2.7 Suspended PEDOT thin films.....	26
III. Experimental Characterization Techniques	29
3.1 Surface characterization methods.....	29
3.2 Optical characterization.....	32
3.2.1 Spectroscopic ellipsometry.....	32
3.2.2 Raman spectroscopy.....	37
3.3 Thermal characterization: frequency-domain thermoreflectance technique	39
3.4 Electrical determination methods (σ , S)	42
3.4.1 Van der Pauw method	42
3.4.2 A custom setup for σ	43
IV. Advanced Optical Characterization of PEDOT:PSS Thin Films	45
4.1 State of the art.....	45
4.2 Ellipsometry data fitting.....	46
4.3 Interpretation of Raman spectra.....	50

4.4 Spectroscopic results and discussion.....	53
4.4.1 Dependence with PSS content.....	53
4.4.2 Effect of DMSO addition	55
4.5 Conclusions	57
V. Thermal and Optical Properties of PEDOT:PSS Based Films.....	59
5.1 State of the art.....	59
5.2 Thermal conductivity of PEDOT:PSS thin films with thickness gradients	61
5.3 Characterization of ZnO nanocrystals and nanowires	66
5.4 Optical properties of ZnO/PEDOT:PSS hybrid thin films.....	68
5.5 Thermal conductivity of ZnO/PEDOT:PSS hybrid thin films	73
5.6 Optical properties of GQDs/PEDOT:PSS hybrid thin films	80
5.7 Thermal conductivity of GQDs/PEDOT:PSS hybrid thin films	85
5.8 Conclusions	91
Conclusions & Outlook.....	93
References.....	95
List of Abbreviations	105
List of Figures.....	106
List of Tables.....	109
Publications	110
Conference Presentations.....	110
Acknowledgements	111

I. Introduction

1.1 Overview

Currently, global energy consumption mainly depends on the contribution of fossil fuels. However, fossil fuels emit greenhouse gases during combustion process, leading to global warming and variable environmental problems. According to related statistics, fossil fuels will run out in a few decades on current trends¹. Human beings are facing a very urgent demand for clean and renewable energy under the background of energy crisis and global warming. In the last few decades, many efforts have been made to explore and develop alternatives and varied forms of renewable energy sources have attracted people's attention, such as solar, wind and hydropower, etc. Among these sustainable energy sources, thermoelectricity can directly realize the two-way conversion between electricity and heat with zero pollution, which provides a promising way to solve the energy dilemma.

Thermoelectric generators (TEGs) convert heat into electricity through the Seebeck effect, and work without moving parts and are free of noise and vibrations. Compared with traditional heat-electricity conversion, TEGs are resource-saving and environment-friendly. If used in the reverse direction, thermoelectric (TE) systems can also convert electricity into thermal energy for cooling or heating through the Peltier effect. For example, TE refrigerators use no refrigerants and may be expected to produce negligible emissions of greenhouse gases.

In principle, TE devices can use any heat source such as waste heat, which is a common heat source that is present in almost all mechanical and thermal processes, including heated water or gas released to the environment, heat equipment surfaces and heated products, etc². However, in general, the heat sources of TEGs are various. For example, solar energy is concentrated to create heat in solar thermoelectric generators (STEGs). Moreover, the heat source of radioisotope thermoelectric generators (RTGs) is from the nuclear decay of the radioisotope. RTGs are used in remote power supply, such as space or deep ocean explorations³. Furthermore, wearable/implantable TEGs use human body as the heat source to provide health support. There are still many other heat sources that TEGs can utilize.

All these features make TE materials gain lots of research attention. Herein, we are first going to introduce key parameters and equations about TE materials.

1.2 Figure of merit (ZT) and Carnot efficiency (η_{\max})

The performance of TE energy conversion is typically given by the dimensionless figure of merit (ZT), which indicates the potential of a material to convert heat into electricity and it is expressed as:

$$ZT = \frac{S^2 \sigma T}{\kappa} \quad (1.1)$$

where S is the Seebeck coefficient, σ is the electrical conductivity, κ is the thermal conductivity, and T is the average temperature between the hot (T_{hot}) and cold (T_{cold}) temperature poles and it is given by $T_{ave} = (T_{hot} + T_{cold})/2$. Note that within the previous definition, the values of σ and κ must be projected into the same direction (σ_{\parallel} and κ_{\parallel} , σ_{\perp} and κ_{\perp}), which becomes especially relevant for anisotropic materials, where σ and κ are represented by a tensor rather than by a scalar (isotropic media). As shown by Eq. (1.1), ZT is determined by three material parameters (σ , κ and S) which can be optimized to enhance the performance of the TE material. Hence, the strategy that is typically followed to enhance the ZT, is to seek for a maximum of $S^2\sigma$ (power factor) and a minimum κ . However, these three parameters are strongly interconnected, e.g., an increase in σ typically leads to lower values of S . Furthermore, in the high doping regime σ and κ are proportional according to the Wiedemann-Franz law, i.e., larger values of σ lead to larger values of κ .

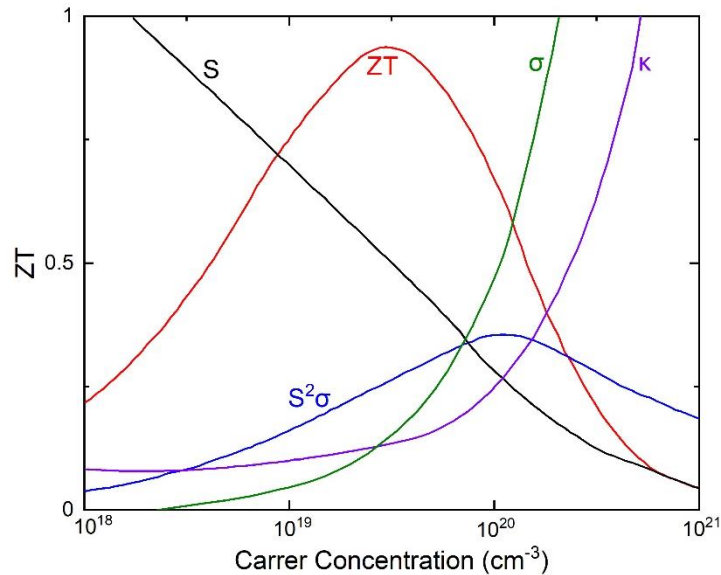


Figure 1.1 TE parameters as a function of carrier concentration. The curves shown here were obtained by numerical modelling of Bi_2Te_3 . (Reproduced from the references⁴⁻⁷)

Figure 1.1⁴⁻⁷ qualitatively illustrates how σ , S , and κ depend on the carrier concentration. In addition, the figure also displays the resultant $PF=S^2\sigma$ and the ZT as a function of σ . As can be seen from this figure, increasing carrier concentration leads to larger values for σ and κ , with a corresponding decrease of S . Hence, maximizing ZT is achieved through a suitable compromise between σ , S and κ . However, optimizing the properties of a material to obtain maximum thermoelectric conversion efficiency still presents significant challenges due to the strong coupling between σ , S , and κ ^{8,9}. In fact, this is evidenced by the different values of σ , corresponding to the maxima of $ZT(\sigma)$ and $PF(\sigma)$ as displayed in Figure 1.1.

The energy conversion efficiency of thermoelectric materials can be expressed as:^{3,10,11}

$$\eta_p = \frac{T_h - T_c}{T_h} \left[\frac{\sqrt{1 + ZT_{ave}} - 1}{\sqrt{1 + ZT_{ave}} + T_c/T_h} \right] \quad (1.2)$$

$$\eta_c = \frac{T_c}{T_h - T_c} \left[\frac{\sqrt{1 + ZT_{ave}} - T_h/T_c}{\sqrt{1 + ZT_{ave}} + 1} \right] \quad (1.3)$$

Here, η_p represents the power generation efficiency, η_c is the refrigeration efficiency, $(T_h - T_c)/T_h$ is the maximum efficiency (Carnot efficiency), T_c is the absolute temperature of the cold pole, T_h is the absolute temperature of the hot pole, ZT_{ave} is the average ZT of the n-type and p-type legs. Since the properties of each material depend on temperature, the average ZT is defined through integration of the temperature as follows:¹²

$$ZT_{ave} = \frac{1}{T_h - T_c} \int_{T_c}^{T_h} ZT(T) dT \quad (1.4)$$

We recall that the Carnot cycle is a theoretical ideal thermodynamic cycle proposed by Sadi Carnot in 1824. The Carnot efficiency illustrates the maximum thermal efficiency that a heat engine can achieve as permitted by the second law of thermodynamics, and it is expressed as follows:

$$\eta_{max} = 1 - \frac{T_c}{T_h} \quad (1.5)$$

As can be seen from Eq. (1.2) and Eq. (1.3), the efficiency of TE devices is closely related to ZT_{ave} and the temperature difference between the hot and cold poles. As shown in Figure 1.2^{9,11,13-15}, a higher ZT_{ave} and a larger temperature difference are needed to generate higher power generation efficiency. Apart from this, when ZT_{ave} is less than or equal to 1, the power generation efficiency is always lower than 10% even for temperature differences of up to 125 K.

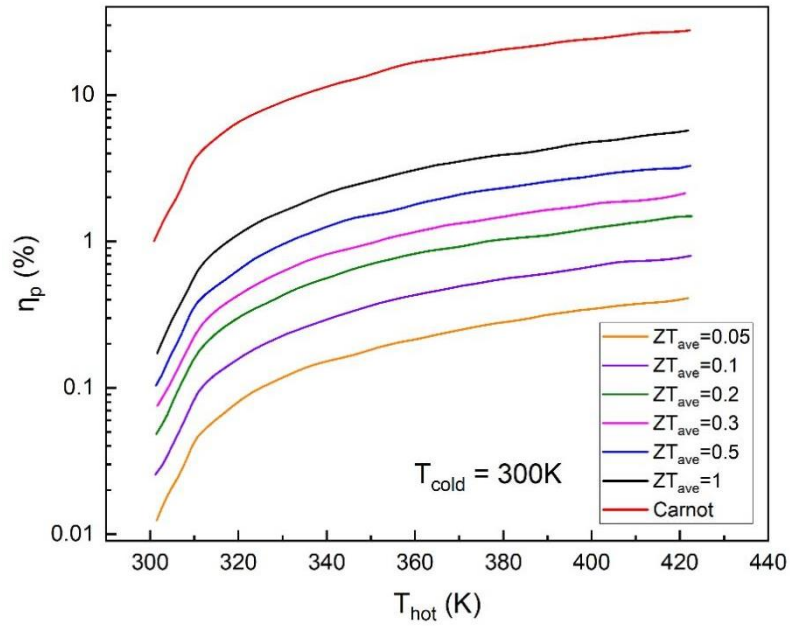


Figure 1.2 Power generation efficiency as functions of temperature of the hot end and ZT_{ave} . The top curve shows the Carnot efficiency. The other six curves represent power generation efficiency under different ZT_{ave} . The temperature of the cold pole is constant at 300 K. (Extracted from references^{9,11,13-15})

Finally, we point out that current available TE devices are still not widely used, partly due to their rather low efficiency¹¹. Practically, currently available TE materials exhibit a maximum conversion efficiency of 5%~20%¹⁴. Applications of TE materials have been limited to narrow fields requiring low powers, e.g., wearable devices. Therefore, it is critical to synthesize TE materials with higher ZT, in order to promote their practical application. In fact, for ideal TE materials, the ZT should be equal to or larger than 1 to obtain a conversion efficiency >10%¹⁴. However, in order to compete with other renewable energy sources, the TE material should have $ZT > 4$ ^{5,16}, which is still larger than current accepted values.

1.3 Seebeck coefficient (S)

The Seebeck effect was discovered in 1821 by Thomas Johann Seebeck. An applied temperature difference between two ends of a semiconductor results in a voltage difference between these two ends. Specifically, as displayed in Figure 1.3, a simple power generator consists of two heavily doped semiconductor legs which are connected electrically in series and thermally in parallel^{17,18}. These two semiconductors are n-type and p-type, respectively. One side of each semiconductor is connected to a heat source,

and the other side to a colder heat sink. Charge carriers (electrons or holes) at the hot ends have higher energy, i.e. carriers at the hot ends are more active than those at the cold ends. Therefore, on average, more carriers will flow from the hot ends to the cold ends, which generates a voltage difference. It is worth noting that if both semiconductors were of the same type (both n-type or both p-type), there would be no current flowing in the circuit, since the equal and opposite voltages would cancel out. In other words, a measurable Seebeck effect only takes place in two leads of two distinct materials. For identical materials, no Seebeck voltage would be measured in the complete circuit⁵.

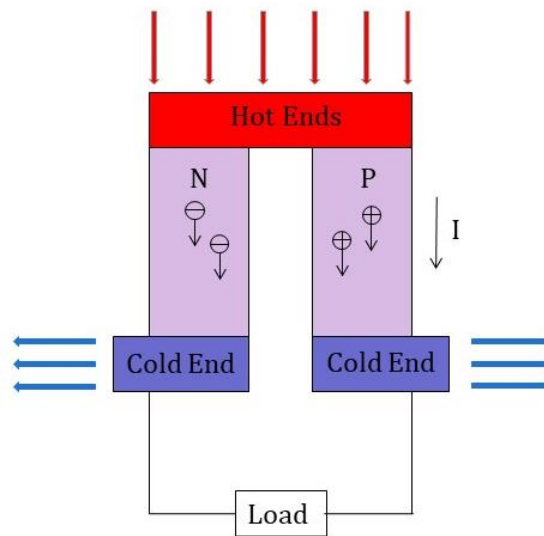


Figure 1.3 Schematic of the Seebeck effect. An applied temperature difference induces electrons and holes in two different semiconductors (pink) to diffuse from the hot side (red) to the cold side (blue), resulting in current flowing through the circuit.

The Seebeck coefficient quantifies the magnitude of Seebeck effect and it is also called thermopower. The thermopower is defined as the ratio of the voltage difference ΔV and temperature difference ΔT , where the voltage difference is caused by a temperature difference. The Seebeck coefficient is expressed as follows:

$$S = \frac{\Delta V}{\Delta T} \quad (1.6)$$

The sign of the Seebeck coefficient depends on the charge of majority carriers. For $S > 0$, which implies a p-type material, the majority of moving charges are holes. On the contrary, for $S < 0$, the material is n-type and electrons are the majority carriers.

For the case of degenerate semiconductors, the Seebeck coefficient can be expressed in terms of DOS effective mass¹⁹⁻²².

$$S = \frac{8\pi^2 k_B^2}{3qh^2} m^* T \left(\frac{\pi}{3n}\right)^{2/3} \quad (1.7)$$

where k_B is the Boltzmann constant, q is carrier charge, h is the Planck constant, m^* is the effective mass, T is the temperature, and n is the carrier concentration. As is evident from Eq. (1.7), S strongly depends on m^* and n .

Typical values of the Seebeck coefficient for metals, semiconductors, and insulators are ~ 5 , ~ 200 , and $1000 \mu\text{V/K}$, respectively²². We note that an ideal TE material should exhibit a large Seebeck coefficient ($>200 \mu\text{V/K}$)¹⁴, hence, indicating a large voltage-generation ability with its corresponding power production.

1.4 Electrical conductivity (σ)

The “Drude model” of electrical conduction was proposed in 1900 by Paul Drude to explain how a metal or heavily doped semiconductor responds to an externally applied uniform electric field E ²³. It assumes that the microscopic behavior of electrons in materials looks like a pinball machine, and electrons are scattered randomly by immobile positive ions as shown in Figure 1.4. Additionally, the electrons move in straight lines, and do not interact with each other or positive ions. The only possible interaction of a free electron with its surrounding environment is via instantaneous collisions.

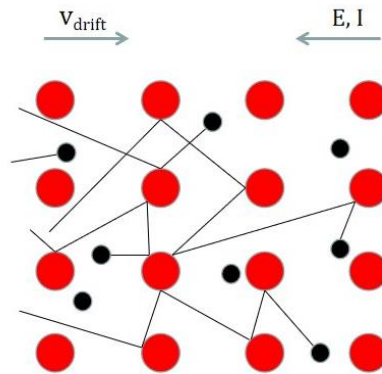


Figure 1.4 Schematic diagram of Drude model. Electrons (black point) move in straight lines and constantly bounce between heavier, stationary crystal ions (red).

Drude model gives the average drift velocity of electron. $v_{drift} = \frac{qE}{m} \tau$

After deduction, the following formulas are obtained.

$$\text{Carrier mobility: } u = \frac{|v_{drift}|}{E} = \frac{q\tau}{m} \quad (1.8)$$

$$\text{Electrical Conductivity: } \sigma = nuq \quad (1.9)$$

where q is carrier charge, m is effective mass, v_{drift} is average drift velocity of electron, E is electric field intensity, τ is average time between collisions, n is carrier concentration. As can be seen from Eq. (1.9), higher carrier concentration and mobility lead to higher electrical conductivity. On the other hand, note that the Seebeck coefficient decreases with increasing carrier concentration, and increases for larger effective mass as seen from Eq. (1.7).

For metals, the carrier concentration does not change much with temperature. Nevertheless, as temperature increases collisions happen more often, and the average time between collisions decreases. According to Eq. (1.8), the carrier mobility shows the same decreasing trend with the average collision time, consequently, the electrical conductivity decreases with increasing temperature. For semiconductors, increasing temperature promotes electrons into the conduction band, which leads to a larger carrier concentration. In this case, the electrical conductivity is mainly governed by the carrier concentration and increases exponentially²⁴. In fact, the temperature dependence of electrical conductivity is rather complex and it is also affected by other factors, such as lattice vibrations, impurity scattering, etc.

The electrical conductivity and its inverse, i.e., the electrical resistivity, are key parameters which define the performance of TE materials. For samples with regular shapes, the electrical conductivity can be calculated from their resistance and geometric dimensions as follows.

$$\sigma = \frac{1}{\rho} = \frac{1}{\frac{RS}{l}} = \frac{l}{RS} \quad (1.10)$$

where R is resistance, S is cross-sectional area, l is material length, ρ is electrical resistivity. Note that whereas the electrical conductivity and electrical resistivity are intrinsic material properties, the electrical resistance and conductance depend on the geometry of the samples²⁵.

1.5 Thermal conductivity (κ)

Heat transport in materials is generally understood and modelled through three main heat transport mechanisms: conduction, convection, and radiation. Conduction is the most significant heat transport mechanism for solids, or between solid objects in thermal contact. Heat conduction occurs when two objects at different temperatures are in direct contact with each other. Heat flows from a hot to a cold end until reaching

thermal equilibrium, i.e., the same temperature. Typically, solids are better heat conductors as compared to liquids, and liquids are better conductors than gases.

The heat conduction law, also known as Fourier's law, is an empirical equation which was first proposed in 1822 by Fourier who concluded that "the heat flux resulting from thermal conduction is proportional to the magnitude of the temperature gradient and opposite to it in sign". Its differential form can be expressed as:

$$\vec{q} = -\kappa \cdot \nabla T \quad (1.11)$$

where \vec{q} is the heat flux density vector, ∇T is the temperature gradient in the direction of heat flow, and the proportionality constant κ is the thermal conductivity. We note that within this approximation, the heat flow direction is normal to isothermal planes. Furthermore, negative sign in this equation indicates that the heat flows in the opposite direction of the temperature gradient.

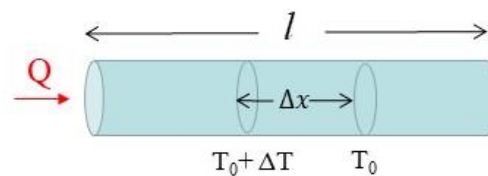


Figure 1.5 Heat flow in a uniform cylinder along its length direction. The total length of the cylinder is l . Thin slice with the length of Δx is studied.

Fourier's law in its one-dimensional form is written as follows:

$$q_x = -\kappa \frac{dT}{dx} \quad (1.12)$$

and its integral form is:

$$\frac{\partial Q}{\partial t} = -\kappa A \frac{\Delta T}{\Delta x} \quad (1.13)$$

In Eq. (1.12) and (1.13), q_x is heat flux density in x-direction, κ is the thermal conductivity, dT/dx is temperature gradient along x-direction, $\partial Q/\partial t$ is the heat flux transferred per unit time, A is the cross-sectional area, ΔT is the temperature difference between two ends, Δx is the distance between two ends.

Fourier's law provides the empirical definition of the thermal conductivity and becomes the basis of many methods for determining the thermal conductivity. Combining Fourier's law with the principle of conservation of energy, leads to the well-known diffusive heat equation, also known as the parabolic heat equation:

$$\frac{\partial T}{\partial t} = D \frac{\partial^2 T}{\partial x^2} \quad (1.14)$$

where $D = \kappa/\rho C_v$ is thermal diffusivity, C_v is the specific heat capacity, and ρ is the density of the material. The previous partial differential equation (1.14) describes how the temperature field evolves over time in a one-dimensional solid medium. It is valid for a uniform medium with temperature gradient lying along the length direction as illustrated in Figure 1.5.

The **thermal conductivity** is the property of a material which describes how efficiently it transports heat, and it is given by a tensor in an anisotropic solid. The thermal conductivity of bulk polymers is usually very low and in the range, 0.1-0.5 W/(m·K)²⁶. In general, the thermal conductivity is the most difficult parameter to measure among the three key parameters which define the ZT of a TE material. In a TE material, the thermal conductivity consists of two contributions²⁷: (i) electrons and holes (κ_e), and (ii) phonons or lattices vibrations (κ_l):

$$\kappa = \kappa_e + \kappa_l \quad (1.15)$$

The electronic contribution to the thermal conductivity, κ_e , is proportional to the electrical conductivity (σ) and it is computed through the Wiedemann-Franz law:

$$\kappa_e = L\sigma T \quad (1.16)$$

where L is Lorenz constant (2.45×10^{-8} V²K⁻² for metals and 1.5×10^{-8} V²K⁻² for non-degenerate semiconductors¹⁴), and it varies with carrier concentration²⁸. As shown by the Wiedemann-Franz law, the electronic part of thermal conductivity is proportional to electrical conductivity, which reveals an inherent conflict for achieving high ZT. Additionally, for metals and inorganic materials with high electrical conductivity, κ_e is much greater than κ_l , hence, dominating κ

The lattice thermal conductivity within the Debye model and the single model relaxation time approximation (RTA) is given by²⁹:

$$\kappa_l = \frac{1}{3} C_v v_s \lambda_{ph} \quad (1.17)$$

where C_v is the specific heat capacity, v_s is the propagation velocity. λ_{ph} is the phonon mean free path, and it is commonly defined as $\lambda_{ph} = v_s \tau$, where τ is the average relaxation time of the thermal phonons.

1.6 Strategies to optimize TE properties

Herein, we introduce the classical strategy to enhance ZT, which is based on the concept of a phonon-glass/electron-crystal (**PGEC**) as originally proposed by Slack³⁰ and discussed in detail by Nolas³¹ and Cahill³². The electron-crystal requirement originates from the fact that crystalline semiconductors have shown to be the best candidates at meeting the compromises required to maximize ZT through the power factor⁴, $PF=S^2\sigma$. The phonon-glass requirement stems from the fact that amorphous glasses exhibit very low lattice thermal conductivity and, hence, also contribute to maximize the ZT. The PGEC concept sets the design rules for ideal TE materials, and has become the general guideline for the design and fabrication of TE materials.

Some **alloy** materials are good examples of TE materials that meet the principles of PGEC^{33,34}. The guest atom in alloy material acts as a scattering center, which reduces the lattice thermal conductivity and enhances the electrical properties¹⁴. Thus, alloying is an effective strategy to achieve high ZT. For example, Liu *et al.* have shown that alloying has a significant influence on the band gap and ultimately on the Seebeck coefficient³⁵, and Nolas *et al.* proposed that the guest atoms act as “rattlers”, which are efficient scattering centers for phonons³³.

Doping is another extensively adopted approach to improve TE performance of materials. A heavily doped semiconductor exhibits a higher power factor than its undoped counterpart^{14,36}. Generally, doping boosts carrier concentration and, hence, enhances the electrical properties. Especially, doping engineering has been widely used to tune the poor electrical performance of organic semiconductors^{9,37}.

Nanostructured materials (nanowires, nanotubes, superlattices, etc) are known to be advantageous in enhancing ZT. Quantum confinement and the energy-filtering effect play key roles when particles size is small enough^{14,38,39}. In this case, increasing the density of states leads to a higher Seebeck coefficient, eventually increasing power factor^{14,28}. Moreover, the thermal conductivity of nanostructured materials is decreased via phonon scattering from interfaces and surfaces^{21,40}.

Nanocomposite is a multiphase material that incorporates nanosized particles into a matrix of a standard material⁴¹. The properties of nanocomposites rely not only on their individual properties, but also on their morphology and interfacial characteristics^{42,43}. Especially, organic/inorganic nanofiller composites attract much research attention because organics have low thermal conductivity and inorganic nanofillers show good electrical properties. On the other hand, strong phonon scattering takes place at the interfaces, which is generally believed to be the main reason of improving the TE properties of nanocomposites¹⁸.

1.7 π -conjugated polymer: PEDOT:PSS

Organic TE materials attract people's attention because of their remarkable advantages, such as abundance of raw materials, low cost, convenience to be processed and flexibility⁴⁴⁻⁴⁶. Most importantly, organic materials have low thermal conductivity, and are good candidates for TEs. However, they exhibit poor electrical properties which have limited their application to thermoelectricity. Anyway, the thermoelectric performance of organic TE materials can be improved further by doping with highly conductive inorganic fillers.

Conjugated polymers are organic macromolecules with alternating double- and single-bonds in the backbone chains. The carbon-carbon single bond is a σ bond, whereas the carbon-carbon double bond consists of a σ bond and a π bond. The overlapping p-orbitals create delocalized π -electrons in the molecular skeleton, leading to interesting and useful optical and electronic properties at macroscopic scales.

Poly(3,4-ethylenedioxythiophene) (PEDOT), as one of the most extensively studied π -conjugated polymers, is well known for its high conductivity, transparency in the visible, environmental stability and solution processability by doping with polystyrene sulfonate (PSS). Based on these properties, PEDOT:PSS is widely used in energy conversion and storage devices⁴⁷. Most commonly, PEDOT:PSS acts as the electrode layer of solar cells.

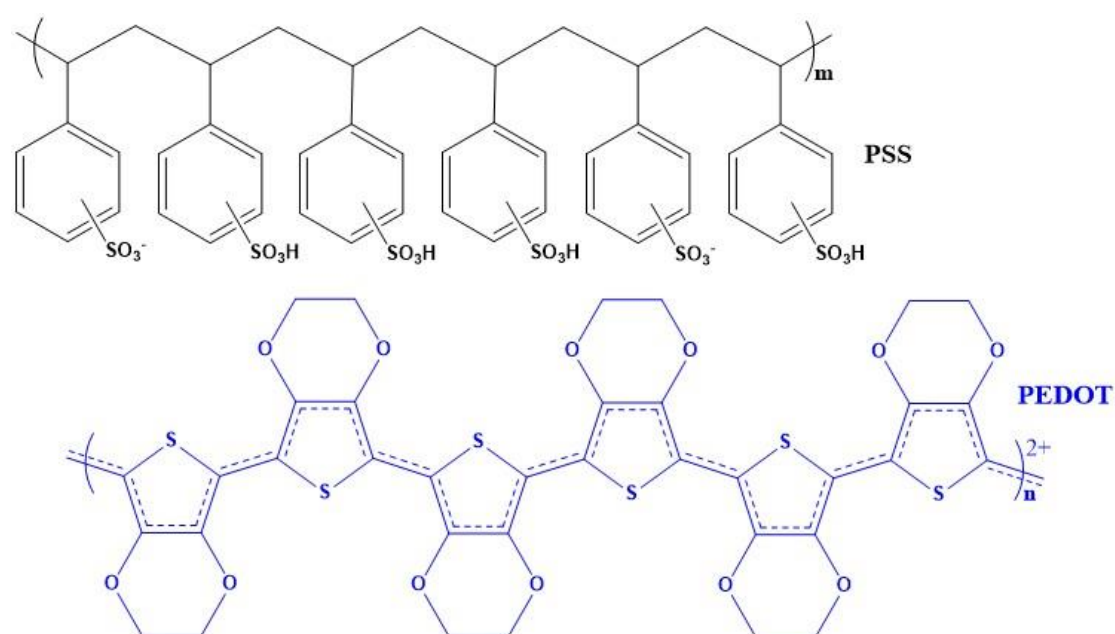


Figure 1.6 Chemical structure of PEDOT:PSS with a doping level of about 0.33.

PEDOT:PSS dispersions are prepared via polymerizing EDOT monomers chemically or electrochemically in aqueous solution in the presence of polyanion PSS. The hydrophilic PSS forms water-soluble polyelectrolyte complexes with the insoluble PEDOT. The chemical structure of PEDOT:PSS is given in Fig. 1.6. The oxidation level of pristine (polymerized) PEDOT is around 33%, i.e., one positive charge for every three EDOT monomer units⁴⁸⁻⁵¹. In this system, PSS functions both as the dopant and stabilizer for PEDOT^{49,51,52}. A certain amount of PSS provides negative charges to balance the positive charges of PEDOT, however, excessive PSS (also called free PSS) keeps the PEDOT:PSS complex dispersible in water.

In some cases, the electrical transport of PEDOT:PSS films is connected with their morphology^{53,54}. It is widely accepted that the well-conducting PEDOT-rich grains are surrounded by the non-conductive PSS matrix^{55,56}. In other words, the PEDOT:PSS system exhibits a core-shell structure^{54,57,58}.

The charge carriers in polythiophenes and its derivatives are polarons and bipolarons⁵⁹. Polarons and bipolarons represent singly and doubly charged quasiparticles, respectively, that are localized along the polymer chains due to strong electron–phonon coupling⁶⁰. The localized charge and its induced lattice distortion is called polaron or bipolaron. PEDOT, one of the polythiophene derivatives, is typically p-doped, so the polarons and bipolarons in PEDOT represent positively charged “hole” quasiparticles. The chemical structure of polarons and bipolarons in PEDOT chain are represented in Fig. 1.7. Generally, the charge carriers in lightly and moderately doped states are polarons, and bipolarons become the dominant charge carriers in heavily doped state^{61,62}. Interestingly, since PEDOT:PSS is heavily doped⁶⁰, the charge carriers in pristine PEDOT:PSS are most likely bipolarons.

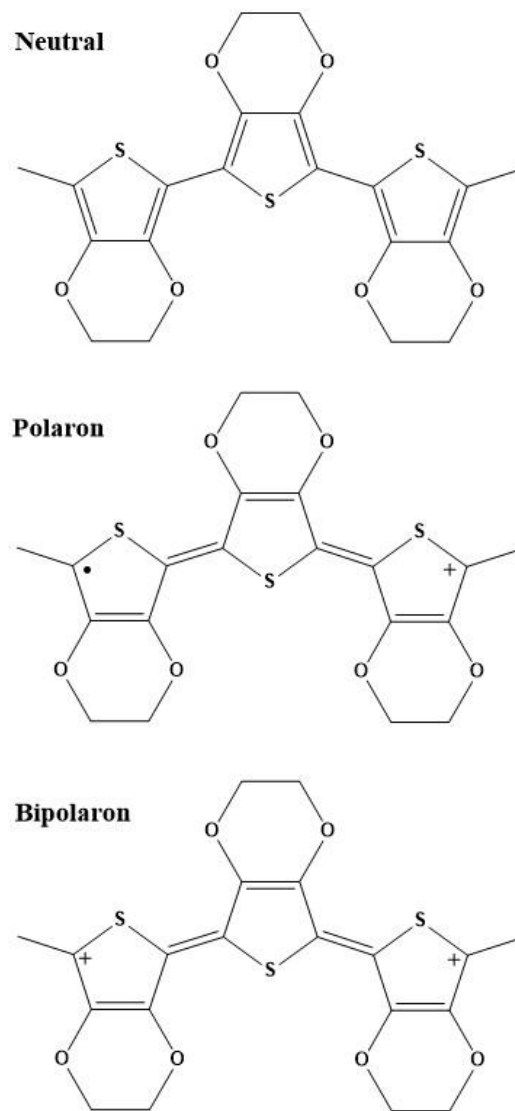


Figure 1.7 Chemical structure of neutral and doped PEDOT units.

II. Material Synthesis and Samples Fabrication

Reagents and equipment used in this chapter are compiled in Table 2.1. Here, material synthesis and samples fabrication methods will be introduced.

2.1 Thick films: drop casting

We used commercial glass microscope slides as substrates. Prior to film deposition, the glass substrates were ultrasonically cleaned for 15 min in soap, acetone, and isopropanol (IPA), successively. Subsequently, the substrates were transferred into an UV ozone cleaner device for longer than 30 min to improve their wettability. The substrates were used as soon as possible once they were taken out from the UV ozone cleaner.

Bulk PEDOT:PSS films were fabricated by drop casting onto the previously prepared glass substrates inside a fume hood. The water evaporation speed in the fume hood was relatively fast due to the drying effect of continuous air flow. The glass slide was cut into three pieces, and the size of each piece was around 2.5 cm × 2.5 cm. Prior to the drop casting process, the PEDOT:PSS aqueous solution was filtered by a syringe filter (PTFE membrane, 0.22 μm pore-size) to remove the larger particles. As Figure 2.1 displays, the films were prepared by drop casting 400 μL of the PEDOT:PSS solution onto a pre-cleaned glass substrate. The as-cast films were then placed on a hot plate to drive off the excess solvent, with the hotplate temperature incrementally increased from 30 to 60 °C in 10 °C intervals (10 min each). The final thermal step at 60 °C lasted 5 min, after which a dried PEDOT:PSS film was obtained. Finally, the samples were removed from the hot plate to avoid cracks due to excessive heating. A drop-cast bulk film is displayed in Figure 2.2.

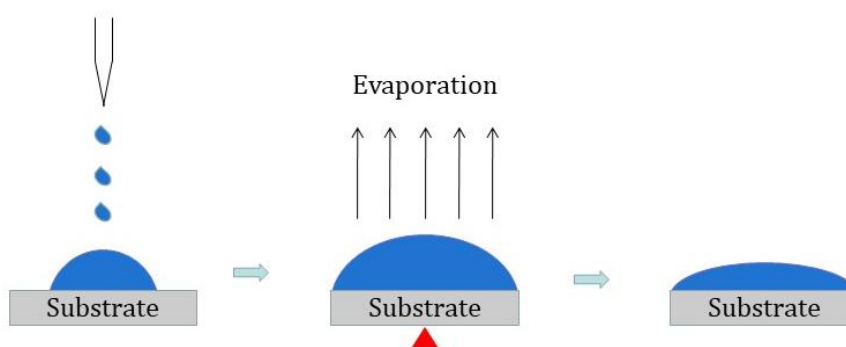


Figure 2.1 Schematic illustration of the drop casting process. The droplets spread out covering the whole substrate and the solvent evaporates at controlled temperature.

Table 2.1 Reagents and equipment in Chapter 2

Name	Specifications
PEDOT:PSS Solution	Heraeus Clevious™ AI 4083. PEDOT:PSS=1:6; Resistivity=500-5000 Ω.cm; Solid content: 1.3-1.7 wt.% in water
PEDOT:PSS Solution	Sigma-Aldrich 483095. PEDOT:PSS=1:1.6; Resistivity=1 Ω.cm; Solid content: 1.3 wt.% in water
PEDOT:X toluene Solution	Heraeus Clevious™ HTL Solar 3. PEDOT:X=N/A; Resistivity=5-500 Ω.cm; Solid content: 1.5-2.5 wt.% in toluene
Detergent	Soap-068-5K0. Dilute with water. Volume Fraction: 75%
Acetone	99.6%
Isopropanol	99.9%
DMSO	Sigma-Aldrich 472301
PSSNa	Aldrich 434574
Sodium Hydroxide	>98% Labkem
Methanol	99.8% Sigma-Aldrich
Zinc Acetate Dihydrate	>99.0% Honeywell Fluka
Zinc Nitrate Hydrate	99% Alfa Aesar
Methanamine	>99.0% Alfa Aesar
Graphene quantum dots	Sigma-Aldrich 900726
Milli-Q water	18.2 MΩ.cm at 25 °C
PTFE Syringe Filters	Labbox SFPT-122-100. Pore: 0.22 μm; Hydrophobic
Glass slides	Labbox, 26 mm×76 mm
Blade Coater	Procep ZEHNTNER ZAA 2300
Spin Coater	SPS POLOS 150i
UV Ozone Cleaner	Model NO. 42-220. Jelight Company
Sonicator	Branson 2800
Hot Plate	IKA C-MAG HS 7
PTFE Filter Paper	Pore: 0.1 μm; Diameter: 47 mm
Thermocouple	IKA™ ETS-D6

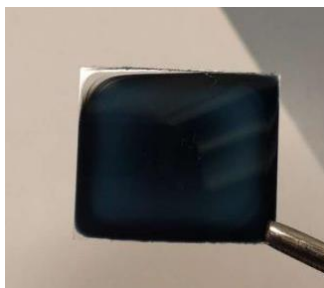


Figure 2.2 Photograph of a drop-cast PEDOT:PSS (AI 4083) film on a glass substrate.

2.2 Thin films: spin coating and blade coating

Thin PEDOT:PSS films were fabricated by spin coating and blade coating. We studied two different formulations of PEDOT:PSS purchased from Sigma-Aldrich 483095 and Heraeus AI 4083. The main difference between these formulations is their electrical conductivity, with values around 1 S/cm and 0.0002-0.002 S/cm for the PEDOT:PSS from Sigma-Aldrich 483095 and Heraeus AI 4083, respectively. Note that the different electrical conductivity of these formulations arises from the different PEDOT to PSS ratio (1:1.6 for Sigma Aldrich, and 1:6 for Heraeus).

We used the same methods as those described in section 2.1 to clean all the glass substrates, and to filter the PEDOT:PSS solutions. A filtered PEDOT:PSS from Sigma-Aldrich 483095 solution with a dispersion content of 1.3% in water was used to fabricate thin films without mixing with IPA. On the other hand, the filtered PEDOT:PSS solution from Heraeus AI 4083 with a dispersion content of 1.3-1.7% in water was mixed with IPA at a volume ratio of 1:2. The IPA-mixed PEDOT:PSS aqueous solution was stirred for 1 h prior to coating.

Spin coating is a common technique for fabricating thin films on flat substrates. The substrate is mounted on a rotary chuck, and the centrifugal force drives the liquid radially outward. The centrifugal force and the surface tension of the liquid create a relatively uniform surface covering during high speed rotation. The higher the spinning speed is, the thinner the film will be. The two main factors affecting film thickness are the spin speed and the viscosity of the solution. Spin coating is an excellent technique at laboratory scale to produce uniform thin films, while its disadvantage is the difficulty with large area samples. The PEDOT:PSS layers deposited onto the glass substrates were coated at a spin rate of 2000 rpm for 90 s. Figure 2.3 illustrates the spin coating process of a PEDOT:PSS thin film.

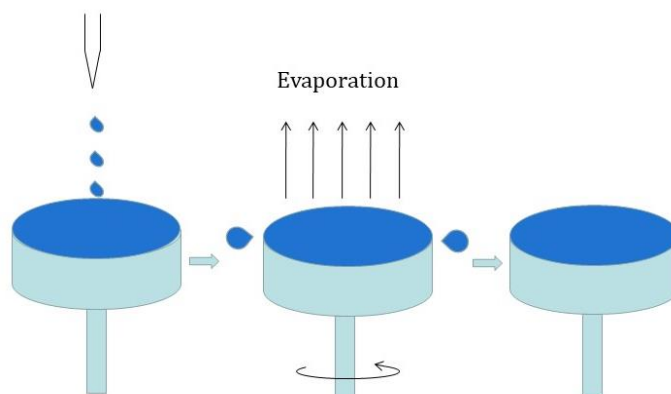


Figure 2.3 Schematic diagram of static dispense spin coating process.

Compared with spin coating, blade coating can deposit thin films with larger area. Filtered PEDOT:PSS solutions with or without co-solvent addition were blade coated on glass substrates. PEDOT:PSS (AI 4083) films were deposited at a blade speed of 90 mm/s at 65 °C. PEDOT:PSS (Aldrich 483095) films were deposited at a blade speed of 70 mm/s at 110 °C. After that, all films were annealed at 120 °C on a hot plate for 15 min. The complete fabrication process of blade-coated PEDOT:PSS films is depicted in Figure 2.4. A typical film is shown in Figure 2.5. After the annealing process, the PEDOT:PSS thin films were kept in a moisture free atmosphere to avoid water absorption.



Figure 2.4 Complete fabrication process of PEDOT:PSS thin films. The filtered PEDOT:PSS solution was blade coated and annealed on a hot plate.

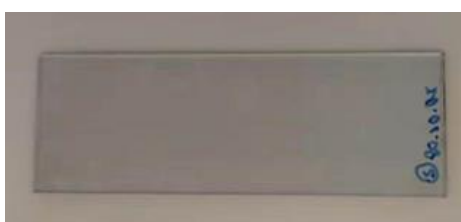


Figure 2.5 Photograph of a blade-coated PEDOT:PSS (Aldrich 483095) thin film on a glass slide.

Regarding the homogeneity of the PEDOT:PSS thin films, the coffee ring effect leads to inhomogeneous films, as typically observed for blade-coated films. The capillary flow induced by the drop evaporation causes the coffee ring effect. At first, the evaporation rate of the edges is faster. To maintain the original size of droplets, the resulting outward flow carries the dispersed material from the interior to the edge. Finally, there is more dispersed material on the edge, hence, resulting in an inhomogeneous film. Nevertheless, the coffee ring effect can be avoided by setting suitable blade parameters. The coating parameters used in this thesis were optimized to avoid the coffee ring effect.

2.3 Thickness gradient in thin films

The thickness of the PEDOT:PSS thin film was continuously varied along the deposition direction, which was set parallel to the long axis of a glass slide. The blade-coating parameters of PEDOT:PSS films with thickness gradients have been presented in section 2.2.

Doctor blade is an ideal means for solution-based deposition of thin films onto large area substrates. In addition, it allows for the fabrication of thin films with a wide range of thickness from 10 nm to ~260 nm depending on PEDOT:PSS solution formulation and coating parameters. During the blade coating process, a constant relative movement is established between the blade and the substrate. In our case, the blade moves and the substrate is stationary as illustrated in Figure 2.6. The liquid flow on the substrate originates from the shear stress caused by the blade motion, which drags the coating solution through the small gap (150 μm , in our case) formed between the substrate and the blade⁶³. The key parameters that can be modified to control the deposition of the thin films are: (i) the distance between the blade and the substrate surface. A big gap increases the maximum thickness, resulting in a big thickness gradient. (ii) the speed of the blade. The faster the blade speed moves, the thicker the film will be. (iii) the volume of the solution. A relatively small volume of the solution that aims to be deposited naturally leads to a thickness gradient along the deposition direction on the glass slide. (iiii) the temperature of the blade-coating hot plate. The diagrammatic drawing of a PEDOT:PSS film with a thickness gradient is shown in Figure 2.7.

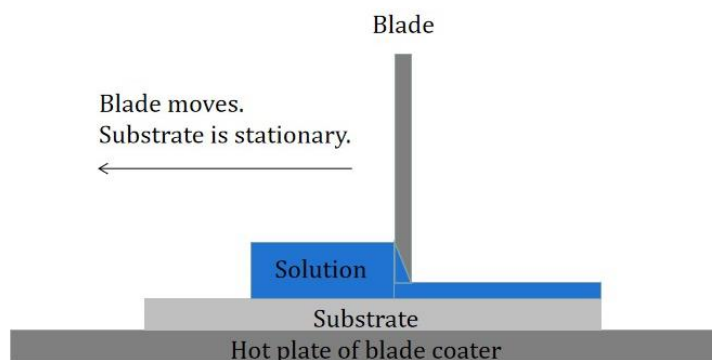


Figure 2.6 Sketch of blade coating process using a blade that is moving relatively to the stationary substrate.

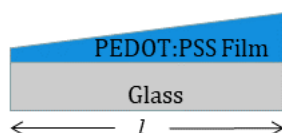


Figure 2.7 Schematic representation of a blade-coated PEDOT:PSS film with a thickness gradient along the length of a glass slide.

The one-dimensional thickness distribution of both studied PEDOT:PSS formulations, i.e. AI 4083 and Aldrich 483095, is illustrated in Figures 2.8.a and 2.8.b, respectively. For AI 4083, the thickness distribution is linear and ranges from 50 nm to 280 nm. On the other hand, the thickness gradient of PEDOT:PSS (Aldrich 483095) film ranges from 80 nm to 220 nm. The lower boundary of the thickness gradient can be as low as 10 nm by adjusting fabrication parameters. However, the upper boundary is typically below 300 nm.

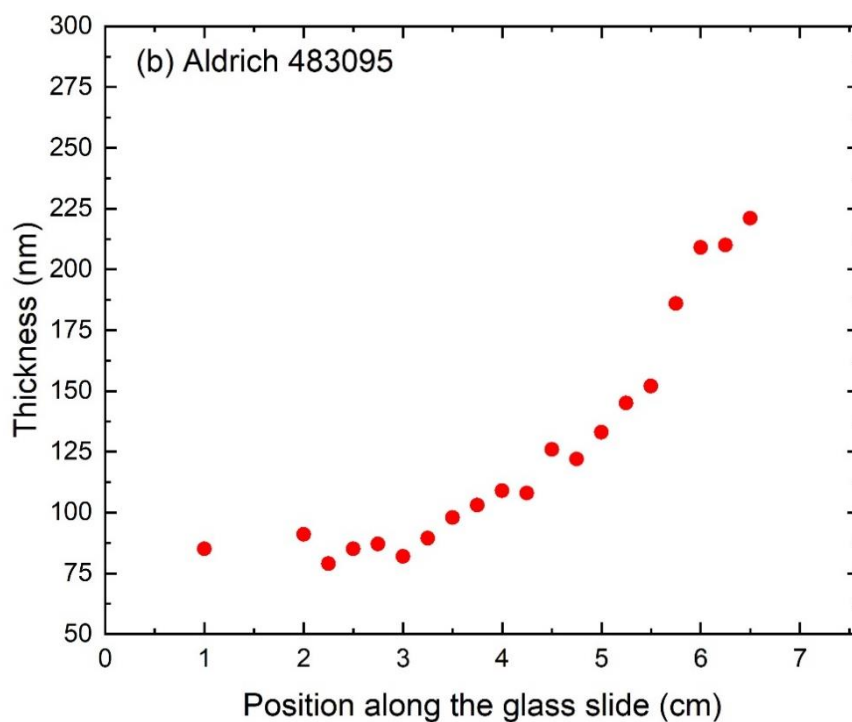
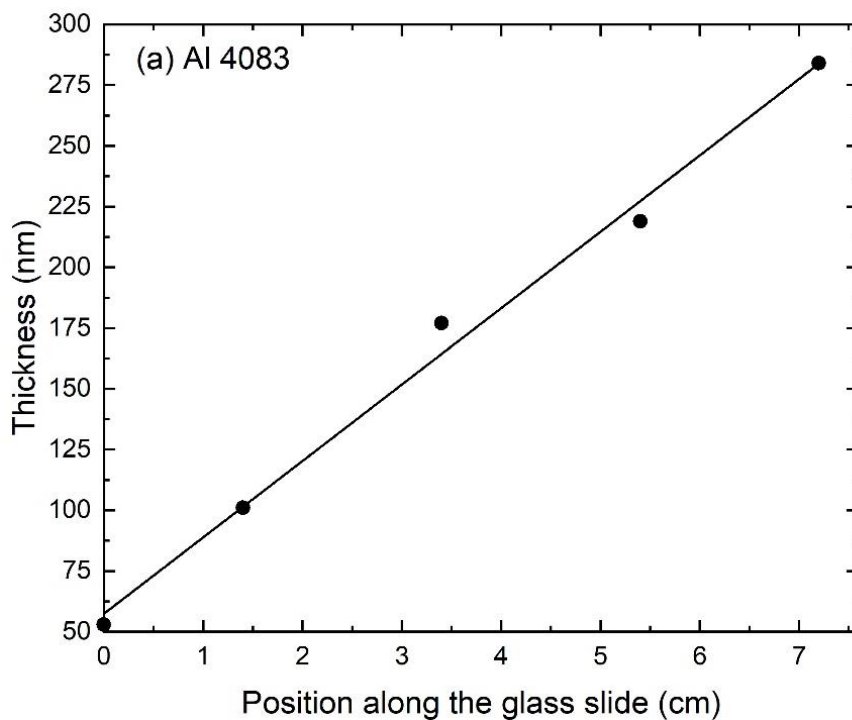


Figure 2.8 Thickness gradients of PEDOT:PSS films parallel to the long axis of glass slides. (a) Al 4083; (b) Aldrich 483095.

2.4 ZnO nanocrystals and nanowires synthesis

A considerable number of methods have been developed to produce ZnO nanowires

(NWs), such as electrodeposition^{64,65}, physical vapor deposition⁶⁶, hydrothermal method^{67,68}, etc. Among all these methods, the hydrothermal method is very attractive due to its low reaction temperature and good potential for upscaling. Moreover, it does not present any strict requirements for the type of substrate, which means that almost any substrate can be used⁶⁸.

Well-aligned ZnO NWs produced by hydrothermal method were grown using a three-step process. In the first step, we used the methodology developed by Pacholski *et al.*⁶⁷ to synthesize ZnO nanocrystals (NCs). 15.6 ml NaOH in methanol (0.03 M) was added dropwise into 30 ml zinc acetate dihydrate in methanol (0.1 M) at 60 °C with continuous stir, and the reaction lasted for two hours. The experimental device for synthesizing the ZnO NCs is shown in Figure 2.9.

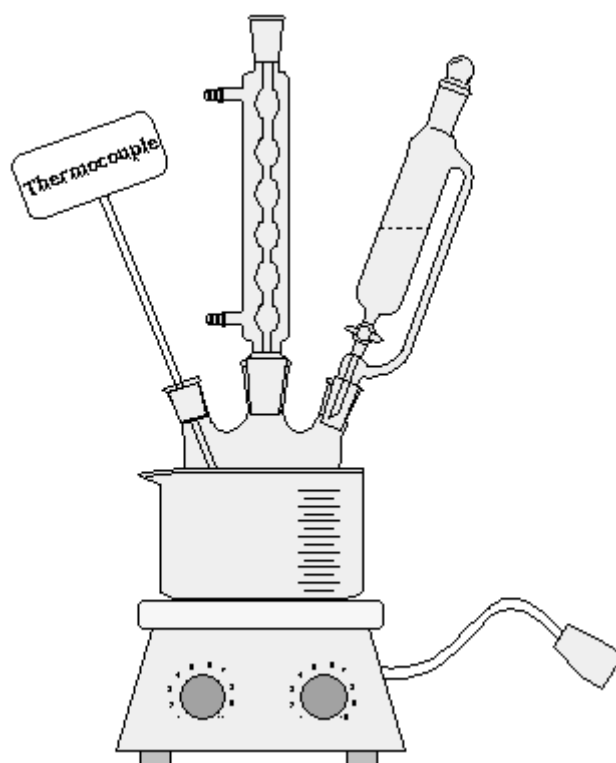


Figure 2.9 Experimental set-up used for synthesizing ZnO nanocrystals. The thermocouple detects real-time temperature and controls the hot plate.

The synthesized ZnO NCs methanol solution was deposited at a spin rate of 6000 rpm on a 1 cm × 1 cm Si wafer. After uniformly coating every layer, the Si wafer was annealed at 150 °C for several minutes to enhance the particle adhesion. In the third step, oriented ZnO NW arrays were prepared from ZnO NCs by hydrothermal process⁶⁸. As illustrated in Figure 2.10, a Si wafer coated with ZnO NCs was placed upside down in a glass beaker.

Aqueous solutions of zinc nitrate hydrate (0.025 M) and methenamine (0.025 M) were added into the vessel at a volume ratio of 1:2. They were stirred at 90 °C for 8 h. In order to improve the distribution uniformity of ZnO NWs, the solutions were replaced every one hour. Finally, the Si wafer was washed with deionized water and dried.

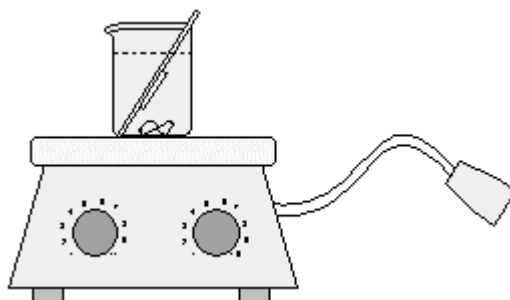


Figure 2.10 Schematic diagram of synthesizing oriented ZnO nanowires by hydrothermal method.

2.5 Fabrication of hybrid films: ZnO NCs/PEDOT:PSS and GQDs/PEDOT:PSS

The vacuum filtration method⁶⁹ was used to fabricate thick ZnO NCs/PEDOT:PSS hybrid films, as shown in Fig. 2.11. Briefly, the synthesized ZnO NCs in methanol were added into the PEDOT:PSS aqueous solution dropwise with continuous stir. The resulting mixtures were stirred for 30 min. Subsequently, 1 ml of a well-dispersed mixture was added in the vacuum filtration apparatus (0.1 μm PTFE filter paper).

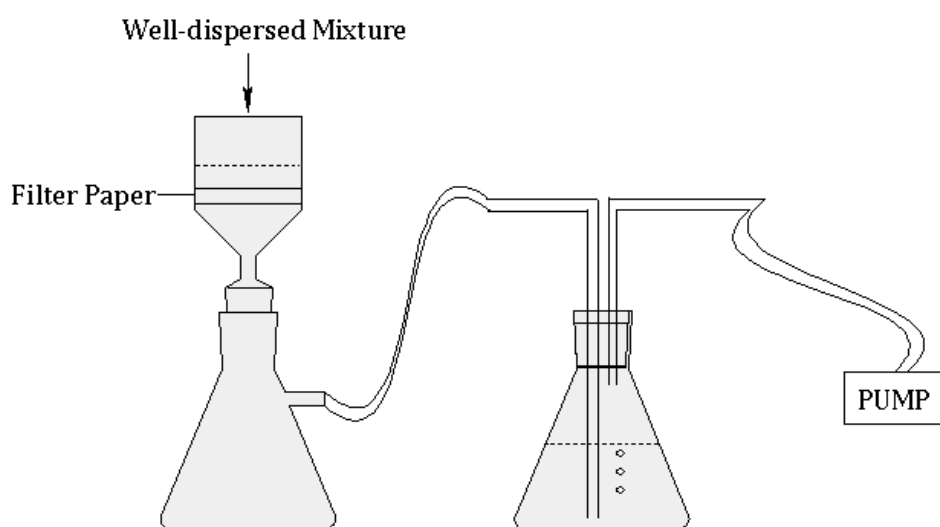


Figure 2.11 Schematic illustration of vacuum filtration apparatus. Evaporated solvents from the suction flask were trapped by isopropanol and ice in the conical flask.

The as-prepared hybrid films were cut into small pieces, and the films were transferred from filter paper to the glass substrate at 60 °C. IPA (or water) moisten the films, which do helps in films transferring. As illustrated in Figure 2.12, the IPA was dropped on the glass or the filter paper. We note that the IPA consumption volume should be moderate, since we have observed that an excessive amount of IPA can cause the fracture and dislocation of the films during transferring process.

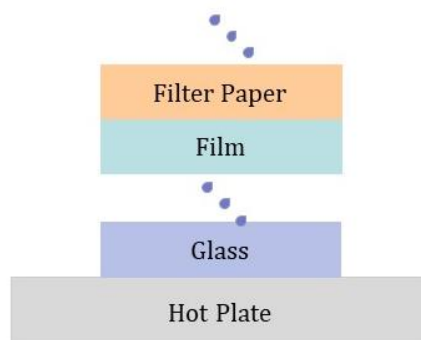


Figure 2.12 Relative position of layers during the film transferring from the filter paper to the glass. Droplets represent isopropanol.

Although we fabricated thick ZnO NCs/PEDOT:PSS films by vacuum filtration, they were not suitable for some of our measurements due to the big surface roughness they exhibited. In order to get smoother films, we fabricated ZnO NCs/PEDOT:PSS hybrid thin films using the blade coater. The cleaning of the glass substrates was the same to that described in section 2.1. Subsequently, the well-mixed ZnO NCs/PEDOT:PSS solution was deposited on a glass substrate by blade coating. The mass ratios of ZnO to PEDOT:PSS we studied are 0, 1/600, 1/400, 1/200 and 1/100. In other words, we have investigated the range with ZnO concentrations below 1% in mass.

The graphene quantum dots (GQDs)/PEDOT:PSS hybrid thin films were also deposited on glass substrates by blade coating. The mass ratios of GQDs to PEDOT:PSS we investigated are 0, 1/10, 1/2 and 1/1.

The coating parameters of ZnO NCs/PEDOT:PSS and GQDs/PEDOT:PSS composites were listed in the following Table 2.2. All composite samples were always kept inside a moisture and oxygen free atmosphere after fabrication.

Table 2.2 Blade-coating parameters of ZnO NCs/PEDOT:PSS and GQDs/PEDOT:PSS hybrid films

Composite	Mass Ratio of Filler to PEDOT:PSS	Temperature (°C)	Blade Speed (mm/s)
ZnO NCs/AI 4083	0	65	90
	1/600	65	90
	1/400	65	90
	1/200	65	90
	1/100	65	90
ZnO NCs/Aldrich 483095	0	110	70
	1/600	110	50
	1/400	110	50
	1/200	110	30
	1/100	110	70
GQDs/AI 4083	0	65	70
	1/10	65	70
	1/2	65	80
	1/1	75	90
GQDs/Aldrich 483095	0	110	40
	1/10	110	50
	1/2	110	60
	1/1	110	60

2.6 Phase-separated films

In the following we describe a DMSO-induced phase separation in PEDOT:PSS films by a slow drying process. The glass substrates (1.25 cm × 1.25 cm) were cleaned with the aforementioned method. The filtered PEDOT:PSS aqueous dispersion was blended with DMSO at a 1:1 volume ratio. The mixture was stirred under room temperature for more than 1 h, and then a 130 μL mixed solution was drop casted onto the glass substrates and slowly dried under room conditions for one week.

After complete drying, the dark PEDOT-rich film was surrounded by a transparent film, as shown in Figure 2.13. According to Liangqi Ouyang's research⁵¹, the transparent area mainly consists of PSS, and the dark film is the concentrated PEDOT:PSS. In good agreement, our studies also confirm that PEDOT only exists in the dark area. We have observed that the dark regions are electrically conducting, whereas the transparent region is electrically insulating. The assignment was also confirmed by Raman spectroscopy, as we will discuss in further detail in Chapter 4.

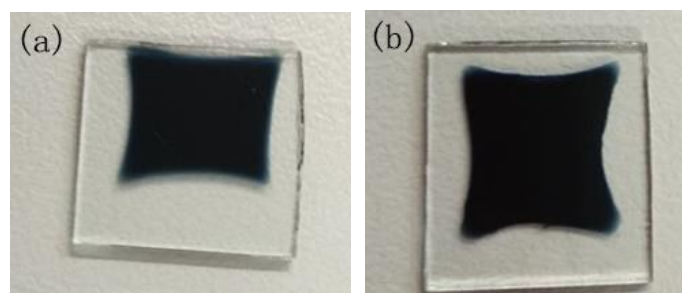


Figure 2.13 Photograph of DMSO-induced phase separated PEDOT:PSS films after complete drying. (a) AI 4083; (b) Aldrich 483095. The dark PEDOT:PSS films were surrounded by transparent PSS films.

The formation of the separated components arises from the faster evaporation rate of water as compared to DMSO under room conditions, which originates from the higher vapor pressure of water (24 mmHg at 25 °C). It was observed that when water evaporated, the dark PEDOT:PSS complexes were no longer soluble and precipitated, whereas a certain amount of colorless free PSS still remained dispersed in liquid phase DMSO during this slow drying process. After drying, these free PSS formed a transparent film around concentrated PEDOT:PSS film.

2.7 Suspended PEDOT thin films

A new PEDOT formulation with a dispersion content of 1.5-2.5% in toluene was used to fabricate suspended PEDOT thin films. The PEDOT solution from Heraeus Clevis™ (HTL Solar 3) use an alternative counter ionomer to PSS to allow for the dispersion in toluene. In order to get suspended PEDOT film, a sacrificial layer was initially deposited by spin coating on the glass substrate. Subsequently, the PEDOT layer was deposited at a spin rate of 3000 rpm for 90 s, as depicted in Figure 2.14. As sacrificial layer we have used poly(sodium-4-styrenesulfonate) (PSSNa), which is ideal due to the good wettability of the PEDOT toluene solution on the surface of the PSSNa film. Most importantly, PSSNa can be easily removed by dissolving it into water, which does not damage the PEDOT layer.

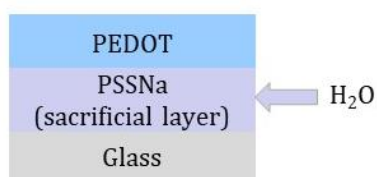


Figure 2.14 Schematic shows 2-layer stack to get a suspended PEDOT thin film.

Finally, the PEDOT film was released by immersing the sample into a water sink. A square scratch was made on the film before immersing, which is beneficial for the film separation from the substrate. The suspended PEDOT film (see Figure 2.15) was captured by a gasket, and it was left under ambient conditions until it was totally dried. The film morphology was studied by optical microscopy. As shown in Figure 2.16, although long range wrinkles are observed on the surface after the evaporation of water, the films resulted homogenous on smaller scales.



Figure 2.15 Suspended PEDOT thin film on a gasket.

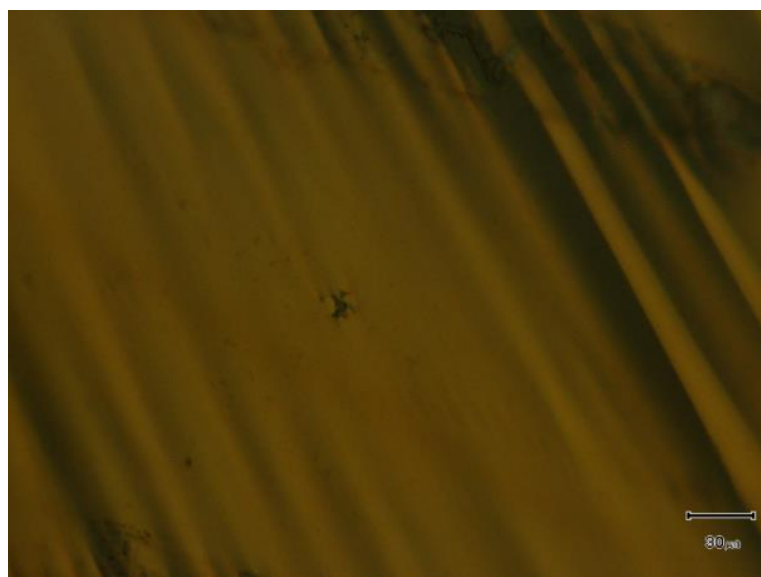


Figure 2.16 Optical micrograph of the surface of the suspended PEDOT thin film. Scale bar represents 30 μm .

III. Experimental Characterization Techniques

Basic working principles of the used equipment as well as representative characterization results used as examples will be introduced in this chapter.

3.1 Surface characterization methods

Atomic force microscopy (AFM) is a surface analysis technique with resolution on the order of fractions of a nanometer. It is widely used for imaging surface topography. It can provide detailed three-dimensional topographies and give information about roughness, grains, phase difference, etc. AFM is essentially applied to investigate the mechanical, electrical, physical and other properties of a sample's surface. Alternatively, it also can be used to determine the thickness of very thin samples.

As illustrated in Figure 3.1, AFM uses a cantilever with an extremely sharp tip (collectively called probe) to scan the sample's surface line by line, while the interaction between the sample's surface and the tip is detected. The motion trajectory of the probe is tracked by a laser beam reflected off the cantilever. This reflected laser beam is monitored by a position sensitive photodiode which records the vertical and lateral motion of the probe, which is calibrated to account for the displacement of the tip caused by the sample's topography.

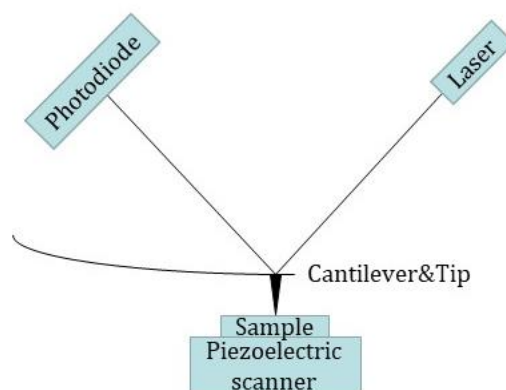


Figure 3.1 Schematic displaying the basic principle of AFM.

According to the degree of contact between the probe and the sample, there are three operating modes in AFM: contact mode, non-contact mode and tapping mode. In contact mode, the tip is in direct contact with the surface of the samples. Contact mode is perhaps the most basic imaging mode, and it is most suitable for imaging relatively hard and smooth surfaces. Non-contact mode is typically chosen for measuring soft materials

without damaging or polluting samples, e.g. biological samples and organic thin films. Tapping mode, also called intermittent contact mode, is the most frequently used mode when operating in ambient conditions.

We used the tapping mode of AFM (Keysight 5100) to measure the surface topography of PEDOT:PSS films as depicted in Figure 3.2. The tip type is App Nano FORT. The stylus force is between 10 nN and 100 nN. The image sizes are typically $5 \times 5 \mu\text{m}^2$ and $2 \times 2 \mu\text{m}^2$.

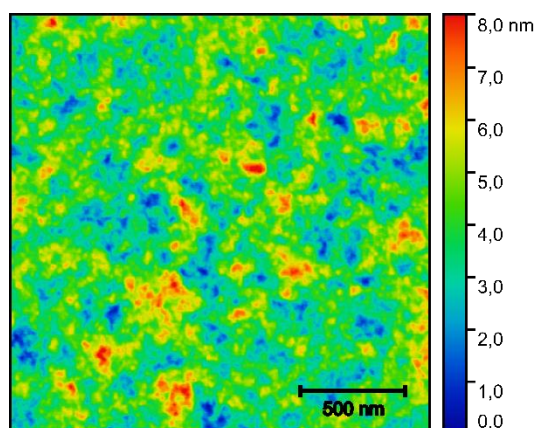


Figure 3.2 Topography image of a blade-coated PEDOT:PSS (AI 4083) thin film with a thickness of 55 nm. The image depicts an area of $2 \times 2 \mu\text{m}^2$. Scale bar represents 500 nm.

Profilometry is a technique used to extract a surface's topographical information. It can be used to detect step height, roughness and morphology. There are two different types of profilometers (called profiler for short), which are: the stylus profiler and optical profiler.

For the stylus profiler, as the diamond stylus moves across the film's surface, the small surface variations in vertical stylus displacement are detected as a function of lateral position, as illustrated in Figure 3.3. Subsequently, the height position signal is converted into a digital signal, stored, analyzed, and displayed. The prominent advantage of the stylus profiler is that it is a direct measurement, i.e. it is independent on the material properties. In contrast, the optical profiler uses light instead of a physical probe, i.e. it is a non-contact surface metrology technique. The light from a lamp is split into two paths by a beam splitter. One path directs the light onto the sample surface, and the other path directs the light to a reference mirror. Reflections from the two paths are recombined and projected onto an array detector. When the path difference between the recombined beams is on the order of a few wavelengths of light or less interference can occur. This interference includes information about the surface contour.

In our particular case, the profiler is mainly used to measure the film thickness. An

artificial scratch was made on the film. The stylus profiler we used is a KLA Tencor D-500 with step heights from nanometers to 1.2 mm. The scan speed is 0.1 mm/s. As PEDOT:PSS films are soft, a small stylus force (0.03 mg) is applied so as to avoid unnecessary damage induced by the stylus.

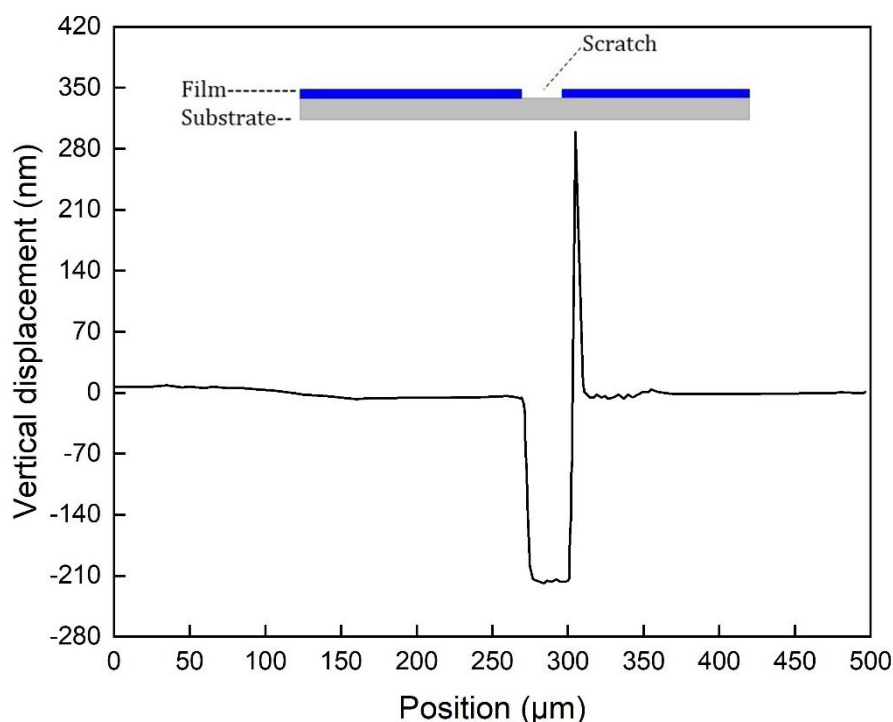


Figure 3.3 Surface profile of a PEDOT:PSS (AI 4083) thin film with the thickness of 215nm.

Scanning electron microscope (SEM) is a non-destructive structural characterization technique. SEM uses a focused beam of high-energy electrons to scan the sample surface. The signal that derives from electron-sample interactions contains information about external morphology (texture), chemical composition, crystalline structure and orientation of solid materials. Among the signal emitted by the incident electrons, the secondary electrons emitted are most valuable for providing morphology and topography, and the backscattered electrons are most valuable for illustrating contrasts in composition in multiphase samples.

For electrically conductive samples, high vacuum mode with higher energy electrons (10-15 kV) is recommended. However, for less conductive samples, it is better to choose low vacuum mode and less energetic electrons (5-10 kV) to allow the residual atmosphere to reduce charging of the sample. In extreme circumstances, depositing a metal layer on the surface will greatly improve the electrical conductivity and thereby

improve the imaging quality.

In this thesis, we used a SEM (FEI Quanta 200 FEG) to detect the morphology of ZnO nanowires under high vacuum mode. The working distance between the final pole piece of the lens and the sample is 10.0 mm. The spot size is 3.5 nm.

3.2 Optical characterization

3.2.1 Spectroscopic ellipsometry

Spectroscopic ellipsometry (SE) measures the polarization change of light upon reflection from or transmission through a sample. The polarization change is represented as the amplitude ratio, ψ , and the phase difference, Δ . The measured response depends on the film thickness, and on the optical properties of the material. Therefore, SE is mainly used to determine film thickness and optical constants. Furthermore, it also provides information about roughness, composition, doping concentration and other material properties associated with a change of the optical response.

SE is a powerful non-destructive test method and has many advantages, such as its high accuracy and good repeatability. It is a self-normalized technique whose result is unaffected if only part of reflected beam is collected, or by fluctuating source intensity or absorption by ambient atmosphere.

3.2.1.1 Components

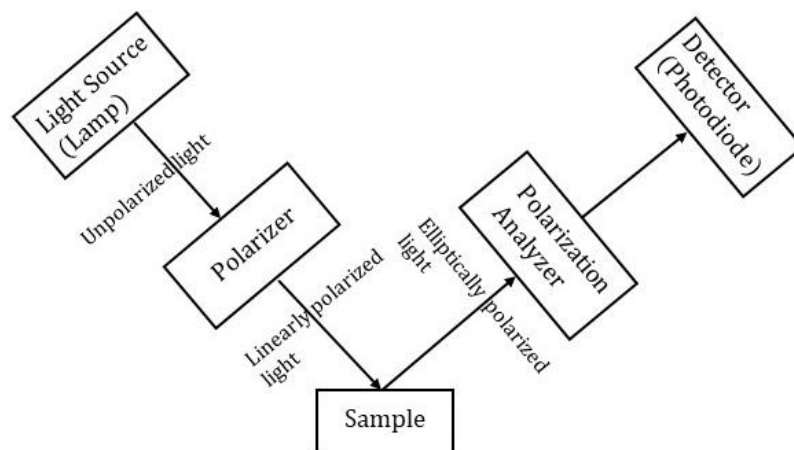


Figure 3.4 A typical ellipsometry experimental setup.

As depicted in Figure 3.4, the basic components of SE consist of light source, polarizer,

polarization analyzer, and detector. Initially, light exits from the lamp and goes into the polarizer which changes the incident unpolarized light into linearly polarized. Linearly polarized light is reflected on the sample's surface and, in the general case, becomes elliptically polarized light. The polarization changes (amplitude and phase) due to the light-sample interaction are detected by the polarization analyzer. Finally, optical information is converted to an electric signal using a photodiode.

3.2.1.2 Fundamental principle

For a non-magnetic sample, SE only considers the electric field vector which can be decomposed into two orthogonal components, p-wave (parallel to the plane of incidence) and s-wave (perpendicular to the plane of incidence) as shown in Fig. 3.5. When two linearly polarized waves with the same frequency are combined out of phase ($\neq 90^\circ$), the resultant wave is elliptically polarized.

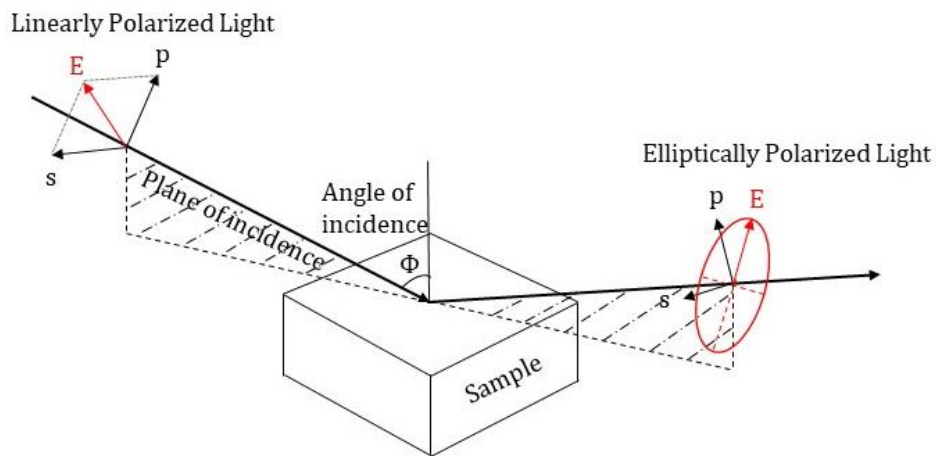


Figure 3.5 Schematic diagram of ellipsometry measurement. The incident linearly polarized light with p- and s- components interacts with the sample, producing outgoing elliptically polarized light.

As we can see from Figure 3.5, the p-waves and the s-waves reflect from the surface. Upon reflection, there is a phase shift between the p-wave and the s-wave, as well as an amplitude change for both waves, which are related to the film thickness and optical functions of the isotropic sample.

The phase shift Δ , is expressed as

$$\Delta = \delta_1 - \delta_2 \tag{3.1}$$

where δ_1 is the phase difference between the p-wave and the s-wave before the

reflection. δ_2 is the phase difference between the p-wave and the s-wave after the reflection. The range of Δ is between -180° to $+180^\circ$ (or from 0° to 360°).

The amplitude ratio $\tan \psi$, is the ratio of the magnitudes of the Fresnel reflection coefficients for the p-wave (R_p) and the s-wave (R_s). The range of ψ is from 0° to 90° . Fresnel reflection coefficients are defined as the ratio of the amplitude of the outgoing light to the amplitude of the incident light for each of the two polarizations.

$$\tan \psi = \frac{|R_p|}{|R_s|} \quad (3.2)$$

Using the definitions in Eq. (3.1) and (3.2), we write the fundamental equation of ellipsometry in an isotropic sample as follows.

$$\rho = \tan \psi e^{i\Delta} = \frac{R_p}{R_s} \quad (3.3)$$

where ρ is defined as the complex ratio of the total reflection coefficients. The term $\tan \psi$ provides the magnitude of ρ , whereas the exponential function $e^{i\Delta}$ provides the phase of ρ .

The complex refractive index $\tilde{\varepsilon}$ and the complex dielectric function \tilde{N} are two common descriptors for the optical properties of a material. They are complex second-rank tensors which for isotropic samples are complex scalars. Both are composed of real and imaginary parts and give information about how material and light interact. They can be transformed mutually in terms of the following equation:

$$\tilde{\varepsilon} = \tilde{N}^2 \quad (3.4)$$

The complex refractive index \tilde{N} , describes the change of a light wave due to its interaction with a material.

$$\tilde{N} = n \pm ik \quad (3.5)$$

where i is the imaginary unit number. The real component n , is the refractive index, which describes how fast light travels through the material relative to vacuum.

The imaginary component, given by k , is the extinction coefficient, which describes the intensity of wave absorbed by the material. The relationship between the extinction coefficient and the absorption coefficient is expressed as:

$$k = \alpha \frac{\lambda}{4\pi} \quad (3.6)$$

where α is absorption coefficient, and λ is wavelength in vacuum. When light passes through an absorbing material, a fraction of light is absorbed and k is larger than zero. For transparent materials, k is typically zero.

The complex dielectric function $\tilde{\varepsilon}$, describes the response of a material to the electric

field vector of a light wave.

$$\tilde{\epsilon} = \epsilon_1 \pm i\epsilon_2 \quad (3.7)$$

where the real component ϵ_1 , is related to polarization. The imaginary component ϵ_2 , exhibits the absorption properties of the material.

The physical connection between the real optical function, ϵ_1 , and the imaginary optical function, ϵ_2 , is known as Kramers-Kronig (KK) relation, and it is given by the following relation:

$$\epsilon_1(E) = 1 + \frac{2}{\pi} P \int_0^{\infty} \frac{E' \epsilon_2(E')}{E'^2 - E^2} dE' \quad (3.8)$$

P denotes the Cauchy principal value. E' is angular frequency variable running through the whole integration range.

A full KK integration requires a complete optical spectrum of $\epsilon_2(E')$ because the range of E' is from 0 to ∞ as Eq. (3.8) suggests. However, typical ellipsometry measurements work from the ultraviolet ($\lambda \sim 200$ nm) to the near infrared ($\lambda \sim 2000$ nm). In other words, ellipsometry measurement could not cover all frequencies of $\epsilon_2(E')$. Therefore, KK consistency only gives the general shape of curve ϵ_1 . In order to get the absolute magnitude of ϵ_1 , the high-frequency dielectric constant ϵ_{∞} is needed. Most oscillator models include ϵ_{∞} which compensates for missing absorption not represented in KK integration.

3.2.1.3 Models

For any transparent material and absorbing material at the wavelengths where they are transparent, the index of refraction increases towards shorter wavelength. This is referred to as normal dispersion. The **Cauchy equation** (see Eq. 3.9) is used to describe the wavelength dependence of the refractive index of transparent materials, or absorbing materials in the transparent spectral region.

$$n(\lambda) = A + \frac{B}{\lambda^2} + \frac{C}{\lambda^4} \quad (3.9)$$

where λ is the wavelength. A, B and C are Cauchy coefficients. A is the principal part of refractive index, and it gives the value of refractive index at longer wavelengths. B and C control the curvature of the refractive index curve. "B" value is generally between 0.002 and 0.02, and "C" value is close to 0.000⁷⁰.

Cauchy equation does not give any restriction to the shape of refractive index curve. However, the variation of refractive index of materials in the transparent spectral region with the wavelength should conform to the normal dispersion. Thus, after calculation

using Cauchy equation, it is necessary to check the curve shape of refractive index to confirm it follows normal dispersion.

The **Drude model** has been widely used to describe the optical properties of metals, inorganic conductors and heavily doped semiconductors. The dielectric function according to the Drude model is expressed as follows^{71,72}.

$$\varepsilon(E) = \varepsilon_{\infty} - \frac{E_p^2}{E^2 + iE\Gamma} \quad (3.10)$$

where E is the photon energy, ε_{∞} is the high frequency dielectric constant, i is the imaginary unit, E_p is the plasma energy, and Γ is the Drude broadening.

The plasma energy increases with carrier concentration, N , as Eq. (3.11) shows⁷³⁻⁷⁵. The Drude broadening, also called broadening coefficient or damping coefficient, can be interpreted as the result of carrier-carrier scattering and/or collisions with molecules, atoms, and/or ions⁷². The Drude broadening is inversely associated with carrier mobility, μ , as shown in Eq. (3.12).

$$E_p = \sqrt{\frac{Ne^2}{\varepsilon_0 m^*}} \quad (3.11)$$

$$\mu = \frac{e}{m^* \Gamma} \quad (3.12)$$

where ε_0 is the dielectric constant of free space, e is the electron charge, and m^* is the effective mass of the charge carriers.

Effective medium approximation (EMA) models were used to describe the rough sample surface during the regression analysis of SE. Within this model, the rough surface was regarded as a layer consisting of a mixture of the materials above and below the interface. It is assumed that both materials mix well, but retain their own optical properties⁷⁰. The EMA theory allows us to calculate the optical properties of a heterogeneous sample from its constituents.

Bruggemann effective medium approximation (BEMA) model is typically used in modeling the surface roughness or the intermixing layer of binary constituents. It is assumed that the size and separation distance of particles are smaller than the optical wavelength so that the medium behaves homogeneously⁷⁶. BEMA equation is expressed as follow:

$$f_A \frac{\tilde{\varepsilon}_A - \tilde{\varepsilon}_{EMA}}{\tilde{\varepsilon}_A + 2\tilde{\varepsilon}_{EMA}} + f_B \frac{\tilde{\varepsilon}_B - \tilde{\varepsilon}_{EMA}}{\tilde{\varepsilon}_B + 2\tilde{\varepsilon}_{EMA}} = 0 \quad (3.13)$$

where $\tilde{\varepsilon}_{EMA}$ is the effective complex dielectric function of the composite material, $\tilde{\varepsilon}_A$ and $\tilde{\varepsilon}_B$ are the complex dielectric functions of component A and B, f_A and f_B are the

volume fractions of A and B. Mathematically, two components A and B play the same role in computing $\tilde{\epsilon}_{EMA}$, which means there is neither host nor inclusion in the BEMA model⁷⁶.

In our case, the BEMA model was used to obtain the GQDs/PEDOT:PSS film thickness and the relative volume fraction of the components. The calculated GQDs fraction based on the BEMA model is in good agreement with the set value in the fabrication process, and the fitted film thicknesses are consistent with the ones from the profiler. These results will be presented in Chapter 5.

3.2.2 Raman spectroscopy

Raman spectroscopy is a potent analysis technique which gives insight into chemical structure, crystal lattice and molecular backbone, phase and polymorphy, etc. In combination with mapping systems, it is possible to get morphology information in inhomogeneous samples.

Raman spectroscopy is based on the interaction of light with the chemical bonds within a material. The incoming light from a laser source is scattered by the molecules. Most of the scattered light is at the same frequency as the laser source and does not provide useful information (Rayleigh scattering). However, a small amount of light (approximately 1 in 10 million photons) is scattered at different frequency, which depends on the chemical structure of the measured material. This is called Raman scattering. Raman scattering occurs in two ways. If the scattered light is of lower frequency than the incoming light, then it is called Stokes scattering. If it is of higher frequency, then it is called anti-Stokes scattering. Noteworthy, it is nearly always the Stokes Raman scattering detected in Raman spectroscopy because the Stokes Raman scattered light is more intense than the anti-Stokes.

The Raman spectrometer we used is WITec alpha300 RA. We show the Raman spectrum of an 89 nm PEDOT:PSS (AI 4083) film in Figure 3.6. All peaks are from PEDOT, and each peak of the Raman spectrum corresponds to a specific molecular bond vibration^{77,78}. The corresponding vibrational modes of the labeled peaks are listed in Table 3.1.

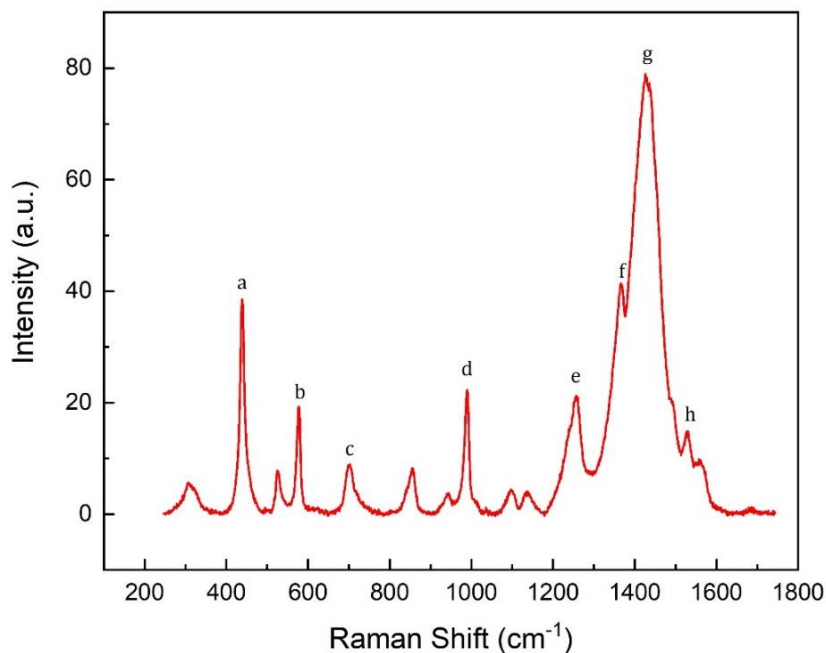


Figure 3.6 Raman spectrum of a blade-coated PEDOT:PSS (AI 4083) thin film with a thickness of 89 nm. The excitation wavelength is 785 nm.

Table 3.1 Summary of vibrational modes in the Raman spectrum of a PEDOT:PSS film (89 nm) at 785 nm excitation wavelength according to Ref.^{77,78}.

Peak	Wavenumber(cm ⁻¹)	Vibrational Modes
a	439	oxyethylene ring deformation
b	577	oxyethylene ring deformation
c	701	symmetric C-S-C deformation
d	989	oxyethylene ring deformation
e	1257	C _α -C _{α'} inter-ring stretching
f	1365	C _β -C _β stretching
g	1430	symmetric C _α =C _β stretching
h	1529	asymmetric C _α =C _β stretching

3.3 Thermal characterization: frequency-domain thermoreflectance technique

Frequency-domain thermoreflectance (FDTR) technique is a non-destructive contactless optical method which can simultaneously determine the thermal conductivity and heat capacity of a sample, as well as the thermal boundary conductance between material layers⁷⁹.

The optical principle of FDTR technique was pictured in Figure 3.7. A pump laser (405 nm) and a probe laser (532 nm) were used to locally heat and probe the local temperature, respectively. A modulated pump laser in the frequency range between 30 kHz and 20 MHz is focused on the sample surface. The surface temperature changes periodically due to the imposed heat flux, leading to the change of the sample's surface reflectivity which is detected by the probe laser. In order to enhance the thermal sensitivity of the technique^{80,81}, a 60 nm Au transducer was evaporated onto the surface of the samples, as displayed in Fig. 3.8. The key quantity that we address is the phase lag between the pump heat wave generated by the pump laser, and the harmonic response of the sample as detected by the probe laser. The frequency dependent phase lag is modelled by solving the parabolic heat equation. As depicted in Figure 3.9, our fits are in good agreement with the experimental data.

In the data processing, the thermal conductivity of glass substrate and gold were independently measured and fitted first. Afterwards, we fitted the thermal conductivity of the PEDOT:PSS film using the thermal conductivity of gold and glass substrate as input parameters. The thicknesses of gold and film layers are from profiler or ellipsometer. The heat capacity and density of PEDOT:PSS films⁸² we used are 1666 J/(kg·K) and 1200 kg/m³, respectively. More parameters are listed in Table 3.2.

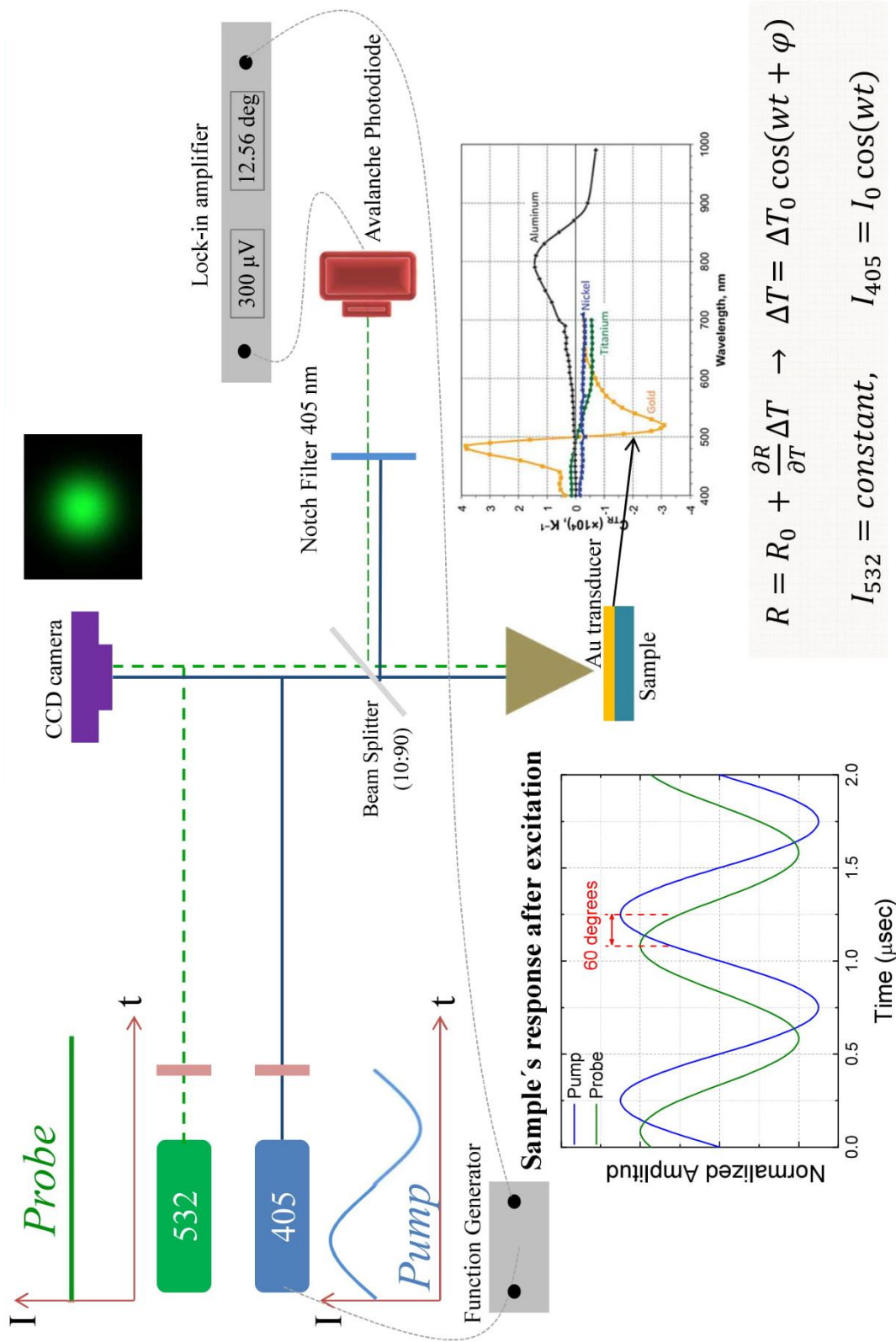


Figure 3.7 Optical principle of frequency-domain thermorefectance. The inset (thermoreflectance coefficient vs. illumination wavelength) is the work of Raad *et al.*¹⁰⁹.



Figure 3.8 A PEDOT:PSS film with a 60 nm gold layer for FDTR measurement.

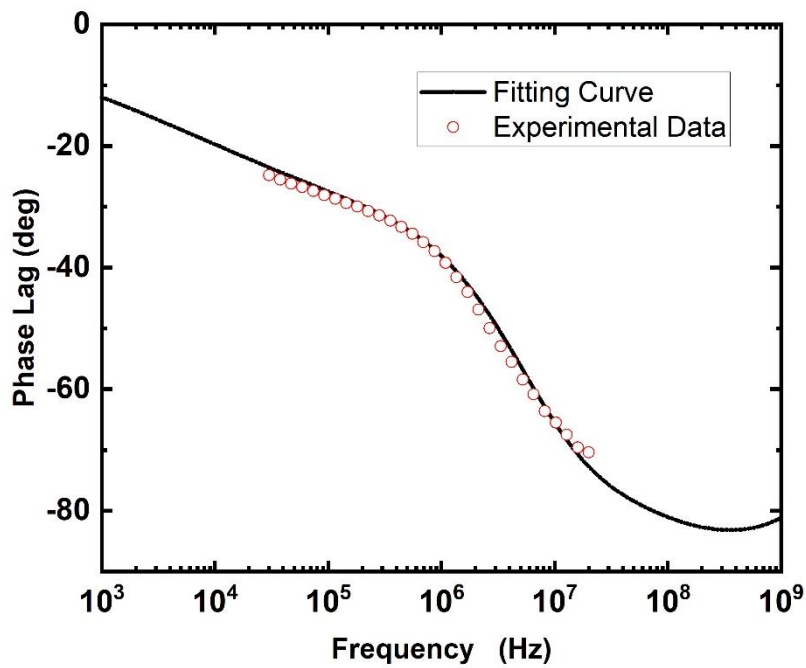


Figure 3.9 Change in the phase lag of a 100 nm blade-coated PEDOT:PSS film with the frequency. The red circles represent the experimental data. The black curve represents the fitting result.

Table 3.2 Parameters in FDTR fitting process

Layers	Heat Capacity (J/(kg·K))	Density (kg/m ³)	Thickness (m)	Thermal Conductivity (W/(m·K))
Gold	129	19300	X ₁	κ ₁
PEDOT:PSS Film	1666	1200	X ₂	κ ₂
Glass substrate	840	2500	1×10 ⁻³	κ ₃

3.4 Electrical determination methods (σ , S)

3.4.1 Van der Pauw method

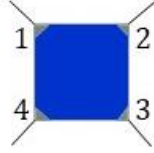


Figure 3.10 Schematic of a square film for the Van der Pauw measurement. Silver paste was deposited on the four corners.

The Van der Pauw method⁸³ is a technique used to measure the sheet resistance and the Hall effect of flat samples of arbitrary shape. In order to use this method, the following conditions must be satisfied.

- (1) Four probes are placed in the perimeter of the sample.
- (2) The four contacts between probes and the sample should be as small as possible.
- (3) The samples show good thickness homogeneity.
- (4) The sample composition is homogeneous, and does not have any holes.

Furthermore, the Van der Pauw method is only suitable for isotropic materials. The sample thickness must be much less than its width and length. The sheet resistance of samples fulfilling the above-mentioned conditions can be calculated in terms of the following formula.

$$e^{-\pi R_{12,34}/R_s} + e^{-\pi R_{23,41}/R_s} = 1 \quad (3.14)$$

where R_s is the sheet resistance. Then the electrical conductivity is: $\sigma = 1/tR_s$. t is the thickness.

$R_{12,34}$ has dimensions of resistance, and is calculated from the measured voltage between the contacts 3 and 4 per unit current that is injected through the contacts 1 and 2. The serial numbers of corners are labeled in Fig. 3.10. $R_{12,34} = U_{34}/I_{12}$

Equation (3.14) is the simplest version of Van der Pauw method. In practice, $R_{12,34}$ is averaged by also measuring with three other (theoretically identical) measurements by reversing the direction of the current and/or switching the current and voltage contacts. The Seebeck coefficient is determined directly from the slope of the ΔV - ΔT plot by slowly heating one side of the sample, while measuring the temperatures of the thermocouples and the Seebeck voltage across the sample.

3.4.2 A custom setup for σ

A custom setup (see Fig. 3.11) consisting of a sourcemeter (Keithley 2604B) and a testing stage with micromanipulators to contact the sample can determine the sheet resistance of thin films.

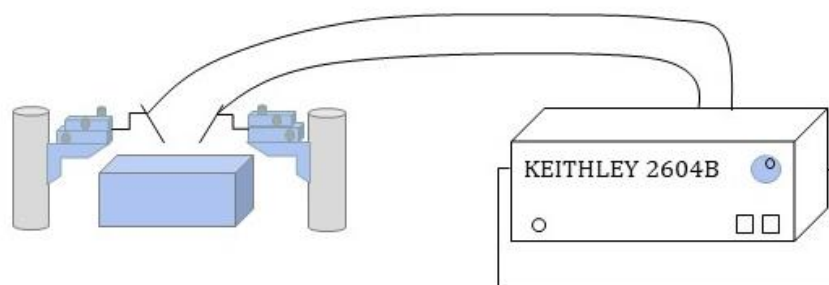


Figure 3.11 A custom setup for the measurement of sheet resistance, in the case of thin films.

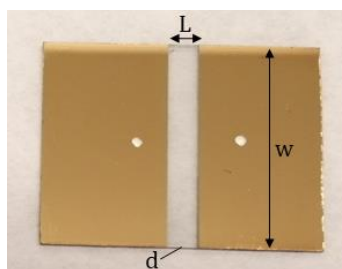


Figure 3.12 PEDOT:PSS thin film for electrical conductivity measurement. The film lies in the transparent area and gold covers the remaining area on the glass substrate. The length, width and thickness of the film are L , w and d , respectively.

As displayed in Figure 3.12, a gold layer with a thickness of 60 nm was evaporated on both sides of the film prior to the measurement, forming a rectangular capacitor-like geometry. Two probes on the testing stage are used to contact the two sides of the film (gold film with or without additional silver paste). The current flows from one probe and arrives at the other one via the film. Before the experiment, a resistance box with variable known resistances is used to calibrate the setup.

The geometry of the film was measured. Then the electrical conductivity is calculated based on the following formula:

$$\sigma = \frac{1}{\rho} = \frac{L}{Rwd} \quad (3.15)$$

where σ is electrical conductivity, ρ is electrical resistivity, R is the measured resistance, L is the length, w is the width and d is the film thickness.

In our case, this custom setup was used to determine the sheet resistances of ZnO NCs/PEDOT:PSS and GQDs/PEDOT:PSS hybrid thin films.

IV. Advanced Optical Characterization of PEDOT:PSS Thin Films

4.1 State of the art

PEDOT:PSS is a widely used organic material in many fields of application⁸⁴, particularly in optoelectronic devices: as flexible electrode for solution-processed solar cells and light-emitting diodes, acting as hole transport and hole injection layer, respectively⁸⁵. Understanding the optical properties of these films to model the optical behavior of such devices is important for their proper design and optimization.

It is widely accepted that PEDOT:PSS thin films are optically anisotropic displaying uniaxial behavior with the optic axis perpendicular to the film plane⁸⁶. Other PEDOT composites have similar optical anisotropy, since it originates in the in-plane arrangement of the PEDOT backbones that results from most solution processes. The anisotropy is also influenced by the composite nature of the films in which PEDOT:PSS grains are surrounded by excess non-conductive PSS. Therefore, the final structure and properties of the films mainly depend on the PSS content of the specific formulation, but also on other film treatments, like DMSO addition, that modify the morphology^{84,85}. This structural variability is reflected in the anisotropic complex refractive indices of the films which are usually determined by spectroscopic ellipsometry. However, most investigations disregard the anisotropy and assume that PEDOT:PSS films are optically isotropic for simplicity^{73,87}. This assumption may be approximately valid sometimes but not always, and in fact it may lead to erroneous conclusions when optical simulation of the devices is needed⁸⁸. In addition, even if not many authors have published reference values of anisotropic complex refractive indices of PEDOT:PSS, considerable scatter of data is found in literature which is also partly due to use of isotropic approximations without clear comparison between isotropic and anisotropic analyses evidencing which kind of errors can be expected when anisotropy is not considered. The two components of the uniaxial complex refractive index of PEDOT:PSS in a wide spectral range were reported in the seminal work of Pettersson *et al.*⁸⁶ for spin-coated films of the Baytron P formulation (1:1.25 ratio by weight). Other reported values are those of Heraeus PH500⁸⁹ and PH1000⁷⁴, both also containing 1:2.5 weight ratio. Finally, spin coated films of Heraeus AI 4083 (1:6) were reported to be optically almost isotropic⁹⁰, although their electrical conductivity was found to be clearly anisotropic⁵⁶. A systematic optical investigation of different formulations including anisotropy and structural considerations is not found at hand.

In this work, we set to rationalize changes in anisotropic complex refractive indices observed in different PEDOT:PSS films. We discuss the anisotropic optical behavior of two quite different commercial PEDOT:PSS formulations, namely Sigma-Aldrich 483095 (1:1.6 ratio by weight) and Heraeus AI 4083 (1:6), comparing with values found in literature. We also compare these results to isotropic approximations and examine the

ellipsometric analysis for very different film thicknesses, from rather thick drop-cast samples to thinner films obtained by blade coating, similar to those used in actual devices. We also study DMSO treated material and correlate the observed variations to structural changes that can be identified from Raman measurements.

4.2 Ellipsometry data fitting

In what follows we describe in detail, as an illustrative example, the analysis of ellipsometry data for the more conductive studied formulation of PEDOT:PSS, namely Aldrich 483095, which displays stronger optical anisotropy. We fit the measured ellipsometric magnitudes $\tan\psi$ and $\cos\Delta$ using both an isotropic model and an uniaxial anisotropic model in which the optic axis of the film is perpendicular to its surface and compare both results. Since all films have low roughness, for the analysis we just consider one film on the isotropic glass substrate which was separately measured and fitted as reference.

The complex dielectric function of PEDOT:PSS can be parameterized using well-known analytic lineshapes⁹¹. The metallic-like behavior given by the bipolaron band⁸⁵ is described using the Drude model whereas other observed contributions such as the polaron band or interband transitions are added as generalized Lorentzians, e.g, zero-dimensional critical points (CPs). Hence, the general lineshape used is:

$$\varepsilon(E) = \varepsilon_{\infty} - \frac{E_p^2}{E^2 + iE\Gamma_p} + \sum_j \frac{A_j e^{i\varphi_j}}{E - E_j + i\Gamma_j} \quad (4.1)$$

where E_p corresponds to the unscreened plasma energy of the free carriers and Γ_p gives their scattering rate. The screened energy of the free-carrier plasma oscillations is $E_p / \sqrt{\varepsilon_{\infty}}$. The parameters of each CP are the amplitude A_j , the phase φ_j , the transition energy E_j and the broadening Γ_j . The Drude model parameters can be related to the electrical resistivity according to:

$$\rho \ (\Omega \cdot cm) = \frac{4\pi\hbar}{\varepsilon_0} \frac{\Gamma_p}{\varepsilon_{\infty} E_p^2} = 0.58695 \frac{\Gamma_p}{\varepsilon_{\infty} E_p^2} \quad (4.2)$$

The unit of ρ in Eq. (4.2) is $\Omega \cdot cm$ when both Γ_p and E_p are inserted in eV. The values of resistivity calculated in this way are helpful to establish relative comparison between films and to provide estimated values which are often smaller than the dc resistivity obtained from electrical measurements. One reason for this discrepancy is the simplistic model but also the higher sensitivity of the electrical measurement to the presence of macroscopic defects in the film⁷¹. The Drude parameters are also useful to estimate the carrier mobility μ and concentration N_p which are given by $\mu(cm^2 / Vs) = 7.2739 / \Gamma_p m^*$ and $N_p(cm^{-3}) = 7.2525 \times 10^{20} E_p^2 \varepsilon_{\infty} m^*$, respectively, where m^*

is the effective mass of the charge carriers and both Γ_p and E_p are expressed in eV. To establish relative comparisons, the effective mass can be taken as 1 although a better estimate could be the value from theory that the effective mass along the chain axis for holes is 0.093⁹².

Figure 4.1.a shows the complex refractive index components $n + ik = \sqrt{\varepsilon}$ obtained for several films. Since all the fit functions are parameterized using Eq. (4.1) we display values extrapolated to lower energy which are relevant for the discussion when the best fit results for both isotropic and anisotropic models are compared. Regarding the anisotropic components, PEDOT:PSS films display positive birefringence, that is, the extraordinary (out of plane) refractive index is larger than the ordinary (in plane) one. The spectral behaviors agree with the in-plane arrangement of PEDOT backbones and obvious conductive behavior of the corresponding component compared to the out-of-plane nonmetallic character. As can be expected from the measurement configuration, the general spectral behavior of the isotropic solution is similar to that of the anisotropic in-plane component⁹³. However, its value is not in between both anisotropic components but it is lower, which seems counterintuitive but it is a consequence of the positive birefringent film optics. It is worth noticing that although the fit in the thick bulk-like drop-cast film data is improved with the anisotropic model (MSE reduced by a factor 1.5), the improvement is most evident in the thinner films when optical interferences appear, from the $\sim 1 \mu\text{m}$ thick film (shown in Fig. 4.1.b) down to device-relevant thicknesses of around 60 nm, which cannot even be properly fitted using Eq. (4.1) and an isotropic optical model (see Fig. 4.2) even if the anisotropy is comparatively smaller than in the drop-cast. In these cases, the MSEs are reduced almost one order of magnitude. The discrepancies using isotropic models are quite clear at angles of incidence around the Brewster angle, which for these films is close to 55 degrees. The Drude parameters determined using the isotropic model are unreliable, ε_∞ and Γ_p are underestimated, while E_p is overestimated. More important, the fitted film thicknesses become quite inaccurate for the isotropic approximations in the thinner films according to profilometer measurements.

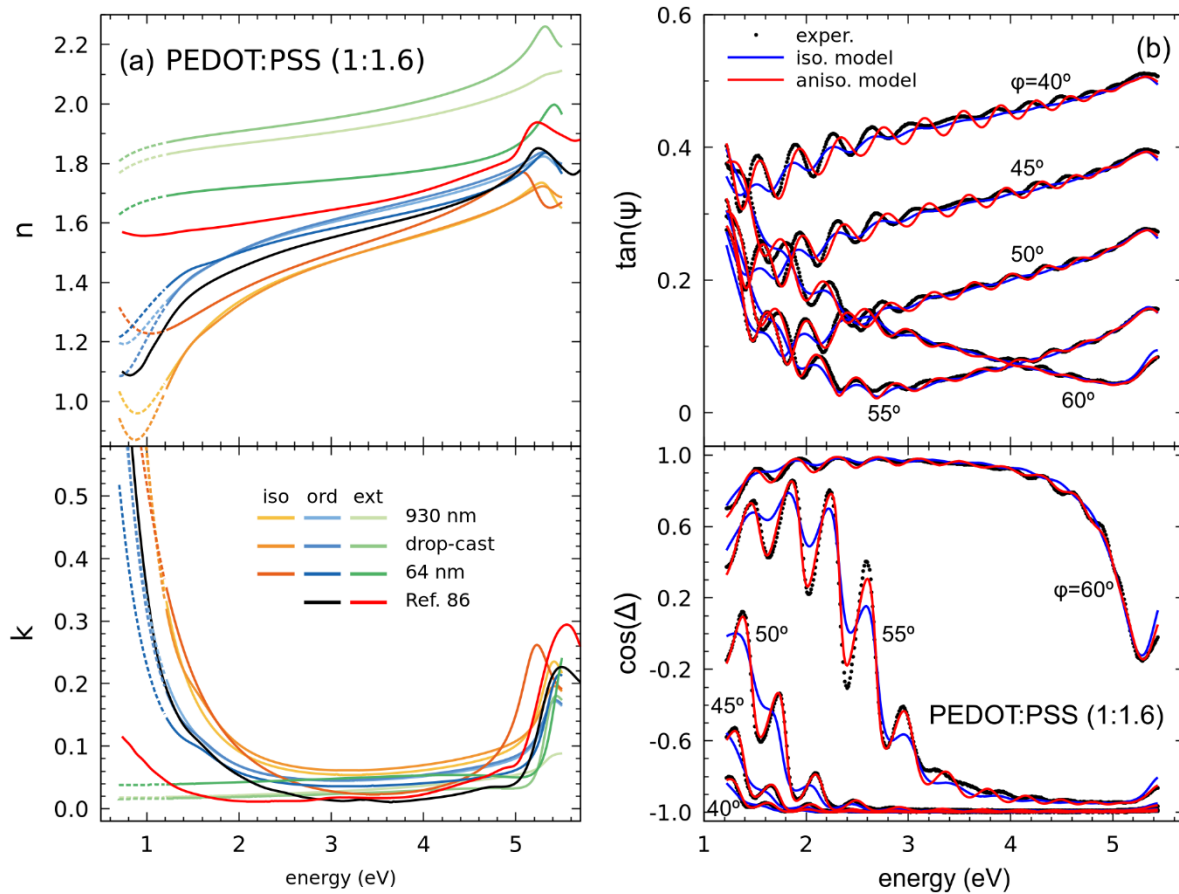


Figure 4.1 (a) Complex refractive index components for different films of PEDOT:PSS (Aldrich 483095). (b) Experimental spectra at five angles of incidence and their best fits using both isotropic and anisotropic models for the thinner ($d=930$ nm) drop-cast film.

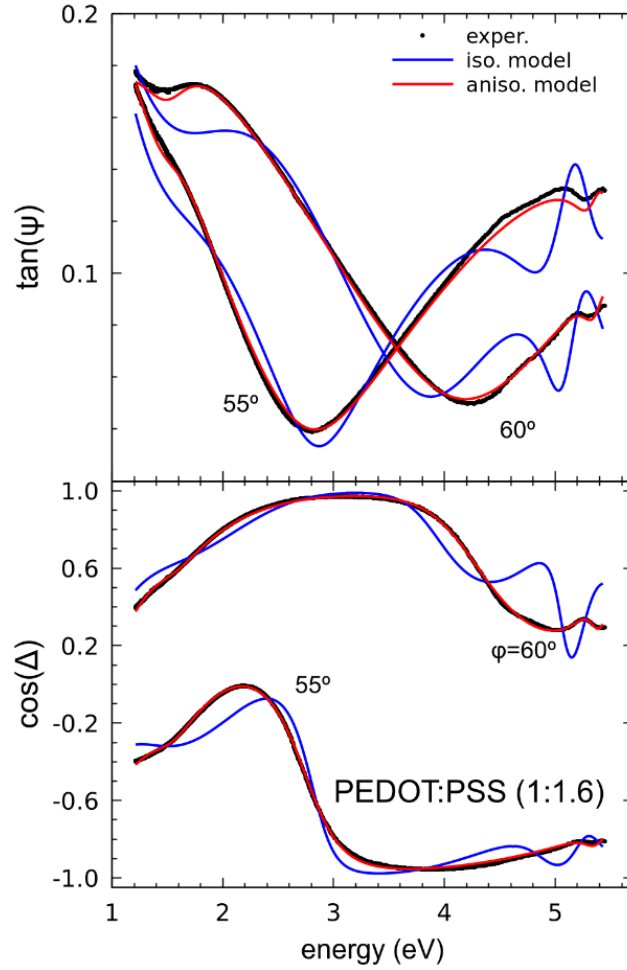


Figure 4.2 Ellipsometric spectra at two angles of incidence for the thin blade-coated film of PEDOT:PSS (Aldrich 483095) and regression fits. Experimental points (black dots) are well fitted by the uniaxial anisotropic model (red lines) but cannot be reproduced by assuming the same analytic expression and an optically isotropic model (blue lines). The film thickness determined by profilometry is 60 nm, the anisotropic fit result is 64 nm and the isotropic fit result is 79 nm.

In order to reproduce the measured spectral dispersions using Eq. (4.1) we need to include up to three CP terms: a rather weak structure often detected close to 1.5 eV which corresponds to the polaron absorption, a prominent peak observed around 5.3 eV which has been attributed to the PSS component, and a higher energy broad peak that represents the contribution of higher lying absorptions in a phenomenological way. This third component is actually added for convenience as it helps to match correctly the experimental background of the spectra. However, this term alters the value of ϵ_{∞} . Therefore, to obtain reliable Drude parameters from the fits using Eq. (4.1), it is convenient to consider just the two first terms and restrict the spectral range for fitting to the lower energy portion of the spectra, as recommended by Humlicek *et al.* in Ref.⁷¹.

A convenient cutoff energy in our case is 3 eV. Since for PEDOT:PSS a weak polaron contribution may be present in the fitted range, in this work we keep three terms including one possible CP to represent the polaron to obtain accurate parameters for use in Eq. (4.2). The relevant Drude parameters obtained for films plotted in Fig. 4.1 are listed in Table 4.1 together with other pertinent results.

In summary, the analysis of ellipsometric data provides both values of film thickness and optical functions whose spectral characteristics can be quantitatively related to the metallic behavior of the PEDOT:PSS films, in particular revealing information about effective doping and electrical parameters. All these magnitudes are seen to depend not only on the specific formulation (or PEDOT to PSS ratio) but also on structural variations that occur during deposition or post treatment.

Table 4.1 Parameters determined from ellipsometry and Raman spectra for selected samples studied in this work. The deposition methods are abbreviated as BC (blade coating) and DC (drop casting). The birefringence $\Delta n = n_e - n_o$ is given at an energy of 2.5 eV as indication of the optical anisotropy of each film. The Drude parameters correspond to the ordinary component.

PEDOT:PSS Aldrich 483095 (1:1.6 ratio by weight)						
Deposition	Δn (2.5 eV)	ϵ_∞	E_p (eV)	Γ_p (eV)	ω (cm ⁻¹)	HWHM (cm ⁻¹)
BC	0.20	1.68	1.28	0.51	1422	41
DC	0.36	1.78	1.48	0.70	1422	41
DC & DMSO	0.15	1.59	1.67	0.82	1427	41
PEDOT:PSS AI 4083 (1:6 ratio by weight)						
BC	0.01	1.52	1.27	0.67	1437	44
BC	0.12	1.58	1.03	0.72	1432	42
DC	0.12	1.56	1.01	0.74	1431	43
DC & DMSO	0.04	1.68	1.10	0.74	1429	39

4.3 Interpretation of Raman spectra

Raman spectroscopy is a well-established optical method to obtain structural fingerprints based on measured vibrational signatures of the samples. In particular, it has been extensively applied to PEDOT:PSS based on experimental knowledge and the vibrational modes calculations performed by Garreau *et al.*⁷⁷ which help to assign the

origin of each mode in PEDOT and deliver valuable insights into the structural transformations of PEDOT upon doping. Despite all this knowledge, controversial statements are found in this abundant literature when partial evidences coming just from Raman spectra are considered. In this context, it is useful to discuss both vibrational and optical spectra together.

It is well known that the Raman spectra of PEDOT:PSS show some dependence with the laser excitation wavelength with usual lasers in the near-infrared and visible range. In particular, the positions of the Raman bands which are associated to the π -bonding system exhibit small shifts with different wavelength excitation due to preferential resonant enhancement of specific segments of the polymer. Longer wavelengths selectively enhance always the segments with longer effective conjugation lengths^{77,94}. However, the main interpretation of the spectra is common to all of them and comparison between samples is possible if spectra are measured with the same excitation. In this work, we choose to work with $\lambda = 785$ nm (1.58 eV) because it has a large resonant effect on the segments of the conjugated thiophene backbone that contribute to the electrical conductivity. This is convenient for correlation with the ellipsometric spectra as well as to obtain reasonably intense signals from very thin films, since we must use low laser powers to prevent heating and degradation of the polymer. In addition, degradation is further reduced by using a less energetic laser in the near infrared.

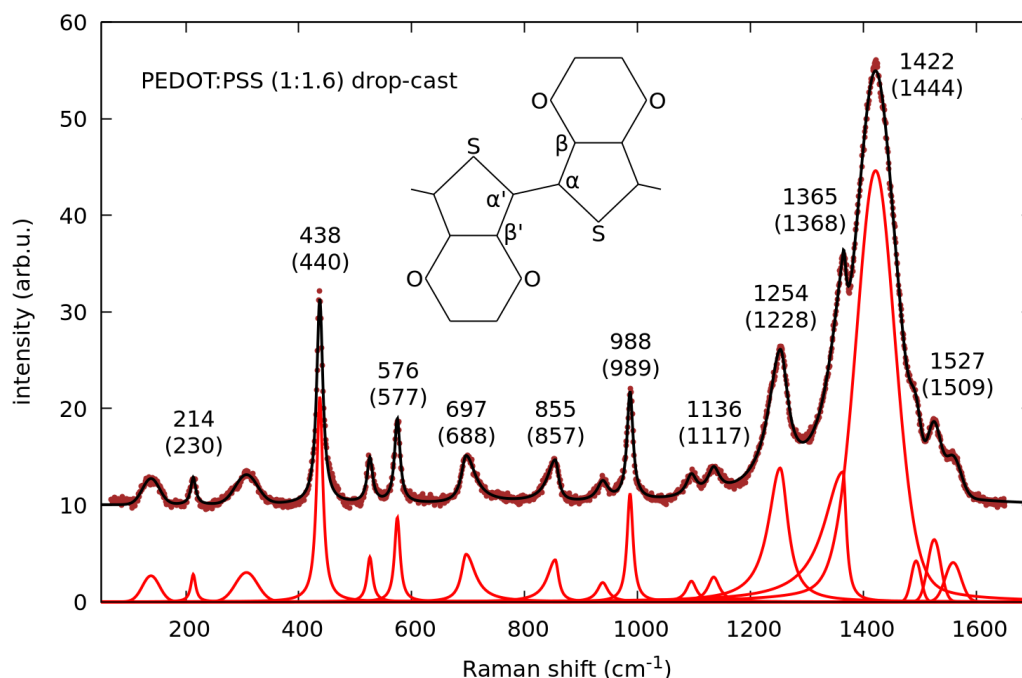


Figure 4.3 Raman spectrum of a drop-cast PEDOT:PSS (Aldrich 483095) film. The fitted components are shown and the obtained Raman shifts are compared to calculated frequencies for PEDOT, given in parentheses according to Ref.⁷⁷.

A typical Raman spectrum is shown in Fig. 4.3. In the fit, each Raman band is initially represented by a pseudo-Voigt function because some bands are better represented by Gaussian and others by Lorentzian lineshapes; once established, these plain lineshapes are chosen. In general, we find that sharper modes are Lorentzian and broader ones are Gaussian. Some bands are obviously asymmetric and are fitted by split profiles. The most intense band near 1422 cm^{-1} is always well reproduced by a symmetric profile with mixed pseudo-Voigt lineshape. The modes that are sensitive to changes in conjugation length are those above 1200 cm^{-1} , as is clear from Fig. 4.4. Among them, the most intense band shows the largest variation upon doping, spanning about 25 cm^{-1} total shift in the PEDOT:PSS complex⁷⁸. This large variation may be an apparent effect since the band possibly contains two components⁷⁸. However, these components do not always appear resolved and experimentally it is practical to just fit one average peak. The origin of these two assumed components is the benzoid-quinoid tautomerism of PEDOT chains, in which the higher frequency component would arise from the benzoid structure and the lower frequency one from the quinoid, agreeing with a longer conjugation length in the latter. This is an idealization because a continuous distribution of molecular conformations is the most probable scenario. Experimentally, the shift upon doping is to the blue, leading to a contradiction with the ground state of PEDOT being aromatic⁹⁵. In addition, calculations support the change to quinoid conformation by doping⁹⁶. Therefore, other mechanisms must counterbalance and be more effective in shortening the conjugation length by increasing doping and the observed Raman shifts cannot be simply interpreted in terms of quinoid to benzoid transformation as frequently done. One possibility could be some twisting of the thiophene backbone⁹⁷, even if PEDOT is considered to be essentially planar. In addition, both intra-chain linearity and inter-chain packing enhance conjugation.

Enhanced linearity is associated to the quinoid conformation. On the other side, enhanced planarity results from PEDOT agglomeration and alignment into large domains. This second mechanism, which is more related to film morphology, could be the dominant one in a real film with phase separation. Another relevant parameter is the linewidth of the main Raman band, which arises from the distribution of conjugation lengths. A narrower band implies more homogeneous distribution of conjugated domains which usually seems to appear for films with red shifted Raman, although in principle, the average position and the linewidth must not necessarily be correlated.

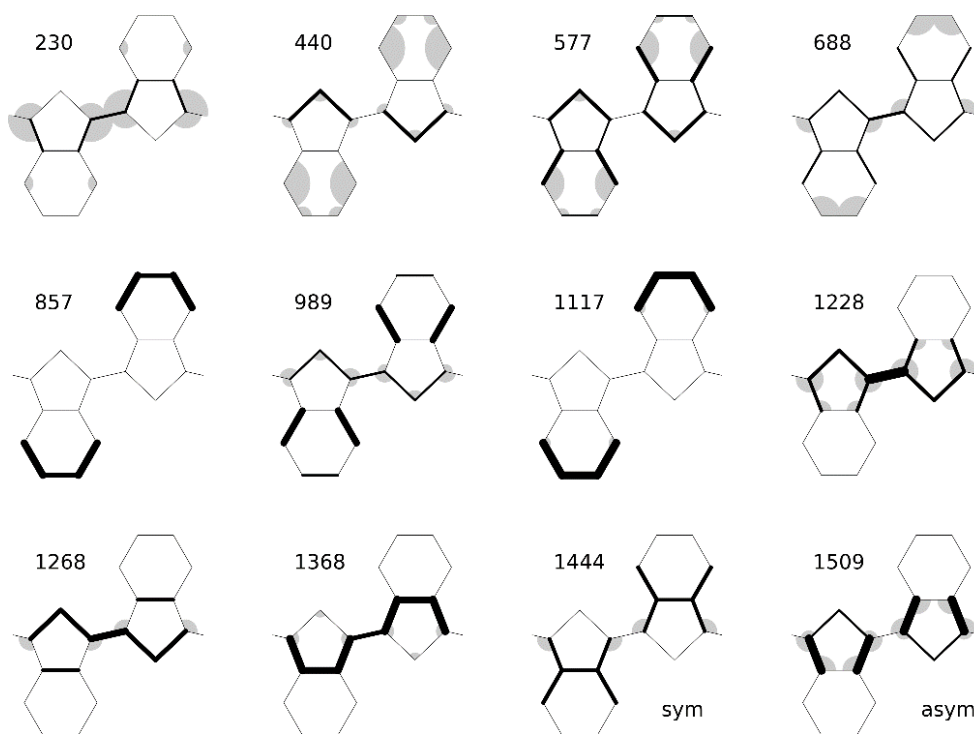


Figure 4.4 Graphical representation of the main modes of PEDOT according to Ref.⁷⁷. Main bond contributions are represented by thicker lines and angles are also proportionally drawn to their variations.

4.4 Spectroscopic results and discussion

As is the case with the electrical conductivity, the measured optical functions represent the response from the combined PEDOT:PSS medium. In particular, observed anisotropies are the result of morphological characteristics of the conducting PEDOT-rich particles embedded in the rather isolating and isotropic PSS-rich host. Hence, PSS richer films are less anisotropic and display lower electrical and optical conductivity. In contrast, Raman scattering is mainly sensitive to PEDOT vibrations; in our experimental conditions we do not detect any PSS vibrations. However, the results of both optical techniques depend on the general film morphological traits. A systematic investigation of both Raman and optical functions including anisotropy is thus helpful to establish the link between optical and structural properties using non-invasive measurements. In the following, we consider the results from different formulations and morphologies to investigate this link.

4.4.1 Dependence with PSS content

The two investigated formulations differ mainly in the ratio of PEDOT to PSS. Despite the

notable difference of proportions 1:1.6 vs. 1:6, in both cases PSS is present in excess in the PEDOT:PSS polyelectrolyte complex and the oxidation level (doping) of PEDOT can be similarly high. The maximum attainable is around 33% ionized sites equivalent to one positive charge every three monomer units. As already mentioned, the films consist of PEDOT:PSS grains embedded in an amorphous PSS matrix. The optical properties of the films correspond to this composed medium, in particular the Drude model parameters of Eq. (4.1) reflect the composite behavior, whereas the critical points are characteristic optical transitions more localized in the components. Note that the weak polaronic transition is localized in PEDOT and its absence or weakness qualitatively indicates the high doping level in all studied films. The largest difference in the two studied formulations being the PSS content, is mostly reflected in the Drude parameters. In particular, the plasma energy gives an indication of the overall PSS content. Regarding the optical anisotropy, we already mentioned that it is larger for the lower PSS content Aldrich 483095 films but we find that films of AI 4083 are still anisotropic, especially if dropcast⁹³. In both formulations, the anisotropy in blade-coated films is comparatively smaller due to faster drying which leads to a morphology with smaller phase separation⁵¹ implying smaller aggregation of PEDOT:PSS grains. Figure 4.5 shows the complex refractive index components for films of AI 4083 showing different anisotropy. The Raman spectra of the same films show up to 5 cm⁻¹ difference in position of the main peak, which is a quite large dispersion compared to 9 cm⁻¹ difference in position between the drop-cast films of the two formulations. It seems clear that the usual identification of main Raman peak position, or in other words conjugation length, solely determined by doping of the PEDOT chain is not valid. Interestingly, the Raman results for films of the same formulation displayed in Fig. 4.5 suggest that the different anisotropy is related to different Raman shift (see Table 4.1). Unfortunately, anisotropy is also related to the PSS content because the PSS matrix is rather isotropic. However, in comparable films, increasing anisotropy gives decreasing Raman shift, pointing to an important influence of inter-chain packing in aggregated grains within the film as mechanism to enhance conjugation length. The linewidth is not clearly reduced, suggesting that the dispersion in conjugated lengths changes very little even if the average is enhanced.

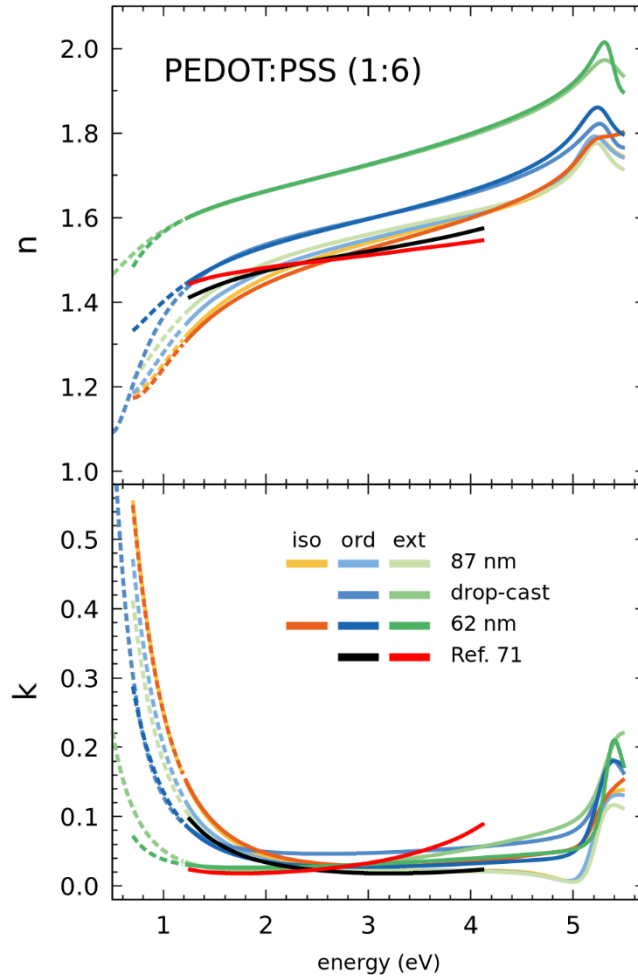


Figure 4.5 Complex refractive index components for different films of PEDOT:PSS (AI 4083). Results obtained both using isotropic and anisotropic models for the thinner films are shown.

4.4.2 Effect of DMSO addition

The role of morphology regarding the optical properties can be further clarified by considering the optical properties of films modified by DMSO addition. The effects of DMSO are most clearly appreciated in drop-cast films in which drying time is longer and changes can develop to a greater extent. Also, the changes induced by DMSO are also more clear in lower PSS content films, in our case of the Aldrich 483095 formulation. In all cases the measurements were done far from the film border where PSS segregation is noticeable. Relevant resulting parameters for all samples selected in this study are listed in Table 4.1.

In all cases, DMSO addition tends to reduce the optical anisotropy. This reduction may be due to smaller PEDOT:PSS grains in the PSS matrix or a lower overall correlation of

in-plane order among the grains. At the same time, the optical spectra (see Fig. 4.6) display more clear polaron bands, consistent with literature⁹⁸, indicating dedoping of the PEDOT:PSS regions. Both facts support the explanation that the higher electrical conductivity is mainly related to a change in phase separation structure that leads to improved connectivity of the PEDOT:PSS regions in the film⁹⁹.

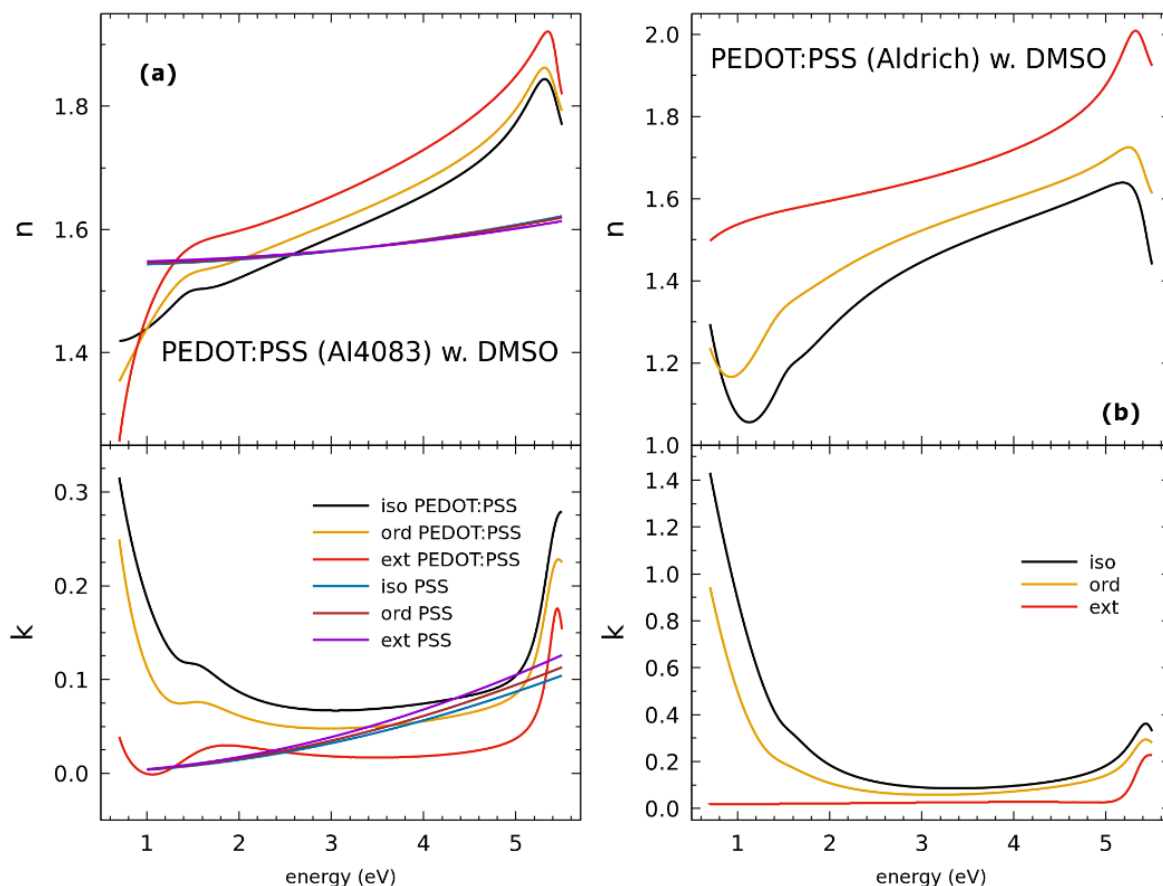


Figure 4.6 Optical functions of PEDOT:PSS modified with DMSO. The isotropic model results are given by the black curves, whereas the anisotropic model results are the orange (ordinary) and red (extraordinary) curves. The results obtained for the segregated PSS film are also plotted in (a), the result is virtually isotropic and we do not observe clear interband transitions in the measured spectral range. Comparing the n and k of the PEDOT:PSS to the pristine drop-cast samples, the main changes are a lower birefringence, a higher plasma energy (due to the smaller excess PSS content), and the appearance of a weak polaron signature near 1.5 eV that indicates some dedoping.

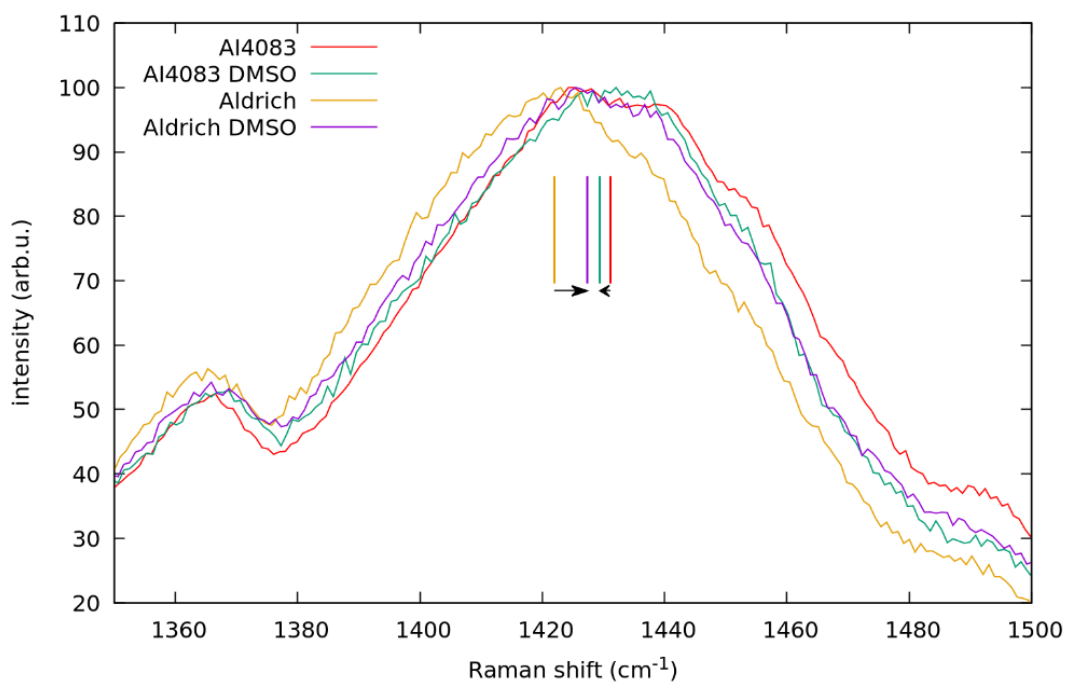


Figure 4.7 Main Raman band for the drop-cast PEDOT:PSS films before and after DMSO treatment.

Figure 4.7 shows the main Raman band for the four drop-cast films. The shifts in this band give indication of the local changes in the PEDOT:PSS grains. Although there is dedoping in both cases, the change in position for every formulation is different. Clearly, the Raman shift is not correlated with the overall PSS content in the film and in particular the large blue shift for the lower PSS containing film suggests that morphology change plays the main role in the shift which indicates a decrease in correlation length. In general, the position of the Raman band seems to result from at least two contributions with opposite sign: a red shift due to dedoping and a blue shift that is likely due to reduction of the grain size. The first predominates in higher PSS content film where the grains are already small without DMSO, and the second in the lower PSS content film that has larger aggregates without DMSO which allow an increased dispersion of the aggregated domains upon DMSO addition, in consonance with recent studies⁹⁹.

4.5 Conclusions

Both spectroscopic ellipsometry and Raman scattering are noninvasive and versatile methods able to probe different structural traits related to the optoelectronic properties of PEDOT:PSS films. The combined study using these optical spectroscopies provides

detailed insights into diverse significant aspects of this complex material. The main optical information extracted from ellipsometry are the optical constants of the composite medium including anisotropic behavior, as well as their spectral characteristics related to average doping and optical conductivity. In addition, interband transitions are signatures of more local properties, in particular the appearance of a weak polaron band is related to the doping state of the PEDOT:PSS domains. On the other hand, the main information obtained from the position of the main Raman band is associated to the correlation length for PEDOT in the same domains. Previous literature suggested that correlation length depends only from the chain conformation given by the doping state, roughly related to the PSS content. In this work, we find that the film's phase separation nanomorphology gives a likewise important contribution to the Raman shift. Since the morphology is connected to the optical anisotropy, there is a correlation between anisotropy and Raman shift in films with the same PSS content, so that higher anisotropy is found together with longer correlation length.

Films obtained with DMSO addition tend to be less anisotropic. This may seem surprising but is consistent with the morphology change induced by this additive. The segregation of PSS caused by DMSO gives as a result some dedoping and improved alignment of the fibrils in the PEDOT:PSS domains but it also tends to cause misaligned and smaller aggregated grains that as a result are closer. Hence, even if the correlation length in a grain may be reduced, their closer proximity can lead to improved optical and electrical conductivity. This effect is largest in the low PSS content formulation we have studied, and is relatively small in high PSS content, since the phase separation of the pristine films is already quite small.

Finally, we must emphasize that it is very difficult to generalize trends which depend from a complex interplay of different parameters. In fact, not only PSS contents and the different solvent/additives can give rise to films with different properties. Different deposition methods and different conditions can also result in different morphologies. Therefore, the availability of advanced optical characterization procedures as outlined in this study are expected to be very useful in understanding and optimizing PEDOT:PSS films for optical and thermoelectric applications.

V. Thermal and Optical Properties of PEDOT:PSS Based Films

5.1 State of the art

Poly(3,4-ethylenedioxythiophene) (PEDOT)-based polymers are currently among the best candidates for thermoelectric harvesting of waste heat targeting near-room temperature applications, i.e., below 150 °C. PEDOT:PSS is an extensively studied organic thermoelectric material. High performance thermoelectric materials require high electrical conductivity and Seebeck coefficient, as well as low thermal conductivity.

When investigating the thermoelectric properties of PEDOT:PSS films, most effort is focused on the electrical conductivity and Seebeck coefficient, and considerably less on the thermal conductivity. Jun Liu *et al.*⁸² studied the thermal conductivity variation of drop-cast PEDOT:PSS films with the DMSO concentration. They found that out-of-plane thermal conductivity (κ_{\perp}) stays constant with the increase of DMSO concentration, 0.3 W/(m·K), whereas in-plane thermal conductivity increases from 0.6 W/(m·K) to 1 W/(m·K). G-H. Kim *et al.*³⁷ report that κ_{\perp} decreases from 0.30 W/(m·K) to 0.22 W/(m·K) in DMSO-mixed PEDOT:PSS films and from 0.32 W/(m·K) to 0.23 W/(m·K) in EG-mixed PEDOT:PSS films with increasing solvent treatment time. Nelson *et al.*¹⁰⁰ found that κ_{\perp} of PEDOT:PSS/Te nanowires hybrid films decreases from 0.36 W/(m·K) to 0.06 W/(m·K) with the increase of Te nanowire weight fraction up to 1%.

In this thesis, we emphasize research on the thermal conductivity of PEDOT:PSS films. In order to tune their thermal conductivity, two strategies were adopted: (i) to fabricate thickness dependent PEDOT:PSS thin films, and (ii) to blend it with inorganic nanoparticles, in particular ZnO nanocrystals (ZnO NCs) and graphene quantum dots (GQDs).

The semiconductor zinc oxide has gained much research interest because it has a wide band gap (3.37 eV) and a large exciton binding energy (60 meV), which contributes to its numerous applications, such as piezoelectric devices, sensors, ultraviolet lasers, photo-electric devices, etc. In addition, ZnO nanoparticles are notable because of their various remarkable chemical and physical properties depending on the different ways they are synthesized. Lin *et al.*¹⁰¹ observed that the electrical conductivity of ZnO nanoparticles (35 nm)/PEDOT:PSS hybrid thin films rises with the ZnO fraction at 300 K. The improved conductivity is mainly due to the enhanced carrier mobility.

GQDs, with a size of several nanometers, attract a lot of attention in recent years due to their unique properties. They have high electron mobility, low toxicity, good solubility in many solvents, and excellent optical and electronic properties, which makes them interesting candidates for a wide range of applications. It has been demonstrated that GQDs can be used in diverse areas related to energy harvesting and efficiency such as in photovoltaic devices, organic light-emitting diodes, etc¹⁰². Kim *et al.*¹⁰³ and Du *et al.*⁴⁴

both observed that the electrical conductivity and Seebeck coefficient of PEDOT:PSS films increase significantly after incorporating GQDs. Wang *et al.*⁴⁵ found that the thermal conductivity of GQDs/PEDOT:PSS (PH1000) films slightly increases from 0.8 W/(m·K) to 0.95 W/(m·K) when the mass ratio of GQDs to PEDOT:PSS increases from 0.1% to 10%.

In this work, we report on the thermal and optical properties of PEDOT:PSS thin films. Three types of PEDOT:PSS films have been studied: (i) PEDOT:PSS thin films with different thicknesses; (ii) ZnO NCs/PEDOT:PSS hybrid thin films; (iii) GQDs/PEDOT:PSS hybrid thin films. To the best of our knowledge, the change of thermal conductivity of PEDOT:PSS films versus thickness, and the thermal conductivity of ZnO NCs/PEDOT:PSS hybrid films have not been reported before. Our work tries to fill this gap and provide promising routes for tuning the thermal conductivity of PEDOT:PSS films applied to thermoelectric conversion. Mastering how to tune the thermal conductivity and understanding the reason for thermal conductivity changes are important for optimizing ZT. Furthermore, our investigation of the optical properties of these films is relevant for optimizing organic electronics including organic solar cells and organic field-effect transistors because it helps to model the optical behavior of these devices.

5.2 Thermal conductivity of PEDOT:PSS thin films with thickness gradients

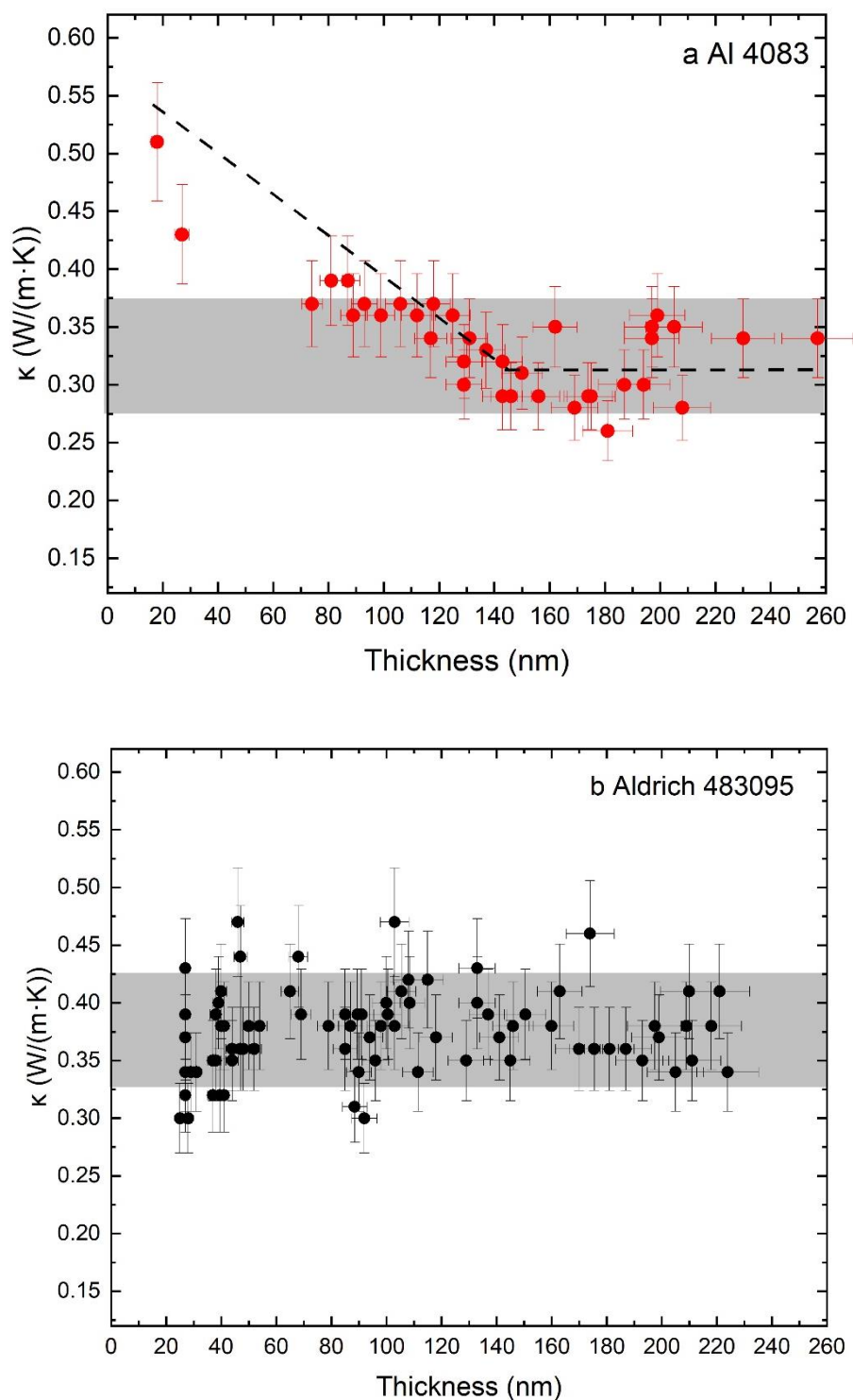


Figure 5.1 Out-of-plane thermal conductivity of blade-coated PEDOT:PSS films measured by FDTR as a function of the film thickness. (a) Al 4083; (b) Aldrich 483095. Dashed line is a guide to the eyes.

Figure 5.1 shows the dependence of the out-of-plane thermal conductivity (κ_{\perp}) on the film thickness in blade-coated PEDOT:PSS films for two different commercially available PEDOT:PSS formulations. The measured thermal conductivity data are mostly located in the grey areas. With the decrease of the film thickness, the thermal conductivity of Al 4083 films remains stable at around 0.31 W/(m·K) at first before starting to rise when the thickness reaches down to 140 nm, exhibiting a maximum value of 0.51 W/(m·K) in the thinnest film point. On the other hand, we did not observe a similar thermal conductivity change in Aldrich 483095 films within our measurement accuracy, as depicted in Fig. 5.1.b. The average thermal conductivity of Aldrich 483095 films is around 0.37 W/(m·K).

What is the origin of the change in thermal conductivity with thickness observed in Fig. 5.1.a.? And why do these two types of PEDOT:PSS films display different thermal conductivity dependence with film thickness? In order to answer these questions, let us consider which physical magnitudes can influence the result. Three possible mechanisms are proposed. Firstly, charge carriers affect the thermal conductivity. We measured the electrical conductivity of Aldrich 483095 films (See Fig. 5.2) and used the maximum value to calculate the electronic contribution to thermal conductivity (κ_e) according to the Wiedemann-Franz law. The resulting κ_e is 1.6×10^{-3} W/(m·K). As we introduced in the first chapter, the thermal conductivity has contributions from the electronic part (charge carriers) and the lattice part (phonons). In this case, the contribution to the thermal conductivity from the electronic part is much smaller than the measured one. Therefore, the detected thermal conductivity of Aldrich 483095 films is dominated by the phonon contribution. The same holds true for Al 4083 films, since they are even less electrically conductive than Aldrich 483095 films. The second possible mechanism is that structural variations lead to the thermal conductivity change. Last but not least, morphology change may also play a role in the change of thermal conductivity of PEDOT:PSS films. To evaluate the structural modifications as function of PEDOT:PSS film thickness, Raman spectroscopy and AFM measurements were performed.

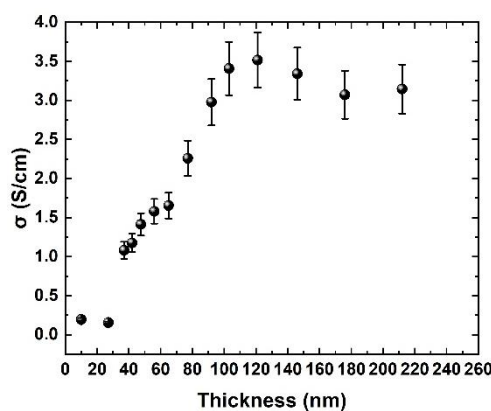


Figure 5.2 Electrical conductivity of PEDOT:PSS (Aldrich 483095) films versus thickness.

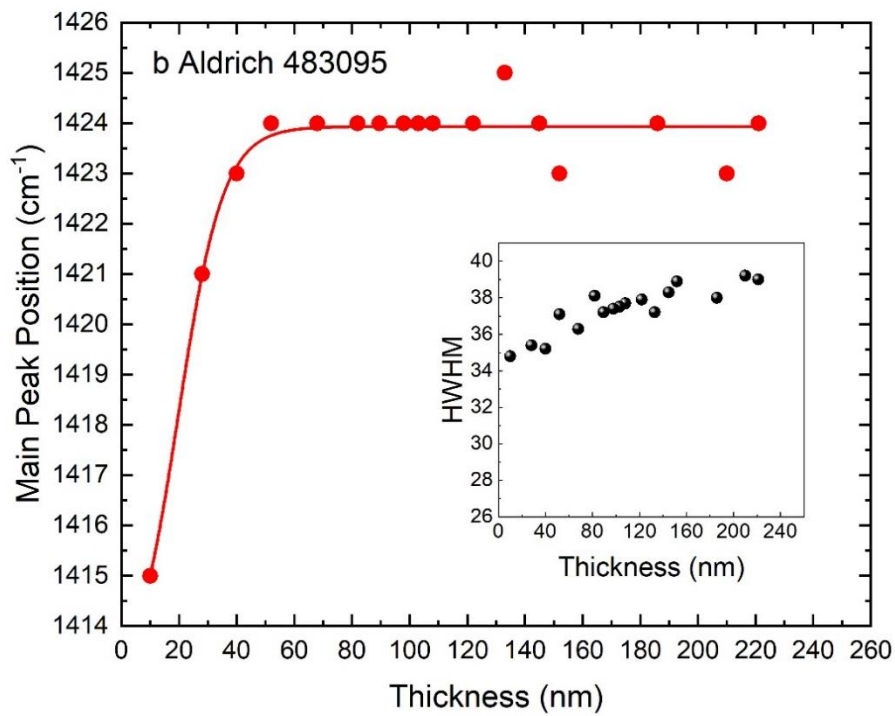
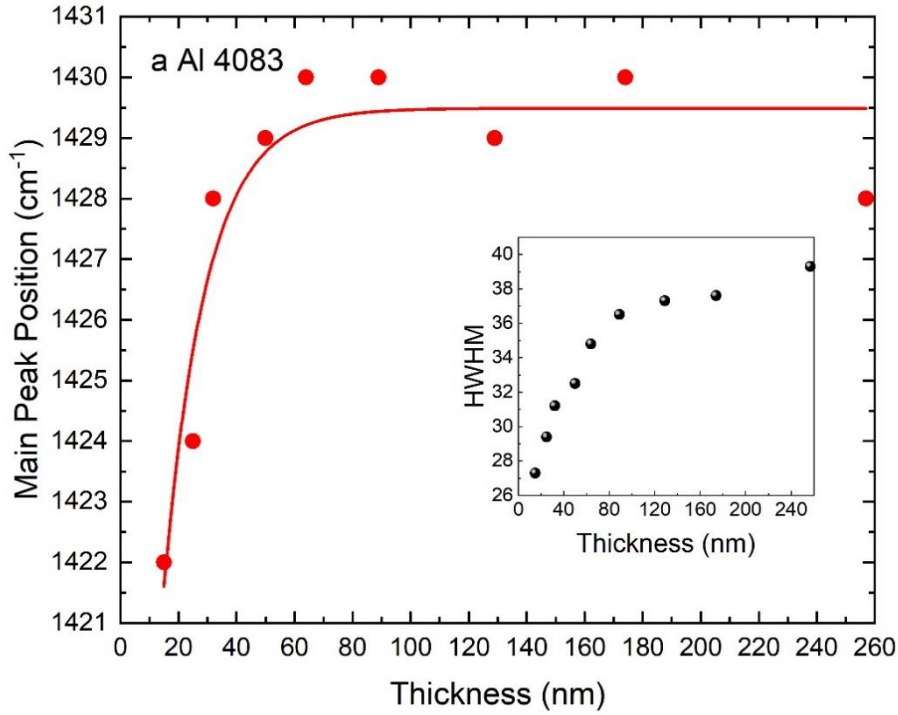


Figure 5.3 Main peak position versus thickness in the Raman spectra of PEDOT:PSS films. (a) Al 4083; (b) Aldrich 483095. The insets show the main peak linewidth.

Figure 5.3 shows the main peak position versus the film thickness in the Raman spectra of PEDOT:PSS films (shown in Fig. 3.6). The main peak which is assigned to the symmetric $C_{\alpha}=C_{\beta}$ stretching gradually shifts to a lower wavenumber with the decrease of

the thickness, spanning about 8 cm^{-1} and 10 cm^{-1} total shift in AI 4083 films and Aldrich 483095 films, respectively. Generally, a red shift in Raman spectra indicates an increased average conjugation length. This is possibly due to the decrease of doping level of PEDOT chains from bipolaron to polaron or neutral state^{104,105}. The thin films tend to be more ordered resulting from improved alignment of the fibrils in the PEDOT:PSS domains.

The insets represent the change in main peak linewidth with the thickness. The most intense band becomes narrower as the thickness decreases. The linewidth of AI 4083 films decreases from 39.3 to 27.3, while the linewidth of Aldrich 483095 films decreases by less, from 39 to 34.8. The linewidth of the most intense band arises from the distribution of conjugation lengths. A narrower band implies a more homogeneous distribution of conjugated domains, which is probably the main mechanism for the enhancement of the thermal conductivity of AI 4083 films. As depicted in the inset of Fig. 5.3.a, the linewidth of the most intense band decreases slightly from 39.3 to 37.3 as the thickness decreases from 240 nm to 130 nm, and then it declines rapidly from 37.3 to 27.3 in the thickness range of (0-130) nm. As a result, with the decrease of the thickness, the thermal conductivity of AI 4083 films keeps stable at first before rising remarkably. Likewise, the thermal conductivity of Aldrich 483095 films almost does not change which correlates with the small linewidth change in the whole thickness range.

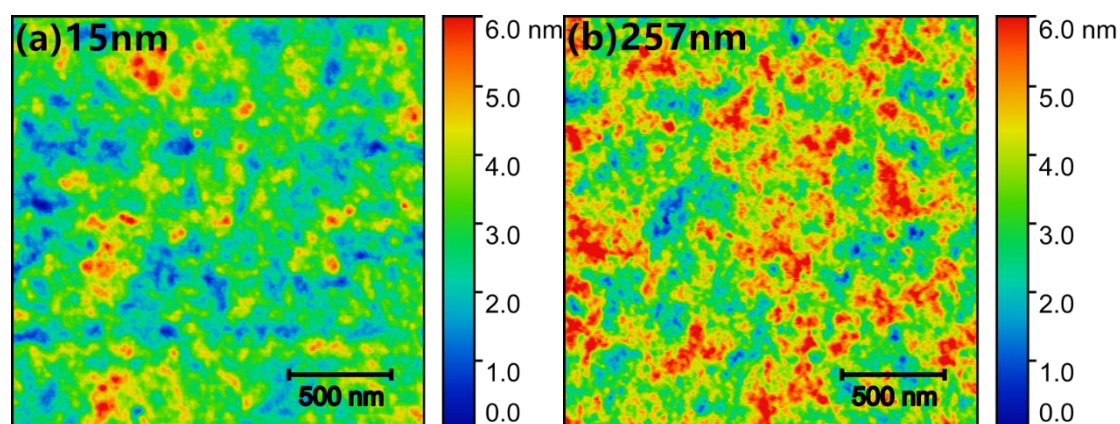


Figure 5.4 Topography images of PEDOT:PSS (AI 4083) films with different thicknesses. (a) 15 nm, Root mean square roughness (sq) = 0.88 nm; (b) 257 nm, sq = 1.1 nm. All images depict an area of $2 \times 2\ \mu\text{m}^2$. Scale bars represent 500 nm.

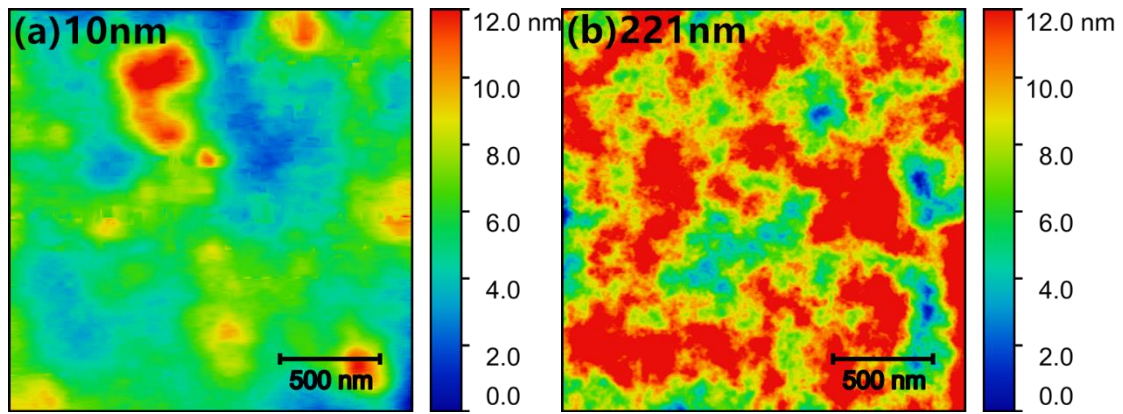


Figure 5.5 Topography images of PEDOT:PSS (Aldrich 483095) films with different thicknesses. (a) 10 nm, $sq=1.8$ nm; (d) 221 nm, $sq=2.9$ nm. All images depict an area of $2 \times 2 \mu\text{m}^2$. Scale bars represent 500 nm.

The surface topography of PEDOT:PSS films was measured by AFM. Fig. 5.4 and Fig. 5.5 demonstrate the morphology of AI 4083 films and Aldrich 483095 films, respectively. The observed roughnesses are 0.88 nm (Fig. 5.4.a), 1.1 nm (Fig. 5.4.b), 1.8 nm (Fig. 5.5.a), and 2.9 nm (Fig. 5.5.b). The topography images of both PEDOT:PSS formulations similarly highlight the growing roughness and the bigger phase separation between PEDOT:PSS grains and excess PSS with increasing film thickness, i.e. the thin films are more homogeneous than thick films. This good homogeneity may have an influence on the high thermal conductivity of thin AI 4083 films. On the other hand, although the homogeneity of Aldrich 483095 films also changes with the thickness, the thermal conductivity of Aldrich 483095 films does not increase. Accordingly, it can be concluded that the morphology of PEDOT:PSS films does not affect their thermal conductivity.

In sum, the thermal conductivity of PEDOT:PSS (AI 4083) films can be significantly enhanced by decreasing the film thickness. As indicated by Raman measurements, this remarkable enhancement is attributed to more homogeneous distribution of conjugated domains.

5.3 Characterization of ZnO nanocrystals and nanowires

We considered two different possibilities of ZnO nano-objects to mix with PEDOT:PSS and form hybrid films, nanocrystals and nanowires. Their synthesis was described in Chapter 2.4 and their characterization is discussed in the following.

The synthesized ZnO nanocrystals were deposited on silicon substrates and measured with spectroscopic ellipsometry to evaluate the size of the ZnO NCs. The fitted thicknesses of one-layer and four-layer ZnO NCs films were 6 nm and 19 nm, respectively. Thus, a linear thickness dependence on the layer numbers was observed which gave a rough estimate of the size of ZnO NCs, around 5 nm.

The spectral absorption coefficient of the ZnO NCs detected from 1/13 ZnO NCs/PEDOT:PSS hybrid film by ellipsometry is shown in Figure 5.6. The inset displays the theoretical dependence of ZnO NCs radius on the absorption wavelength^{106,107}. The broad band centered at 356 nm from the ensemble of ZnO NCs in our film is consistent with an average diameter of 5 nm according to the theoretical calculation^{106,107}, and is in good agreement with the above estimated size.

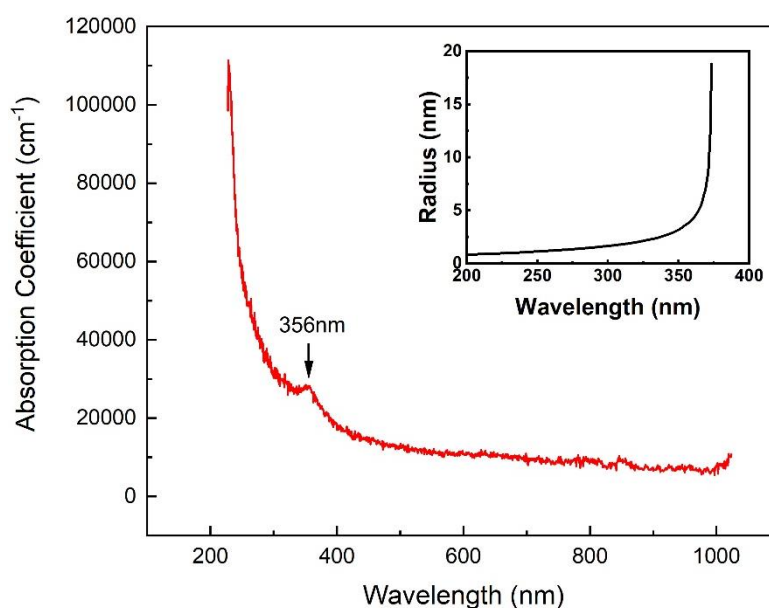


Figure 5.6 Optical absorption coefficient spectrum of ZnO nanocrystals detected from 1/13 ZnO NCs/PEDOT:PSS hybrid film by ellipsometry. The inset displays the theoretical dependence of ZnO nanocrystals radius on the absorption wavelength^{106,107}.

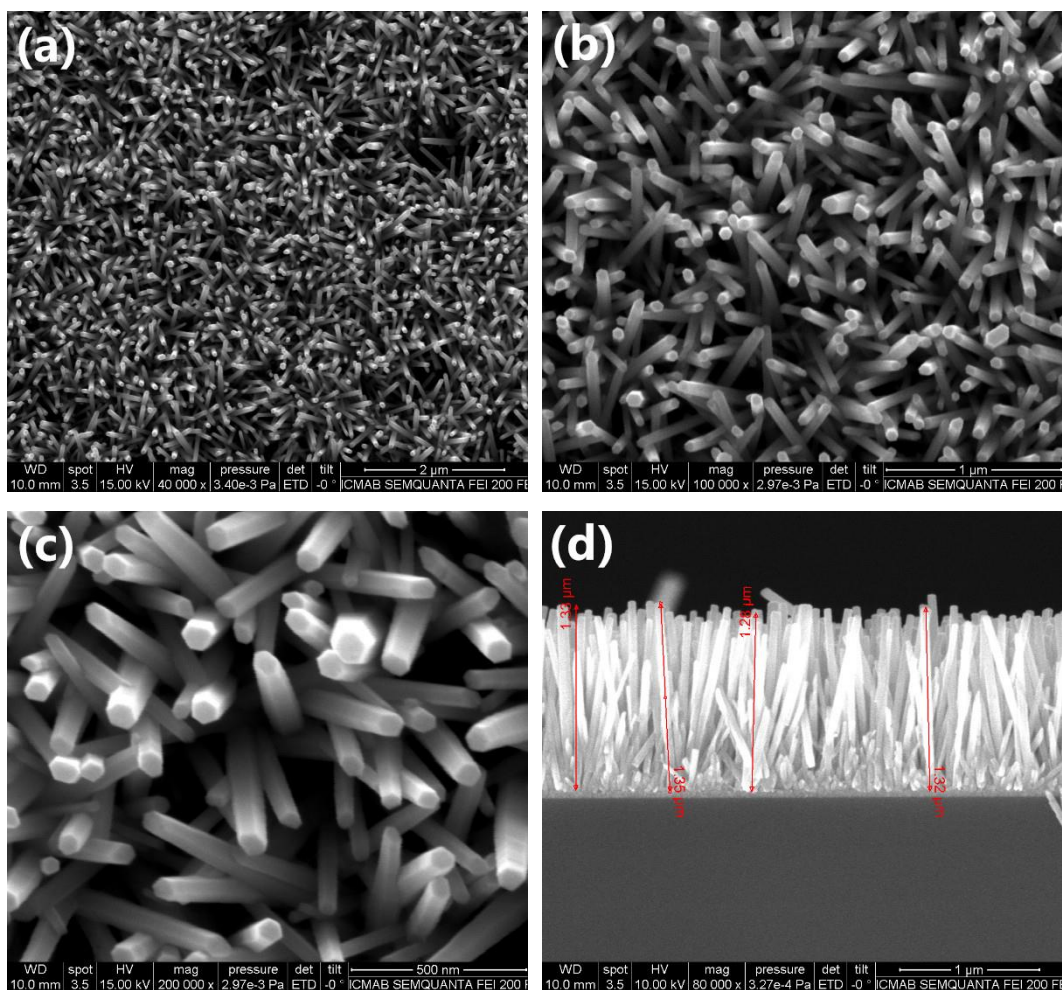


Figure 5.7 SEM images of ZnO nanowire arrays synthesized by hydrothermal method. (a) to (c), Top view. Scale bars are 2 μm , 1 μm and 500 nm, in turn. (d) Cross-sectional view. Scale bar is 1 μm . These images are representative of the entire surface.

The morphology of ZnO nanowire arrays was characterized by scanning electron microscopy (see Fig. 5.7). As we can see from images (a), (b), (c), ZnO NW arrays are uniformly distributed on the substrate. The cross section of a single nanowire is hexagonal. The average diameter of single nanowire is around 70 nm. The cross-sectional image of the arrays (Fig. 5.7.d) suggests that ZnO NWs penetrate the nanocrystals layer and grow nearly vertically. The length of ZnO NWs is up to $1.3 \pm 0.1 \mu\text{m}$ after growing for 8 h. Accordingly, the aspect ratio of ZnO NWs approaches 20.

Figure 5.8 shows the Raman spectrum of these same ZnO NWs. The peak at 520.7 cm^{-1} is due to the silicon substrate. The other peaks labelled by arrows are from ZnO NWs. It is reported that ZnO NWs manufactured by the hydrothermal method possess wurtzite structure⁶⁸. Our Raman spectrum is consistent with the literature¹⁰⁸, indicating the hexagonal wurtzite structure of ZnO NWs.

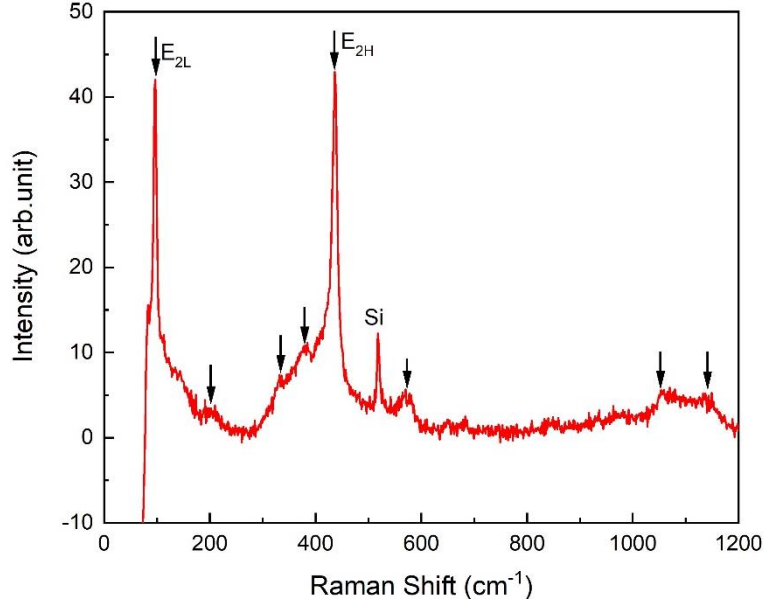


Figure 5.8 Raman spectrum of ZnO nanowires. Excitation wavelength is 532 nm. The peak at 520.7 cm⁻¹ is due to the silicon substrate.

We selected ZnO NCs for the hybrids. There are two reasons for choosing ZnO NCs over NWs. On one hand, ZnO NCs are dispersed in methanol, which is mutually soluble with the solvent of PEDOT:PSS, water. Therefore, it is rather easy to obtain well-mixed ZnO NCs/PEDOT:PSS solutions. On the other hand, the fabrication process of ZnO NWs/PEDOT:PSS hybrid films is quite complicated and more steps are needed: synthesizing nanowires, removing nanowires from the substrate, dispersing them in PEDOT:PSS solution. On balance, we therefore chose ZnO NCs as fillers. In what follows, we report on ZnO NCs/PEDOT:PSS (called ZnO/PEDOT:PSS for short hereafter) hybrid films.

5.4 Optical properties of ZnO/PEDOT:PSS hybrid thin films

Spectroscopic ellipsometry was used to measure the optical properties of ZnO/PEDOT:PSS hybrid thin films. The Drude model was used for fitting the film thickness besides the usual Drude parameters. The metallic-like behavior given by the bipolaron band is described using the Drude model whereas other observed contributions such as the polaron band or interband transitions are added as generalized Lorentzians. Hence, the final model used is:

$$\varepsilon(E) = \varepsilon_{\infty} - \frac{E_p^2}{E^2 + iE\Gamma_p} + \sum_j \frac{A_j e^{i\varphi_j}}{E - E_j + i\Gamma_j} \quad (5.1)$$

where E_p is the plasma energy, Γ_p is Drude broadening, ϵ_∞ is the high frequency dielectric constant. A_j is the amplitude, φ_j is the phase, E_j is the transition energy and Γ_j is the broadening of Lorentz peak j . The Drude parameters are useful to estimate the carrier concentration N_p and mobility μ which are given as follows.

$$N_p(\text{cm}^{-3}) = 7.2525 \times 10^{20} E_p^2 \epsilon_\infty m^* \quad (5.2)$$

$$\mu(\text{cm}^2 / \text{Vs}) = \frac{7.2739}{\Gamma_p m^*} \quad (5.3)$$

where m^* is the effective mass of the charge carriers and both Γ_p and E_p are expressed in eV. The electric resistivity can be calculated using the obtained Drude parameters according to:

$$\rho(\Omega \cdot \text{cm}) = \frac{4\pi h}{\epsilon_0} \frac{\Gamma_p}{\epsilon_\infty E_p^2} = 0.58695 \frac{\Gamma_p}{\epsilon_\infty E_p^2} \quad (5.4)$$

where E_p and Γ_p are expressed in eV.

The thicknesses of the obtained films are listed in Tables 5.1 and 5.2. We used the mass ratio between ZnO NCs and PEDOT:PSS to name samples, and the corresponding ZnO fractions are shown in the tables. The fitted thicknesses using ellipsometry are compared with the ones measured by profilometry. In general, the fitted thicknesses are in good agreement with the profiler thicknesses. The big thickness difference in 1/600 ZnO/AI 4083 film probably results from different probed points. Even if we tried to do both ellipsometer and profiler measurements in a similar position, this was approximate.

Table 5.1 Thicknesses of ZnO/PEDOT:PSS (AI 4083) films

Sample	ZnO fraction	d_prof(nm)	d_ellip(nm)
PEDOT:PSS(AI 4083)	0	109	100
1/600 (Mass ratio of ZnO to PEDOT:PSS)	0.17%	169	114
1/400	0.25%	132	124
1/200	0.5%	200	171
1/100	1%	112	106

Table 5.2 Thicknesses of ZnO/PEDOT:PSS (Aldrich 483095) films

Sample	ZnO fraction	d_prof(nm)	d_ellip(nm)
PEDOT:PSS(Aldrich 483095)	0	94.5	79
1/600	0.17%	87	83
1/400	0.25%	110	86
1/200	0.5%	83	75
1/100	1%	94	80

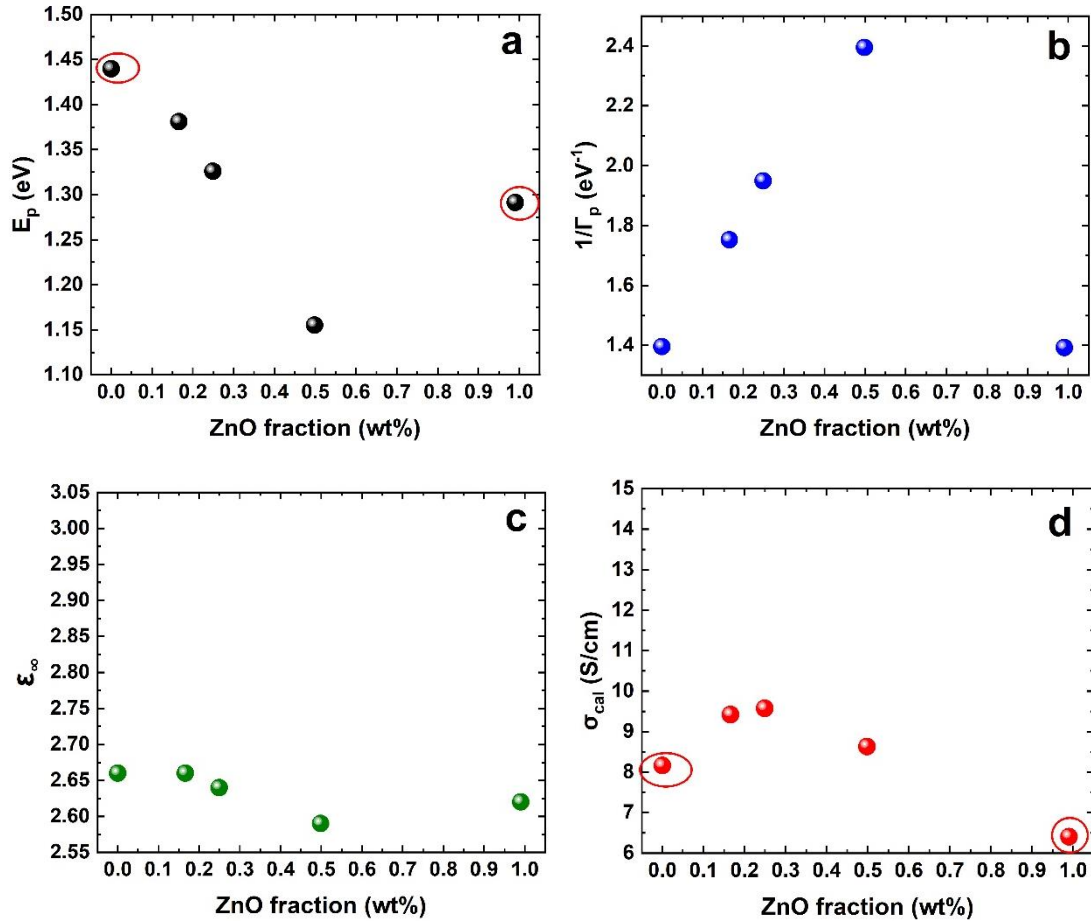


Figure 5.9 Drude parameters and conductivity of ZnO/PEDOT:PSS (AI 4083) films versus ZnO fraction. (a) Plasma energy; (b) Reciprocal of Drude broadening; (c) High frequency dielectric constant; (d) Conductivity calculated from Drude parameters.

Figure 5.9 displays the Drude parameters and conductivity of ZnO/PEDOT:PSS (AI 4083) films versus ZnO fraction. The plasma energy reflects the carrier concentration in terms of Eq. (5.2), to be precise, the bipolaron concentration. The reciprocal of Drude broadening and the high frequency dielectric constant describe the carrier mobility and the electronic density of films, respectively. It is clear from Fig. 5.9 that Drude parameters vary with ZnO fraction. We think the Drude parameters might not only be affected by ZnO fraction but also the film thickness. In order to determine the effect of ZnO fraction separately, we focused on the AI 4083 film and 1/100 ZnO/AI 4083 film as their thicknesses are very close, around 100 nm. As apparent in Figure 5.9.b, the carrier mobility is the same in these two films. However, the plasma energy of the AI 4083 film and 1/100 ZnO/AI 4083 film are 1.44 eV and 1.29 eV, which means the bipolaron concentration goes down with ZnO fraction. The conductivity of the AI 4083 film is higher than that of 1/100 ZnO/AI 4083 film because its bipolaron concentration is higher.

The absorption spectra of the AI 4083 film and 1/100 ZnO/AI 4083 film were measured by ellipsometry (Fig. 5.10). We observed a weak and broad band at 911 nm in the absorption curve of 1/100 ZnO/AI 4083 film. This band is attributed to the polaron absorption according to the conventional DFT theory⁶⁰. However, we did not detect this polaron band in the AI 4083 film, which is in accordance with the widely accepted idea that the charge carriers in PEDOT:PSS films are bipolarons. The appearance of polarons and the decreasing bipolaron concentration illustrate the dedoping of PEDOT chains from bipolaron to polaron with the increase of ZnO fraction.

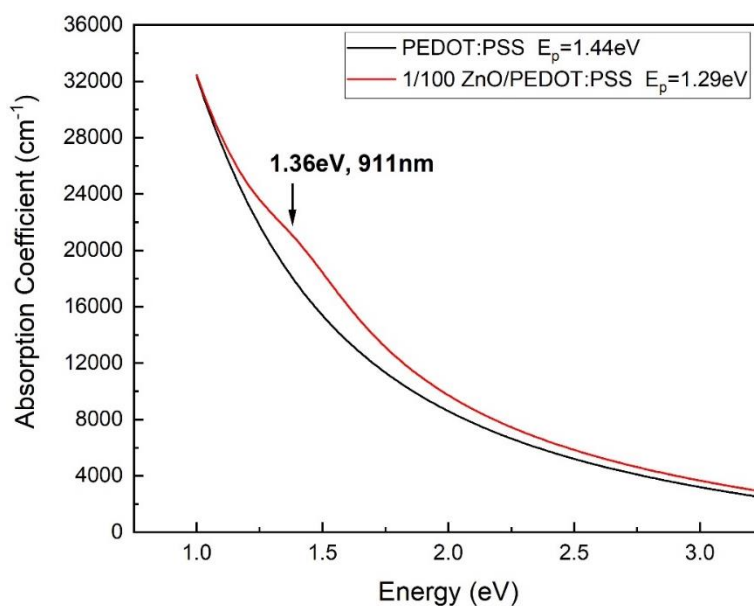


Figure 5.10 Absorption coefficient spectra of PEDOT:PSS (AI 4083) film (black) and 1/100 ZnO/PEDOT:PSS hybrid film (red).

Figure 5.11 illustrates the Drude parameters of the in-plane optical response and corresponding conductivity of ZnO/PEDOT:PSS (Aldrich 483095) films versus ZnO fraction. Since the thicknesses of all films are around 80 nm, the changes in Drude parameters occur because of ZnO fraction change. The plasma energy slightly declines with ZnO fraction, indicating that the bipolaron concentration decreases. The high frequency dielectric constant remains stable with respect to ZnO fraction, which means the electronic density of films hardly changes with ZnO fraction. Furthermore, the reciprocal of Drude broadening increases with respect to ZnO fraction until a maximum followed by a lower plateau. The conductivity displays the same changing rules as the reciprocal of Drude broadening, which indicates that the conductivity of ZnO/Aldrich 483095 films depends on the carrier mobility.

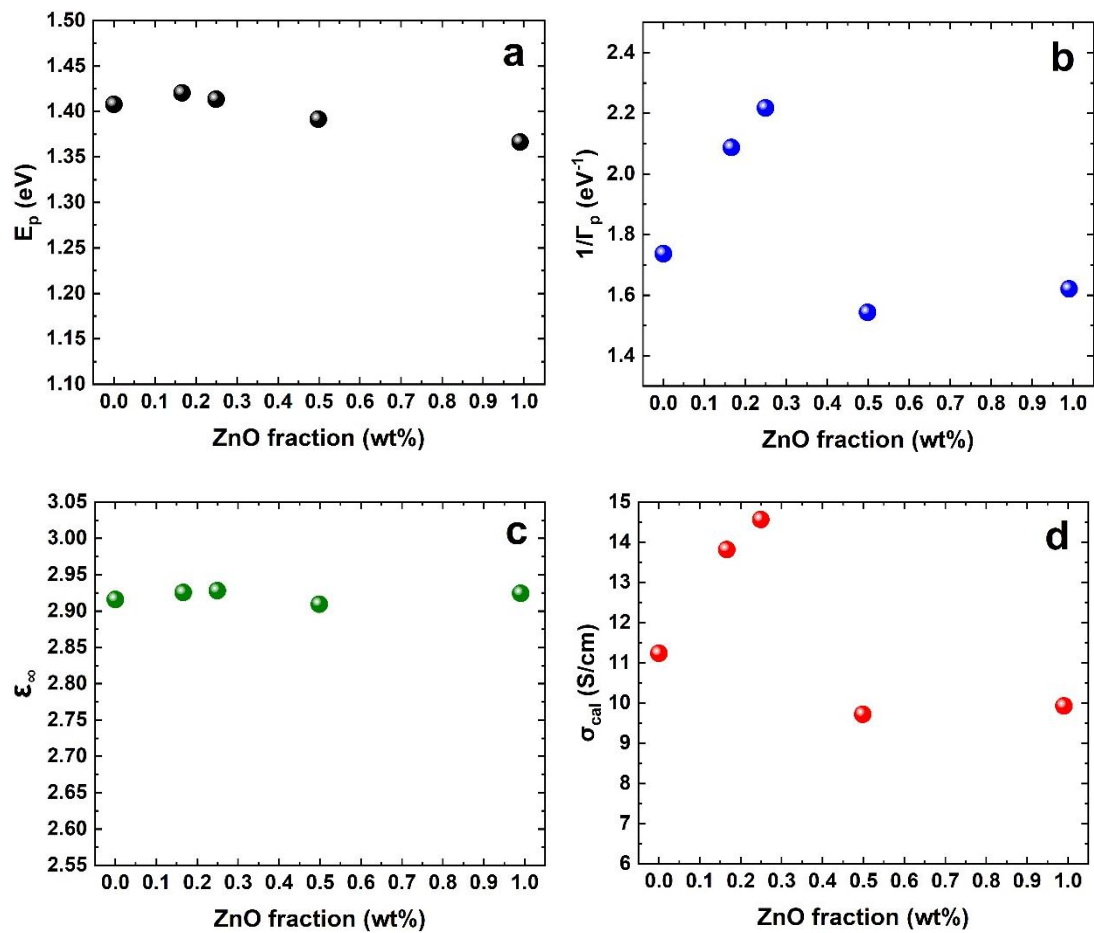


Figure 5.11 Drude parameters of the in-plane optical response and corresponding conductivity of ZnO/PEDOT:PSS (Aldrich 483095) films versus ZnO fraction. (a) Plasma energy; (b) Reciprocal of Drude broadening; (c) High frequency dielectric constant; (d) Conductivity calculated from Drude parameters.

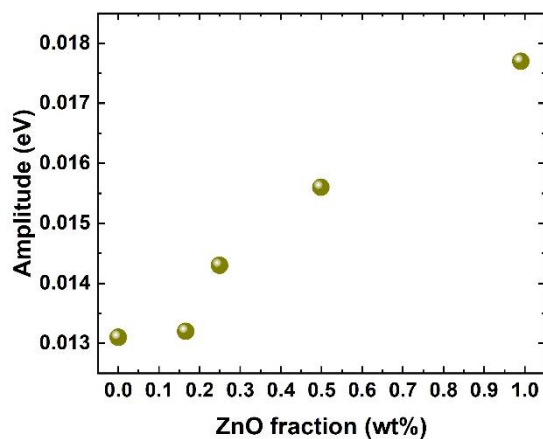


Figure 5.12 Amplitude of the generalized Lorentzian versus ZnO fraction in the ellipsometry fitting of ZnO/PEDOT:PSS (Aldrich 483095) films.

Figure 5.12 depicts the amplitude of the generalized Lorentzian versus ZnO fraction in the ellipsometry fitting of ZnO/PEDOT:PSS (Aldrich 483095) films. The amplitude of the Lorentz peak gives information about the polaron concentration in the films. As apparent in Fig. 5.12, there is an upward trend in the amplitude with the increase of ZnO fraction, suggesting the increasing polaron concentration. Additionally, the bipolaron concentration slightly goes down with ZnO fraction, as described in Fig. 5.11.a. These two results indicate the dedoping of PEDOT chains as ZnO fraction increases.

5.5 Thermal conductivity of ZnO/PEDOT:PSS hybrid thin films

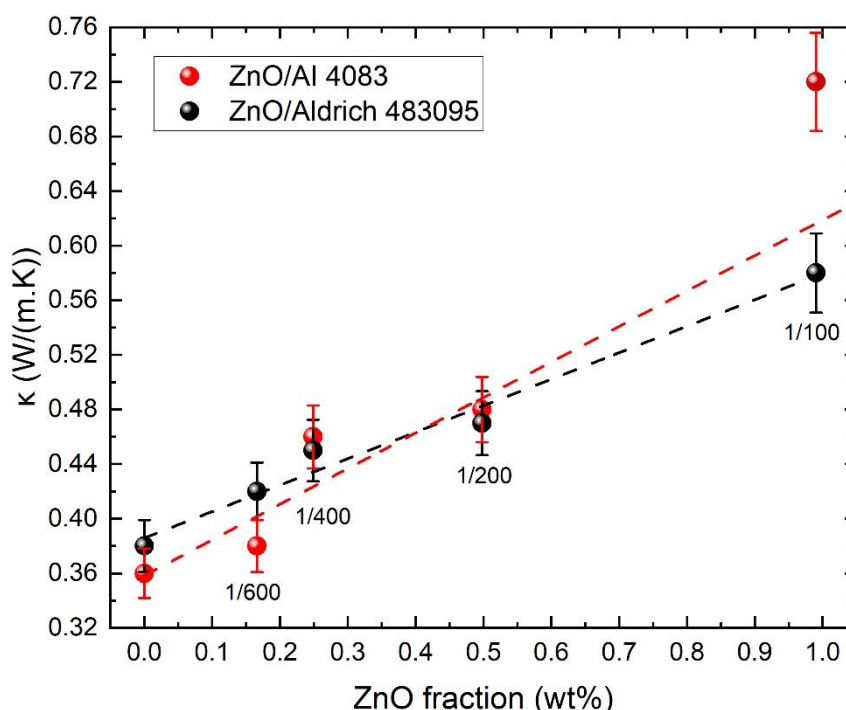


Figure 5.13 Thermal conductivity of blade-coated ZnO/PEDOT:PSS hybrid thin films measured by FDTR as a function of ZnO fraction.

Figure 5.13 illustrates the dependence of the thermal conductivity on ZnO fraction in ZnO/PEDOT:PSS hybrid thin films. Red and black colors represent ZnO/AI 4083 and ZnO/Aldrich 483095 films, respectively. The dashed lines are linear fits to the corresponding data. Adding ZnO significantly increases the thermal conductivity. As ZnO fraction increases from 0 to 1%, a considerable thermal conductivity increase occurs in ZnO/AI 4083 films from 0.36 W/(m·K) to 0.72 W/(m·K), while the thermal conductivity of ZnO/Aldrich 483095 films goes up from 0.38 W/(m·K) to 0.58 W/(m·K).

In order to find the quantitative relation between thermal conductivity and ZnO fraction, we fitted the first four data points of ZnO/AI 4083 films and all five data points of ZnO/Aldrich 483095 films. A linear dependence of thermal conductivity with respect to

ZnO fraction was observed. Stated differently, the composition of ZnO/PEDOT:PSS hybrid films affects the thermal conductivity. An estimation of the thermal conductivity of ZnO nanoparticles was obtained from the slope of the fitted curve. In theory, the thermal conductivity of ZnO nanoparticles in ZnO/AI 4083 and ZnO/Aldrich 483095 films should be the same, i.e. the slopes of two curves should be the same. According to the fitted equations, we obtained the thermal conductivity of ZnO nanoparticles ($\kappa(\text{ZnO})$), 26 W/(m·K) in ZnO/AI 4083 films and 20 W/(m·K) in ZnO/Aldrich 483095 films. These two $\kappa(\text{ZnO})$ values are close although they are not completely equal. If we fitted all five data points of ZnO/AI 4083 films, the $\kappa(\text{ZnO})$ value is 36 W/(m·K), which makes no sense because it is very different from the $\kappa(\text{ZnO})$ in ZnO/Aldrich 483095 films.

The thermal conductivity of ZnO/AI 4083 films increases significantly from 0.48 W/(m·K) to 0.72 W/(m·K) when ZnO fraction rises from 0.5% to 1%. The thermal conductivity of 1/100 ZnO/AI 4083 film is far away from the fitted curve. We deduce there are possibly other factors affecting the thermal conductivity of 1/100 ZnO/AI 4083 film. The composition effect is not the only influencing factor.

In order to find out other factors influencing the thermal conductivity, three possible mechanisms are proposed. Firstly, free carriers affect the thermal conductivity. We measured the electrical conductivity (see Fig. 5.14) and calculated the electronic thermal conductivity in terms of the Wiedemann-Franz law. κ_e is 7.2×10^{-7} W/(m·K) in ZnO/AI 4083 films and 1.3×10^{-5} W/(m·K) in ZnO/Aldrich 483095 films. The electronic contribution to the thermal conductivity was ruled out since the calculated electronic thermal conductivity is much smaller than the measured thermal conductivity. Accordingly, the thermal conductivity of ZnO/PEDOT:PSS composite films is dominated by the phonon contribution. Secondly, structural variations result in the thermal conductivity change. Thirdly, morphology might have an impact on the thermal conductivity.

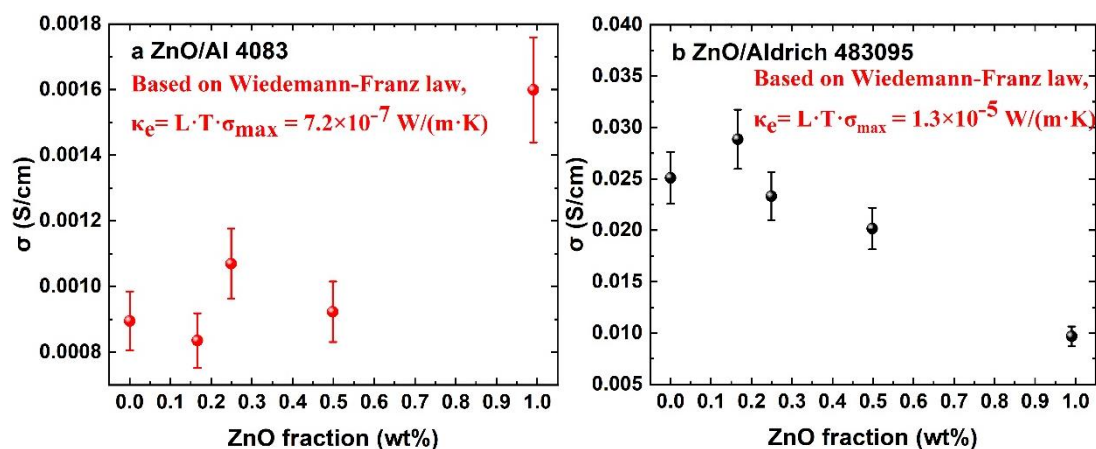


Figure 5.14 Electrical conductivity of ZnO/PEDOT:PSS films versus ZnO fraction. (a) ZnO/AI 4083; (b) ZnO/Aldrich 483095.

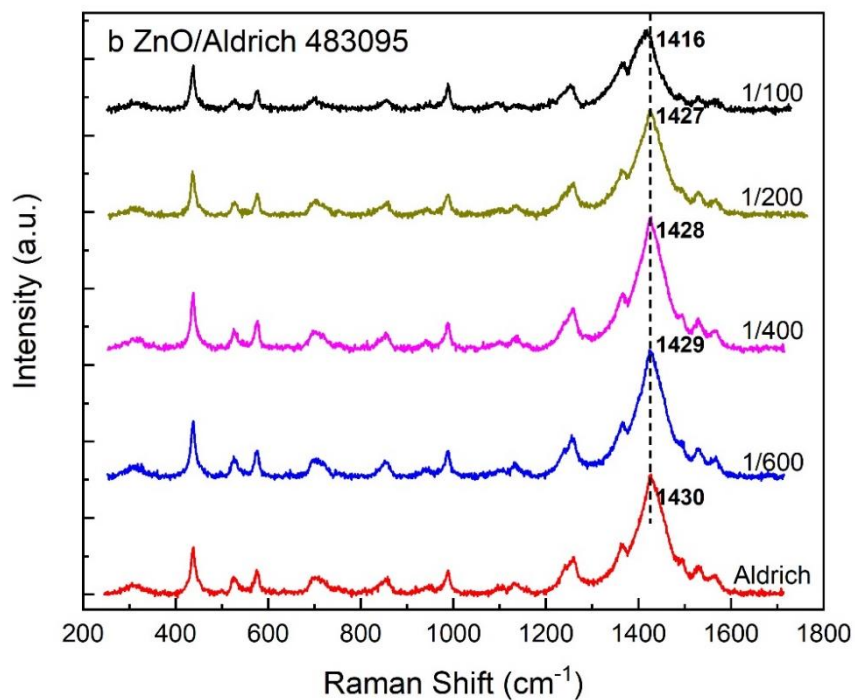
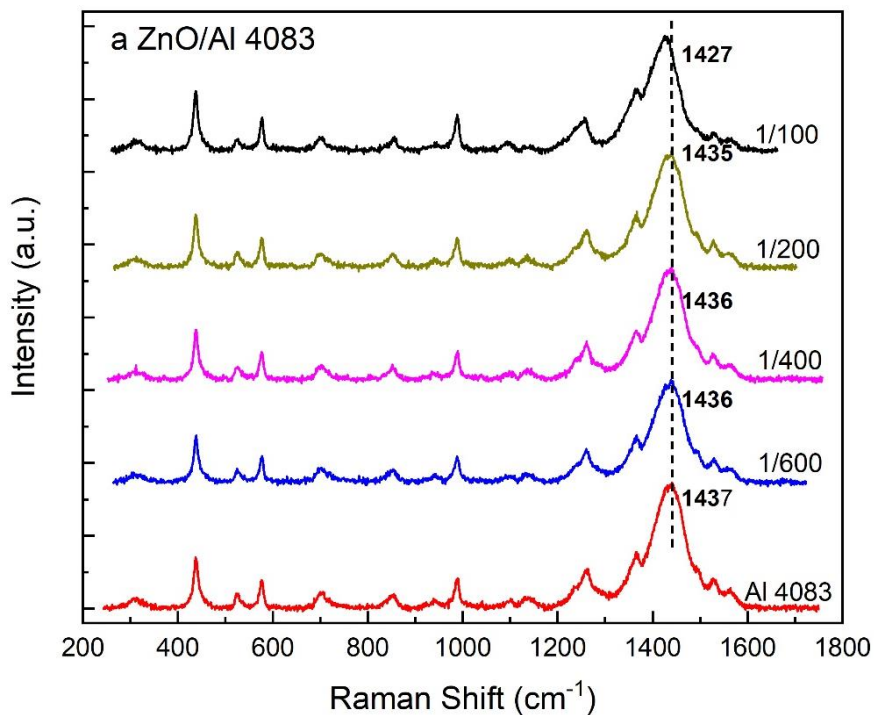


Figure 5.15 Raman spectra of ZnO/PEDOT:PSS films. (a) ZnO/AI 4083; (b) ZnO/Aldrich 483095. The different colors of Raman spectra represent different ZnO fractions. The Raman spectra were offset vertically to improve visibility.

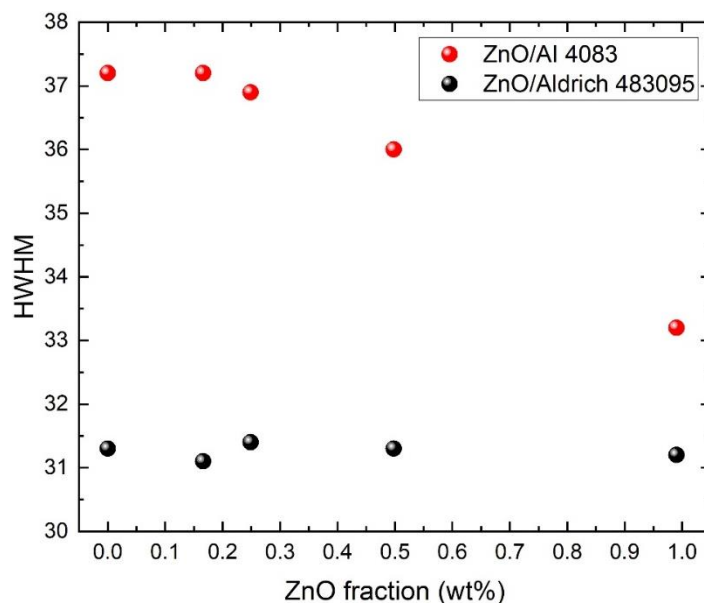


Figure 5.16 Main peak linewidth versus ZnO fraction.

Raman spectroscopy was used to investigate the structure change of PEDOT chains with ZnO fraction. Figure 5.15 depicts the Raman spectra of ZnO/PEDOT:PSS films. With the increase of ZnO fraction, there are red shifts in the symmetric $C_{\alpha}=C_{\beta}$ stretching vibration, from 1437 cm^{-1} to 1427 cm^{-1} for ZnO/AI 4083 films and from 1430 cm^{-1} to 1416 cm^{-1} for ZnO/Aldrich 483095 films. The red shifts are only 2 cm^{-1} (ZnO/AI 4083) and 3 cm^{-1} (ZnO/Aldrich 483095) when ZnO fraction rises from 0 to 0.5%. However, as ZnO fraction increases from 0.5% to 1%, the red shift becomes very clear, 8 cm^{-1} (ZnO/AI 4083) and 11 cm^{-1} (ZnO/Aldrich 483095).

As mentioned before, the red shift in Raman spectra indicates the increased average conjugation length. This is possibly ascribed to the dedoping of PEDOT chains from bipolaron to polaron or neutral state^{104,105}. This dedoping has been confirmed by the ellipsometry results in the section 5.4. PEDOT:PSS domains tend to more ordered as ZnO fraction increases. We think the structure change related to the red shifts is not the reason for the thermal conductivity change. That is because the thermal conductivity of ZnO/Aldrich 483095 films grows from 0.38 (0%) to 0.47 (0.5%), finally reaching at 0.58 (1%). The changing speeds of the thermal conductivity and the Raman shift are not consistent.

Figure 5.16 shows the change in the main peak linewidth with ZnO fraction. It is clear that the linewidth in ZnO/AI 4083 films declines with the ZnO fraction. In particular, the linewidth decreases remarkably from 36 to 33.2 when ZnO fraction rises from 0.5% to 1%. As already discussed, the linewidth of the most intense band arises from the distribution of conjugation lengths. A narrower band implies a more homogeneous distribution of conjugated domains. So it is possible that the improved homogeneity of

conjugated domains in 1/100 ZnO/AI 4083 film results in its high thermal conductivity. On the other hand, we do not observe a significant linewidth change in ZnO/Aldrich 483095 films with different ZnO fractions, which reveals the distribution of conjugation length does not vary. The unchanged distribution of conjugation length is irrelevant to the thermal conductivity change of ZnO/Aldrich 483095 films.

The surface morphology of ZnO/PEDOT:PSS films was investigated using AFM in order to examine its possible impact on the thermal conductivity. Figure 5.17 exhibits the topography images of ZnO/PEDOT:PSS (AI 4083) films. The observed roughnesses are 1.4 nm, 1 nm, 1 nm, 1.7 nm and 2.6 nm from Figure 5.17.a to e. The images indicate the growing roughness and the bigger phase separation between PEDOT:PSS grains and excess PSS with the increase of ZnO fraction. The phase separation in 1/100 ZnO/AI 4083 film is particularly noticeable, indicating bigger aggregation of PEDOT:PSS grains that is possibly induced by the agglomeration of ZnO nanocrystals. The n-type aggregated ZnO nanoparticles combine with p-type PEDOT, causing the phase separation. We are not sure if this phase separation affects the thermal conductivity. It seems that the phase separation does not play a key role in the thermal conductivity of ZnO/AI 4083 films. That is because a rough morphology corresponds to a low thermal conductivity in AI 4083 films, according to the result in the section 5.2. However, the rough 1/100 ZnO/AI 4083 film exhibits the high thermal conductivity in this batch. The topography images of ZnO/PEDOT:PSS (Aldrich 483095) films were pictured in Figure 5.18. The observed roughnesses are 7.5 nm, 8.7 nm, 10 nm, 9 nm and 6 nm from Figure 5.18.a to e. It seems that the morphology of ZnO/Aldrich 483095 films does not change significantly with ZnO fraction.

In sum, the composition of ZnO/PEDOT:PSS films is the main cause affecting their thermal conductivity. The increased homogeneous distribution of conjugated domains accounts for the additional increment of thermal conductivity in the 1/100 ZnO/AI 4083 film.

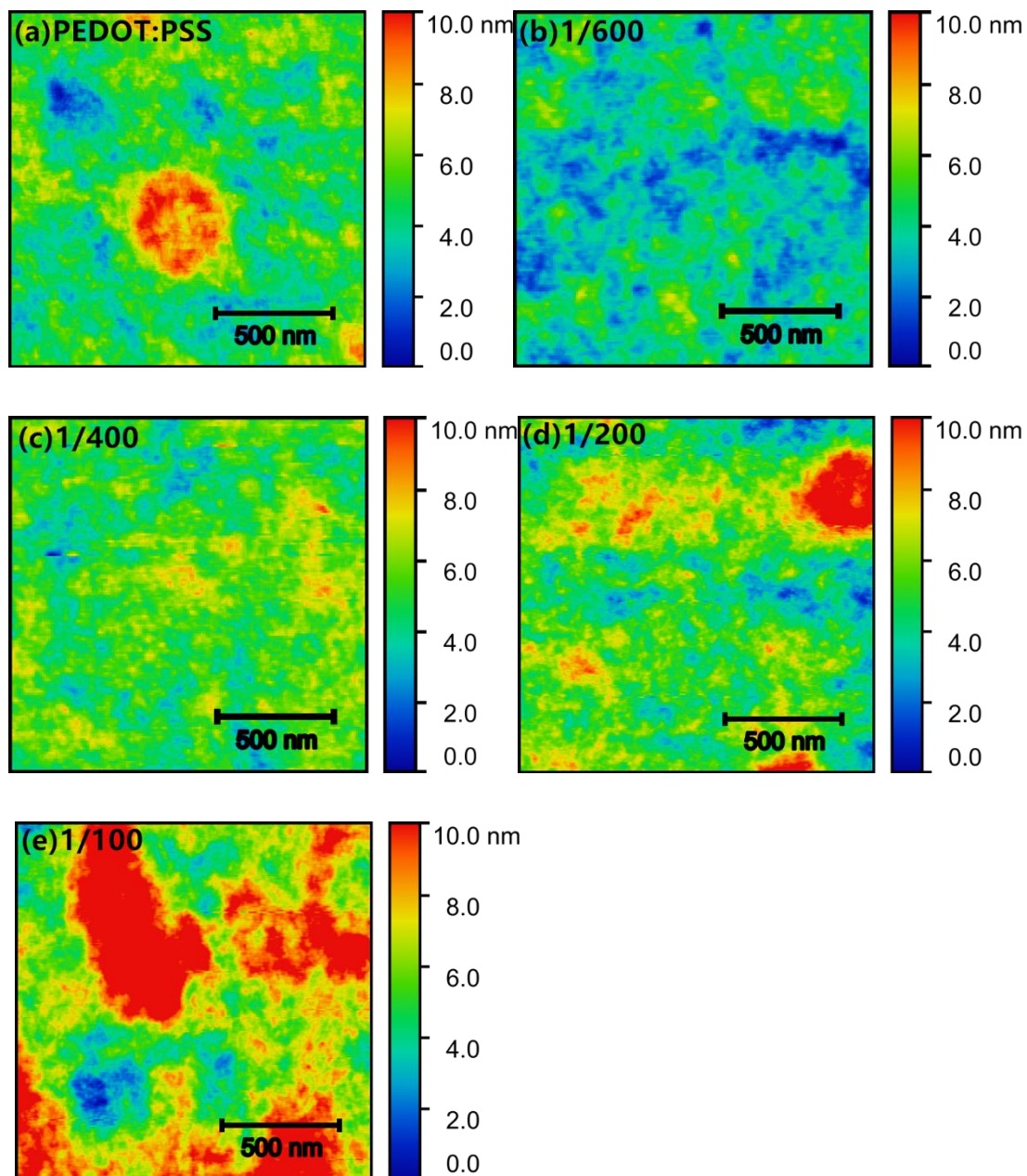


Figure 5.17 Topography images of ZnO/PEDOT:PSS (AI 4083) films. (a) PEDOT:PSS, $sq=1.4$ nm; (b) 1/600, $sq=1.0$ nm; (c) 1/400, $sq=1.0$ nm; (d) 1/200, $sq=1.7$ nm; (e) 1/100, $sq=2.6$ nm. All images depict an area of $1.5 \times 1.5 \mu\text{m}^2$. Scale bars represent 500nm.

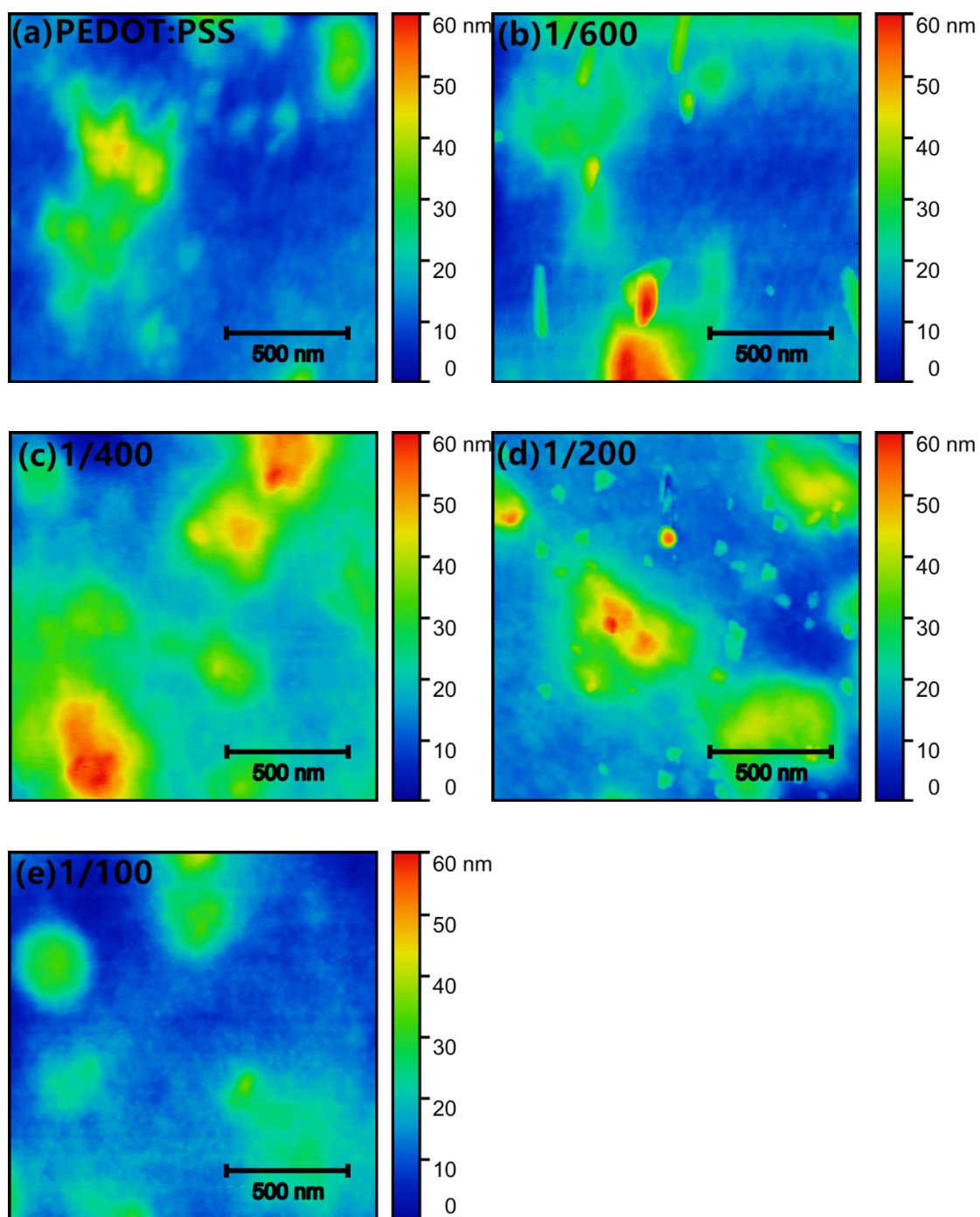


Figure 5.18 Topography images of ZnO/PEDOT:PSS (Aldrich 483095) films. (a) PEDOT:PSS, $sq=7.5$ nm; (b) 1/600, $sq=8.7$ nm; (c) 1/400, $sq=10$ nm; (d) 1/200, $sq=9$ nm; (e) 1/100, $sq=6$ nm. All images depict an area of $1.5 \times 1.5 \mu\text{m}^2$. Scale bars represent 500 nm.

5.6 Optical properties of GQDs/PEDOT:PSS hybrid thin films

Here and hereafter we focus on the case of GQDs/PEDOT:PSS hybrid thin films. Spectroscopic ellipsometry was used to determine the optical properties of GQDs/PEDOT:PSS films. Bruggeman effective medium approximation (**BEMA**) model was used for fitting the relative volume ratio of the components and the film thickness. BEMA model is expressed as follows:

$$f_A \frac{\tilde{\epsilon}_A - \tilde{\epsilon}_{EMA}}{\tilde{\epsilon}_A + 2\tilde{\epsilon}_{EMA}} + f_B \frac{\tilde{\epsilon}_B - \tilde{\epsilon}_{EMA}}{\tilde{\epsilon}_B + 2\tilde{\epsilon}_{EMA}} = 0 \quad (5.5)$$

where $\tilde{\epsilon}_{EMA}$ is the effective complex dielectric function of the composite material, $\tilde{\epsilon}_A$ and $\tilde{\epsilon}_B$ are the complex dielectric functions of component A and B, f_A and f_B are the volume fractions of A and B. Although GQDs/PEDOT:PSS is actually a three-component system, we assumed it as a two-component system in which PEDOT:PSS is regarded as a single material. Note that PEDOT:PSS cannot be modelled using BEMA because its components interact. Moreover, since Aldrich 483095 films show pronounced optical anisotropy, we considered the isotropic GQDs phase for each one of the PEDOT:PSS components with a common volume fraction for both during the regression analysis. To summarize the fitted anisotropy, we indicate the birefringence $\Delta n = n_e - n_o$ at some arbitrary energy which seems representative, in this case 2 eV.

Table 5.3 Ellipsometry results of GQDs/PEDOT:PSS (AI 4083) films based on BEMA model

Sample	vf(GQDs)_set	vf(GQDs)_fit	d_prof (nm)	d_fit (nm)
PEDOT:PSS (AI 4083)	0	0.02	55.5	68.5
1/10 (Mass ratio of GQDs to PEDOT:PSS)	0.09	0.09	79	82.7
1/2	0.33	0.33	68	74.9
1/1	0.5	0.4	89	110
GQDs	1	1	/	>5000

Table 5.4 Ellipsometry results of GQDs/PEDOT:PSS (Aldrich 483095) films based on BEMA model

Sample	vf(GQDs)_set	vf(GQDs)_fit	d_prof (nm)	d_fit (nm)	Δn (2 eV)
PEDOT:PSS (Aldrich 483095)	0	0.002	60	52.9	0.32
1/10	0.09	0.1	67	52.1	0.32
1/2	0.33	0.35	59	52.5	0.2
1/1	0.5	0.65	67	66.8	0.02

Tables 5.3 and 5.4 show the fitting results of GQDs/PEDOT:PSS films based on BEMA model. The fitted GQDs fractions are in good agreement with the set values in the fabrication process, which means GQDs are well dispersed in the hybrid films. However, the largest difference between the fitted value and the set value lies in 1/1 films. One possible reason is that GQDs did not disperse very well in 1/1 films. This fact tells us that the maximum GQDs fraction is between 33% and 50% in order to obtain homogeneous composite films. Anyway, the fraction differences are acceptable because they are not big. Moreover, we note that the fitted GQDs fractions in PEDOT:PSS films are 0.02 (AI 4083) and 0.002 (Aldrich 483095) which represent the small fitting errors. In addition, the fitted film thicknesses are consistent with the ones from profiler. More importantly, it is revealed that the anisotropy of PEDOT:PSS (Aldrich 483095) films is reduced by mixing with GQDs. When the GQDs fraction is 50%, the GQDs/Aldrich 483095 composite film becomes isotropic.

The complex refractive index was determined for GQDs/PEDOT:PSS films (see Fig. 5.19 and Fig. 5.20).

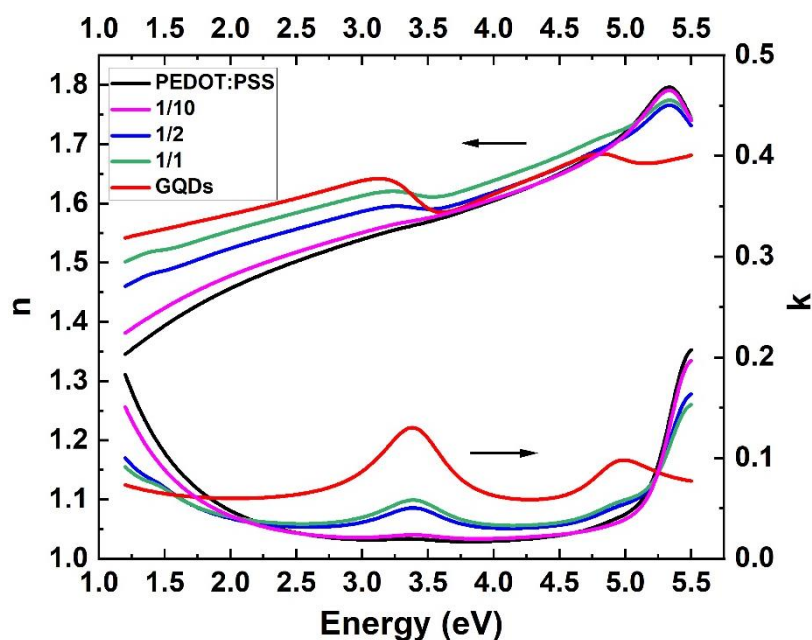


Figure 5.19 Complex refractive index of GQDs/PEDOT:PSS (AI 4083) films.

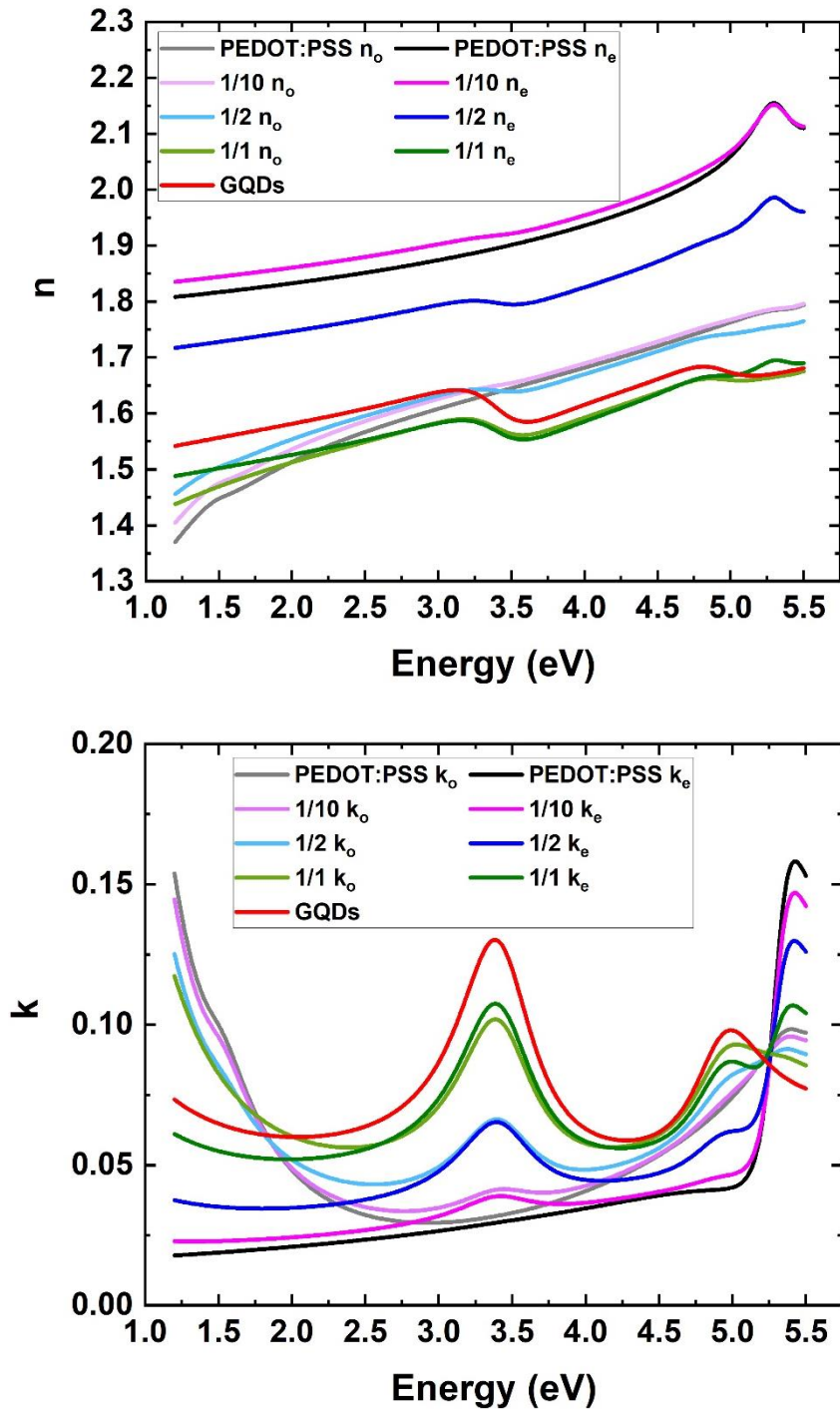


Figure 5.20 Complex refractive index of GQDs/PEDOT:PSS (Aldrich 483095) films.

Drude model (Eq. 5.1) was used to fit the film thickness and the usual Drude parameters of GQDs/AI 4083 films. Fitted parameters from the Drude model provide further insights on the influence of GQDs concentration on the investigated electrical properties. Here, we do not show the fitted thicknesses any more since they are almost the same as the ones from BEMA model. Figure 5.21 exhibits the Drude parameters and conductivity of

GQDs/AI 4083 films versus GQDs fraction. The plasma energy decreases linearly with GQDs fraction, suggesting the decreasing bipolaron concentration in the composite films. On the other hand, the high frequency dielectric constant rises linearly, which means the electronic density of composite films increases with GQDs fraction. Moreover, the Drude broadening changes slightly with GQDs fraction, fluctuating between 0.65 eV and 0.85 eV. This implies that the carrier mobility remains stable with GQDs fraction. However, there is a downward trend in the conductivity. It can be concluded that the main factor that controls the conductivity of GQDs/AI 4083 films is the plasma energy, i.e. the bipolaron concentration.

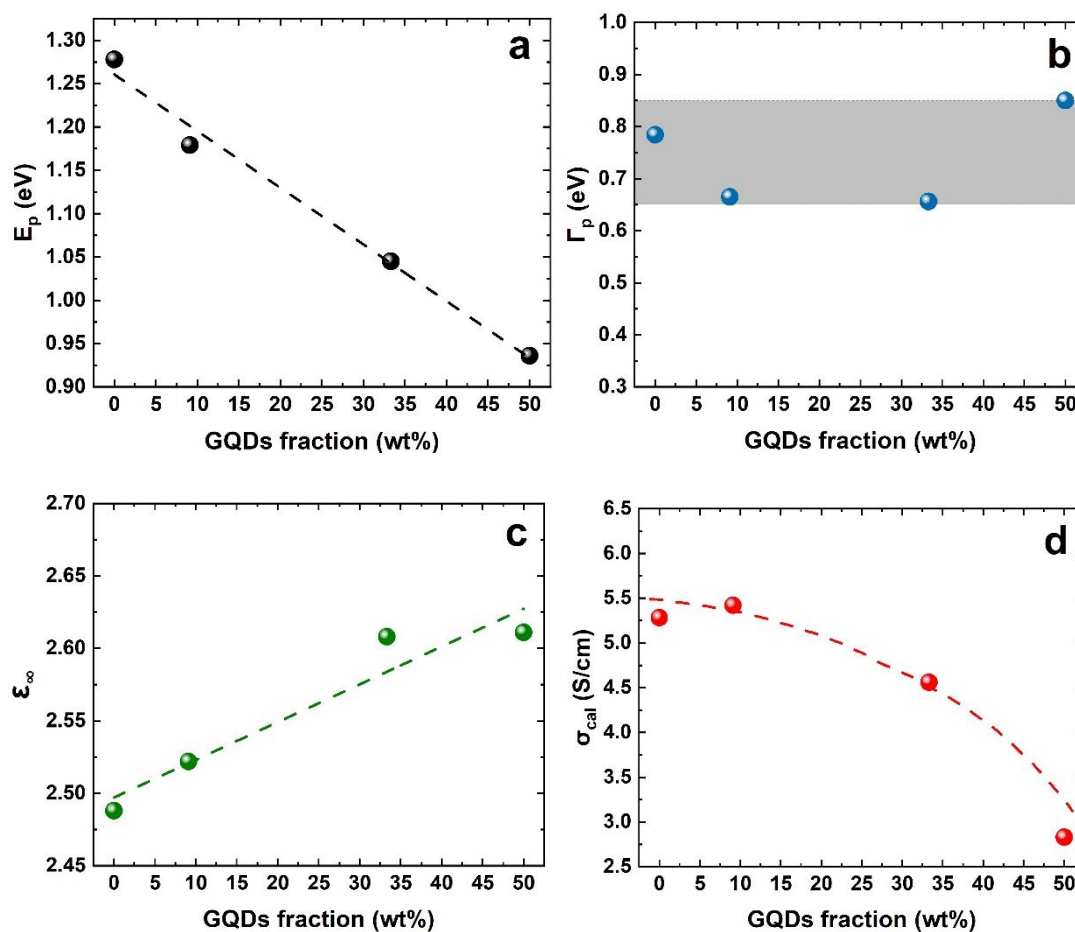


Figure 5.21 Drude parameters and conductivity of GQDs/PEDOT:PSS (AI 4083) films versus GQDs fraction. (a) Plasma energy; (b) Drude broadening; (c) High frequency dielectric constant; (d) Conductivity calculated from Drude parameters.

Table 5.5 Ellipsometry results of GQDs/PEDOT:PSS (AI 4083) films based on Drude model. "A" represents the amplitude of the generalized Lorentzian.

Sample	A (eV)
PEDOT:PSS (AI 4083)	/
1/10	0.007
1/2	0.006
1/1	0.007

Table 5.5 shows the fitting results of GQDs/PEDOT:PSS (AI 4083) films based on Drude model. "A" represents the amplitude of the generalized Lorentzian, which describes the polaron concentration. It is clear that polarons appear in the hybrid films, whereas it is not detectable in the AI 4083 film. The appearance of polarons and the decreasing bipolaron concentration reveal the dedoping of PEDOT chains from bipolaron to polaron as GQDs fraction increases.

5.7 Thermal conductivity of GQDs/PEDOT:PSS hybrid thin films

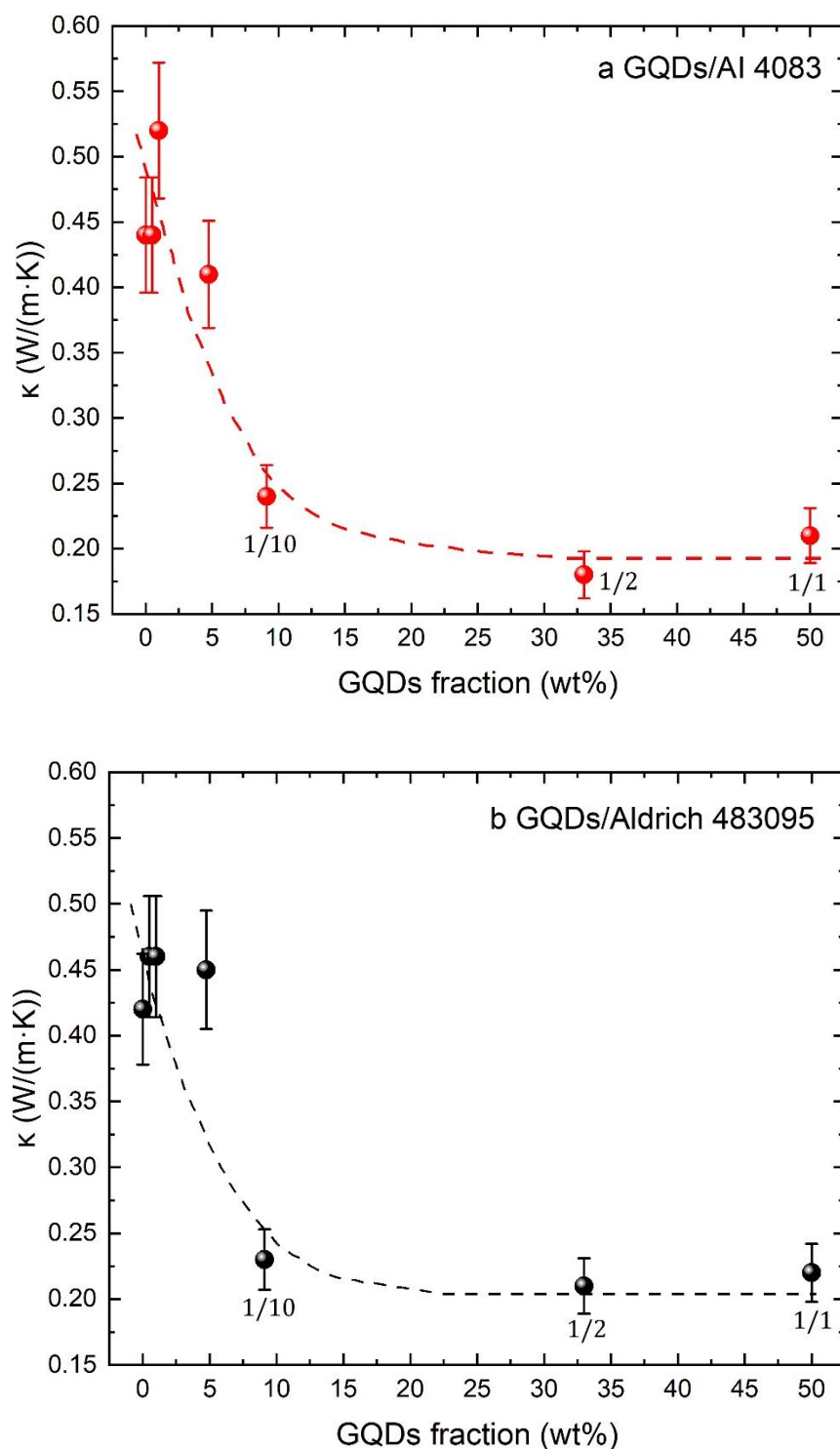


Figure 5.22 Thermal conductivity of blade-coated GQDs/PEDOT:PSS hybrid thin films measured by FDTR as a function of GQDs fraction. (a) GQDs/AI 4083; (b) GQDs/Aldrich 483095. Dashed lines are a guide to the eyes.

Figure 5.22 illustrates the dependence of the thermal conductivity on GQDs fraction in GQDs/PEDOT:PSS hybrid thin films. The thermal conductivity decreases rapidly when adding 0-10 wt% GQDs in the PEDOT:PSS solution and reaches a plateau with additional GQDs. GQDs/AI 4083 films and GQDs/Aldrich 483095 films display a similar changing trend.

In order to find out the reason for the thermal conductivity change, we firstly verified the effect of charge carriers on the thermal conductivity. The electrical conductivity of GQDs/PEDOT:PSS films was measured and the results are shown in Fig. 5.23. We calculated the electronic thermal conductivity using the maximum value of the electrical conductivity in terms of the Wiedemann-Franz law. The resulting κ_e is $8.9 \times 10^{-6} \text{ W}/(\text{m}\cdot\text{K})$ in GQDs/AI 4083 films and $1.1 \times 10^{-5} \text{ W}/(\text{m}\cdot\text{K})$ in GQDs/Aldrich 483095 films. The electronic contribution to the thermal conductivity was ruled out since the calculated electronic thermal conductivity is much smaller than the measured one. Thus the thermal conductivity of GQDs/PEDOT:PSS films is dominated by the phonon contribution.

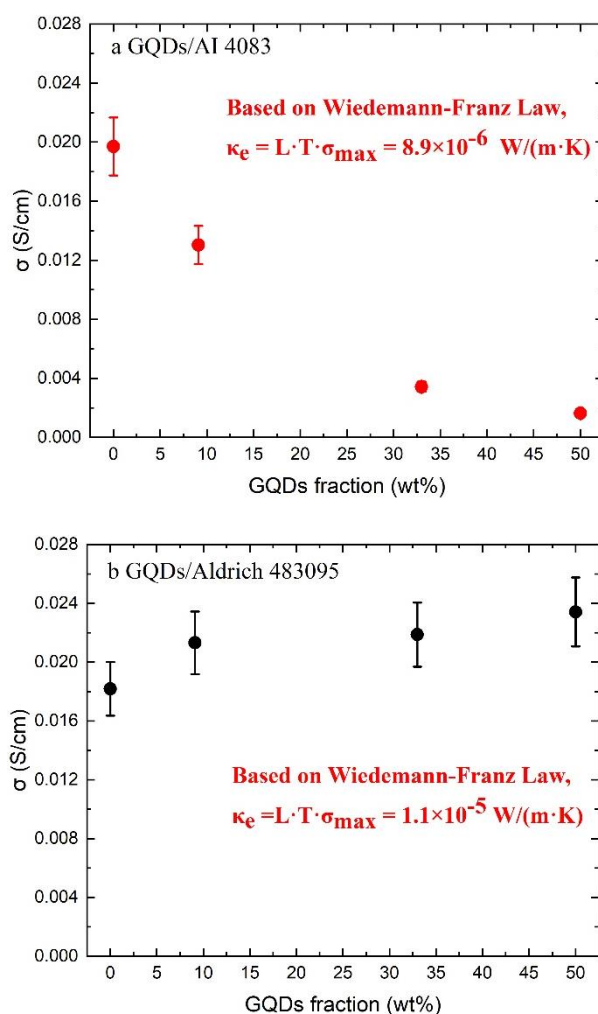


Figure 5.23 Electrical conductivity of GQDs/PEDOT:PSS films versus GQDs fraction. (a) GQDs/AI 4083; (b) GQDs/Aldrich 483095.

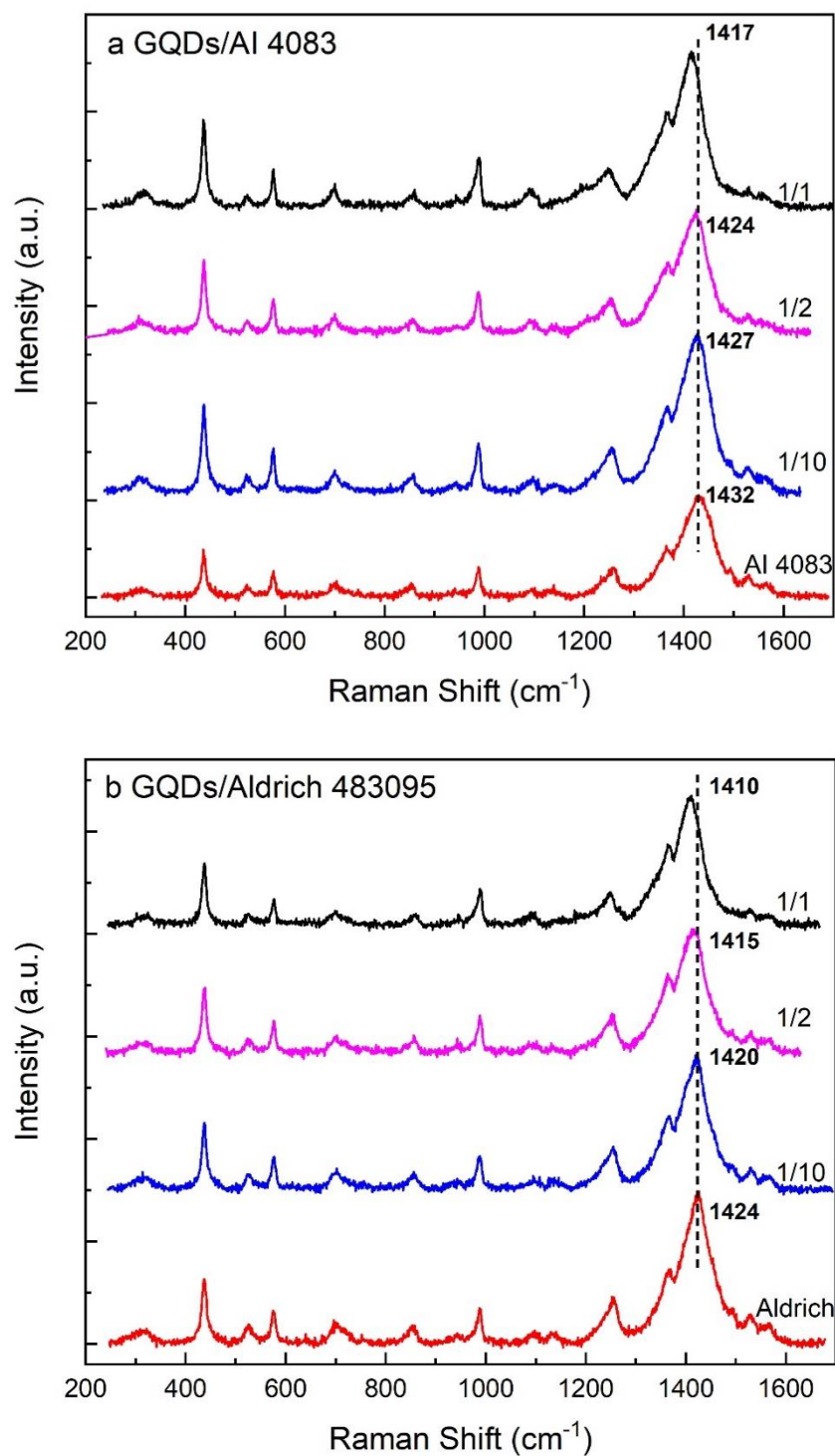


Figure 5.24 Raman spectra of GQDs/PEDOT:PSS films. (a) GQDs/AI 4083; (b) GQDs/Aldrich 483095. The different colors of Raman spectra represent different GQDs fractions. The Raman spectra were offset vertically to improve visibility.

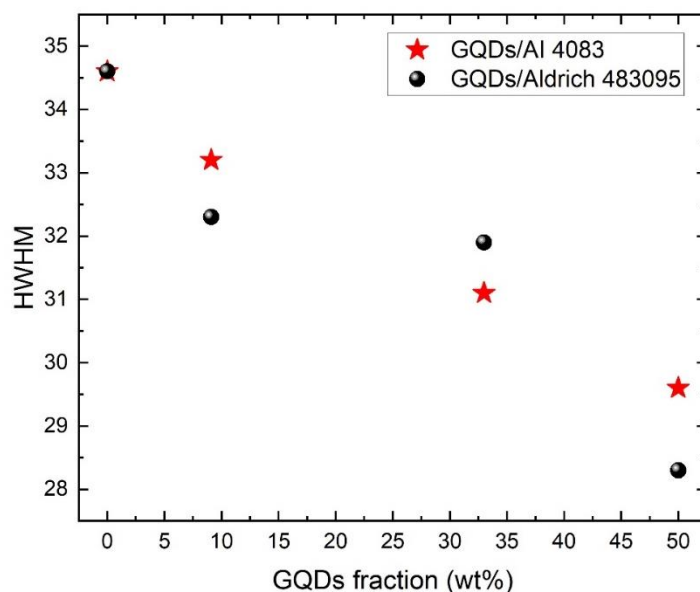


Figure 5.25 Main peak linewidth versus GQDs fraction.

To understand the thermal conductivity behaviour further, Raman spectroscopy was used to investigate structural variations. Figure 5.24 shows the Raman spectra of GQDs/PEDOT:PSS films. As GQDs fraction increases, the red shifts occur in the symmetric $C_{\alpha}=C_{\beta}$ stretching vibration, from 1432 cm^{-1} to 1417 cm^{-1} for GQDs/AI 4083 films and from 1424 cm^{-1} to 1410 cm^{-1} for GQDs/Aldrich 483095 films. As aforementioned, a red shift indicates an increased average conjugation length. This is possibly attributed to the dedoping of PEDOT chains from bipolaron to polaron or neutral state^{104,105}. This dedoping has been confirmed by the ellipsometry results in the section 5.6. PEDOT:PSS polymer chains tend to be more ordered with the increase of GQDs fraction.

Figure 5.25 illustrates the change in the main peak linewidth with GQDs fraction. There is a gradual decline in the linewidth of the most intense band, suggesting more homogeneous distribution of conjugated domains. However, we do not think the structural variations cause the drop of thermal conductivity, because the improved distribution homogeneity and more ordered polymer chains would increase thermal conductivity, not decrease it.

To check whether the aforementioned thermal conductivity results could be correlated to film morphological changes, we carried out an AFM characterization of GQDs/PEDOT:PSS composite films. The topography images of GQDs/AI 4083 films and GQDs/Aldrich 483095 films are shown in Figure 5.26 and Figure 5.27. We did not observe a clear morphology difference in GQDs/AI 4083 films with different GQDs fractions. Note that the thermal conductivity decreases significantly from the PEDOT:PSS film to the 1/10 hybrid film. However, the roughness and the phase separation of these

two films hardly change. Similar results are also obtained for GQDs/Aldrich 483095 films. In conclusion, the morphology cannot explain the observed drop in thermal conductivity.

In summary, we presume that the most possible mechanism which controls the thermal conductivity of GQDs/PEDOT:PSS films is that GQDs act as scattering centers. As the GQDs fraction increases, the phonon scattering becomes stronger, thus resulting in the decrease of thermal conductivity. However, a direct proof was not obtained, and further investigation is still needed.

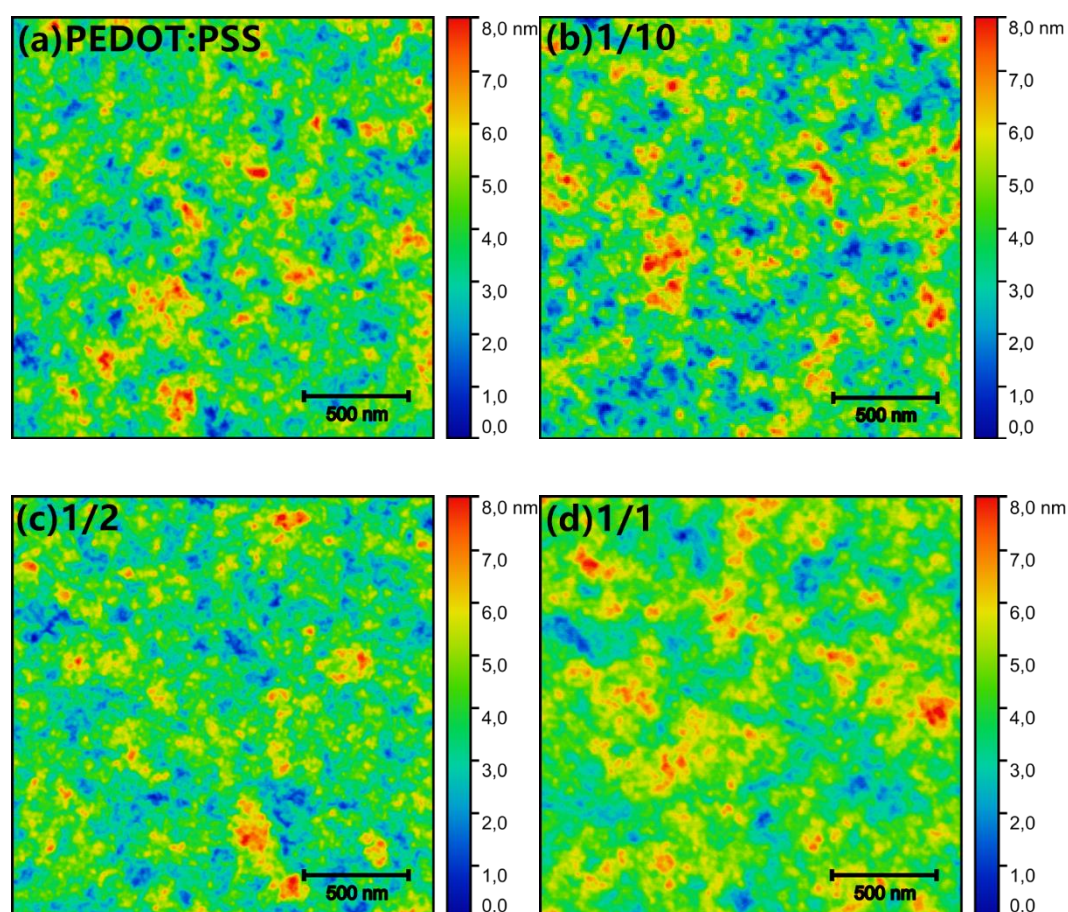


Figure 5.26 Topography images of GQDs/PEDOT:PSS (AI 4083) films. (a) PEDOT:PSS, $sq=1.1$ nm; (b) 1/10, $sq=1.3$ nm; (c) 1/2, $sq=1$ nm; (d) 1/1, $sq=1$ nm. All images depict an area of $2 \times 2 \mu\text{m}^2$. Scale bars represent 500 nm.

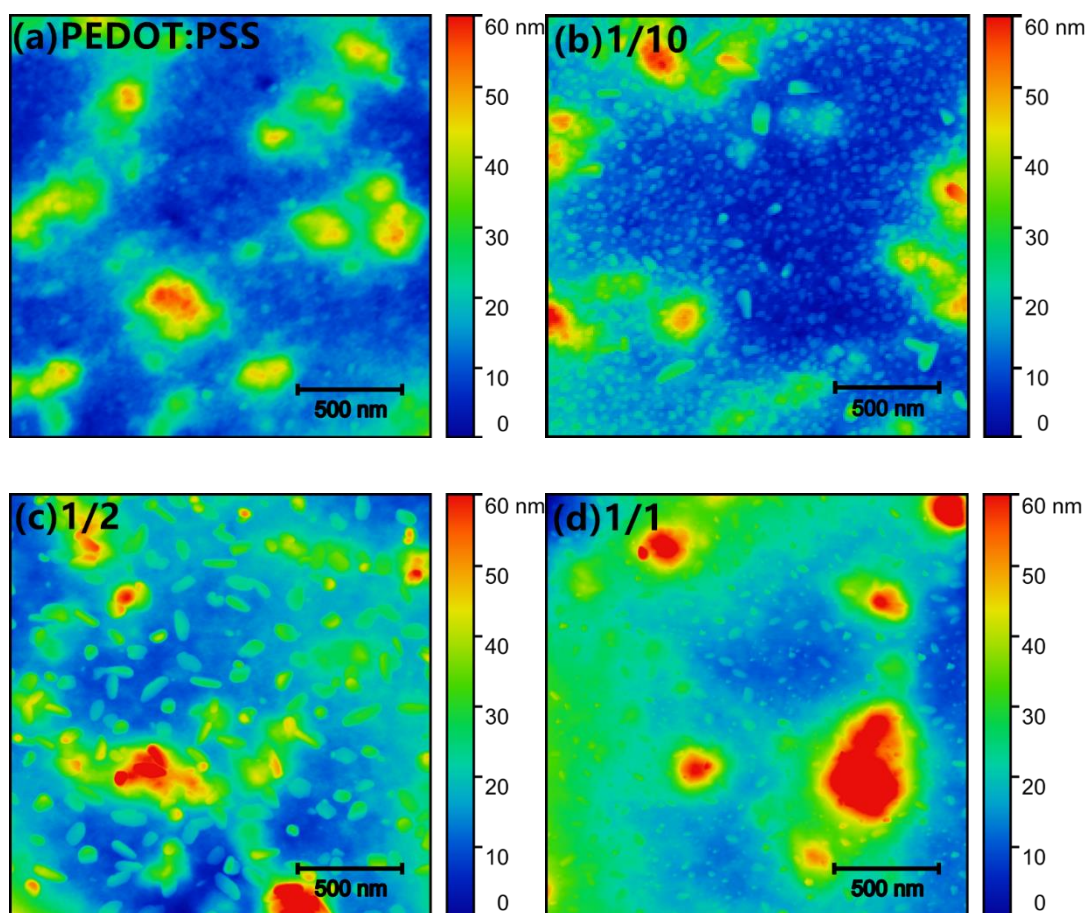


Figure 5.27 Topography images of GQDs/PEDOT:PSS (Aldrich 483095) films. (a) PEDOT:PSS, $sq=9.4$ nm; (b) 1/10, $sq=10$ nm; (c) 1/2, $sq=10$ nm; (d) 1/1, $sq=12.1$ nm. All images depict an area of $2 \times 2 \mu\text{m}^2$. Scale bars represent 500 nm.

5.8 Conclusions

We have demonstrated that it is possible to decrease the thermal conductivity of PEDOT:PSS (AI 4083) thin films by a factor of two by increasing the film thickness. The main mechanism that controls the thermal conductivity of PEDOT:PSS films is the distribution of conjugated lengths. In addition, the key advantages of this thickness gradient fabrication approach are: (i) the high throughput of experimental results it provides within one sample, and (ii) the obtained results provide an excellent relative determination of the influence of the thickness on investigated particular property, since a single fabrication step is used making each measurement consistently comparable and eliminating potential sample-to-sample variations.

The thermal conductivity of PEDOT:PSS films can also be significantly varied by doping with nanoparticles (ZnO NCs or GQDs), depending on the amount of nanoparticles. As far as ZnO/PEDOT:PSS hybrid films are concerned, a linear dependence of thermal conductivity with respect to ZnO fraction was observed, which originates from the composition change of hybrid films induced by varying ZnO fraction. It is worth mentioning here that the thermal conductivity of 1/100 ZnO/AI 4083 film depends not only on the film composition, but also on the improved distribution homogeneity of conjugated domains. For GQDs/PEDOT:PSS composite films, we have found a two-fold decrease for the thermal conductivity as GQDs fraction increases. The possible mechanism is that GQDs act as scattering centers and the phonon scattering plays a key role in the thermal conductivity change.

In this work we have also investigated the optical properties of PEDOT:PSS films blended with nanoparticles (ZnO NCs or GQDs) by spectroscopic ellipsometry. The decreasing bipolaron concentration and the appearance of polarons prove the dedoping of PEDOT chains in nanoparticle/PEDOT:PSS films as the nanoparticle fraction increases. In particular, the calculated GQDs fraction based on BEMA model is in good agreement with the set value in the fabrication process. As a remarkable finding, we observed that the optical anisotropy of PEDOT:PSS (Aldrich 483095) films is reduced after incorporating GQDs.

Moreover, we find that one should not only emphasize the frequency of the most intense band in the Raman spectra of PEDOT:PSS films. Instead we note that it is important to also pay close attention to the linewidth of the most intense band which contains important structure information.

In sum, the thermal conductivity of PEDOT:PSS films can be significantly tuned by changing the film thickness or by doping with nanoparticles. These results contribute to a deeper understanding of the thermal conductivity in PEDOT:PSS films, paving the way towards optimizing ZT value.

Conclusions & Outlook

We have systematically investigated the structural and optical properties of PEDOT:PSS thin films through spectroscopic ellipsometry and Raman scattering. From the ellipsometry studies we obtained the optical constants of the composite medium considering its optical anisotropy. In particular, the appearance of a weak polaron band indicated a change of the doping state within the PEDOT:PSS domains. On the other hand, the Raman spectra provided information about the conjugation length of the PEDOT component within the same domains. It is found that not only local structural changes of the chain conformation, but also the overall morphology of the composite films, are relevant for the interpretation of the Raman spectra. We have also observed that addition of DMSO tends to reduce the optical anisotropy of PEDOT:PSS films, which is in accordance with the morphology change induced by this additive. The observed segregation of PSS caused by DMSO leads to some dedoping and improved alignment of the fibrils in the PEDOT:PSS domains but it also tends to cause misaligned and smaller aggregated grains which results in the reduction of the optical anisotropy. On the other hand, it is possible that these smaller grains become closer in space, giving rise to improved electrical conductivity even if the correlation length in a grain may be reduced. This effect is largest in the lower PSS content formulation we have studied, while is relatively small in samples with higher PSS content. Here, we note that not only PSS contents and solvent treatment, but also deposition methods and specific deposition conditions can affect the final properties of PEDOT:PSS films.

We have also studied the thermal conductivity of the PEDOT:PSS films, and we show that it can be significantly tuned by changing the film thickness or by doping with nanoparticles (ZnO NCs or GQDs). It is observed that the thermal conductivity of PEDOT:PSS (AI 4083) films decreases by a factor of two by increasing the film thickness, which can be attributed to the change in the conjugated lengths distribution. As far as ZnO/PEDOT:PSS hybrid films are concerned, the thermal conductivity increases linearly with ZnO fraction, which originates from the composition change of hybrid films. The increased homogeneous distribution of conjugated domains accounts for the additional increment of thermal conductivity in the 1/100 ZnO/AI 4083 film. In the case of GQDs/PEDOT:PSS hybrid films, the thermal conductivity shows a two-fold decrease as GQDs fraction increases. These results are understood considering that the GQDs act as local scattering centers, hence, resulting in a decrease of the thermal conductivity. Furthermore, we have also investigated the optical properties of PEDOT:PSS films blended with nanoparticles (ZnO NCs or GQDs) by spectroscopic ellipsometry. Dedoping of the PEDOT chains is demonstrated by increasing the concentration of nanoparticles within the hybrid films. We also show that the optical anisotropy of the PEDOT:PSS (Aldrich 483095) films is reduced after incorporating GQDs.

Out of interest, further work can be carried out around suspended PEDOT:PSS thin films. We described the fabrication method of suspended PEDOT:X films in Chapter 2. However, suspended PEDOT:PSS films are more difficult to be prepared since it is challenging to find a suitable sacrificial layer which meets two requirements: (i) PEDOT:PSS aqueous solution shows good wettability on it; (ii) The solvent of this sacrificial solution does not dissolve PEDOT:PSS films. Once the suspended PEDOT:PSS thin films are prepared successfully, the following work will be to study their thermal anisotropy. We think that studying the possible correlation between the thermal and optical anisotropy can be of relevance for the field.

References

- (1) Burek, S. When Will Fossil Fuels Finally Run out and What Is the Technical Potential for Renewable Energy Resources? *Int. J. COMADEM* **2010**, *4* (13), 22–27.
- (2) *Waste Heat*. <https://www.waste-heat.eu/>.
- (3) Yang, L.; Chen, Z. G.; Dargusch, M. S.; Zou, J. High Performance Thermoelectric Materials: Progress and Their Applications. *Adv. Energy Mater.* **2018**, *8* (6), 1701797. <https://doi.org/10.1002/aenm.201701797>.
- (4) Snyder, G. J.; Toberer, E. S. Complex Thermoelectric Materials. *Mater. Sustain. Energy A Collect. Peer-Reviewed Res. Rev. Artic. from Nat. Publ. Gr.* **2011**, 101–110. https://doi.org/10.1142/9789814317665_0016.
- (5) Hamid Elsheikh, M.; Shnawah, D. A.; Sabri, M. F. M.; Said, S. B. M.; Haji Hassan, M.; Ali Bashir, M. B.; Mohamad, M. A Review on Thermoelectric Renewable Energy: Principle Parameters That Affect Their Performance. *Renew. Sustain. Energy Rev.* **2014**, *30*, 337–355. <https://doi.org/10.1016/j.rser.2013.10.027>.
- (6) Mardini-Bovea, J.; Torres-Díaz, G.; Sabau, M.; De-La-hoz-Franco, E.; Niño-Moreno, J.; Pacheco-Torres, P. J. A Review to Refrigeration with Thermoelectric Energy Based on the Peltier Effect. *DYNA* **2019**, *86* (208), 9–18. <https://doi.org/10.15446/DYNA.V86N208.72589>.
- (7) Vaqueiro, P.; Powell, A. V. Recent Developments in Nanostructured Materials for High-Performance Thermoelectrics. *J. Mater. Chem.* **2010**, *20* (43), 9577–9584. <https://doi.org/10.1039/c0jm01193b>.
- (8) Liu, W. Di; Chen, Z. G.; Zou, J. Eco-Friendly Higher Manganese Silicide Thermoelectric Materials: Progress and Future Challenges. *Adv. Energy Mater.* **2018**, *8* (19), 1–18. <https://doi.org/10.1002/aenm.201800056>.
- (9) Wang, Y.; Yang, L.; Shi, X.; Shi, X.; Chen, L.; Dargusch, M. S.; Zou, J.; Chen, Z. Flexible Thermoelectric Materials and Generators: Challenges and Innovations. *Adv. Mater.* **2019**, *31* (29), 1807916. <https://doi.org/10.1002/adma.201807916>.
- (10) Yang, J.; Caillat, T. Thermoelectric Materials for Space and Automotive Power Generation. *MRS Bull.* **2006**, *31* (3), 224–229. <https://doi.org/https://doi.org/10.1557/mrs2006.49>.
- (11) Chen, Z. G.; Hana, G.; Yanga, L.; Cheng, L.; Zou, J. Nanostructured Thermoelectric Materials: Current Research and Future Challenge. *Prog. Nat. Sci. Mater. Int.* **2012**, *22* (6), 535–549. <https://doi.org/10.1016/j.pnsc.2012.11.011>.
- (12) Kim, H. S.; Liu, W.; Chen, G.; Chu, C. W.; Ren, Z. Relationship between Thermoelectric Figure of Merit and Energy Conversion Efficiency. *Proc. Natl. Acad. Sci.* **2015**, *112* (27), 8205–8210. <https://doi.org/10.1073/pnas.1510231112>.

- (13) Zhang, X.; Zhao, L. D. Thermoelectric Materials: Energy Conversion between Heat and Electricity. *J. Mater.* **2015**, *1* (2), 92–105. <https://doi.org/10.1016/j.jmat.2015.01.001>.
- (14) Gayner, C.; Kar, K. K. Recent Advances in Thermoelectric Materials. *Prog. Mater. Sci.* **2016**, *83*, 330–382. <https://doi.org/10.1016/j.pmatsci.2016.07.002>.
- (15) Fleurial, J. P. Thermoelectric Power Generation Materials: Technology and Application Opportunities. *Jom* **2009**, *61* (4), 79–85. <https://doi.org/10.1007/s11837-009-0057-z>.
- (16) Gao, X.; Uehara, K.; Klug, D. D.; Tse, J. S. Rational Design of High-Efficiency Thermoelectric Materials with Low Band Gap Conductive Polymers. *Comput. Mater. Sci.* **2006**, *36* (1–2), 49–53. <https://doi.org/10.1016/j.commsci.2004.12.080>.
- (17) Zebarjadi, M.; Esfarjani, K.; Dresselhaus, M. S.; Ren, Z. F.; Chen, G. Perspectives on Thermoelectrics: From Fundamentals to Device Applications. *Energy Environ. Sci.* **2012**, *5* (1), 5147–5162. <https://doi.org/10.1039/c1ee02497c>.
- (18) Zheng, X. F.; Liu, C. X.; Yan, Y. Y.; Wang, Q. A Review of Thermoelectrics Research - Recent Developments and Potentials for Sustainable and Renewable Energy Applications. *Renew. Sustain. Energy Rev.* **2014**, *32*, 486–503. <https://doi.org/10.1016/j.rser.2013.12.053>.
- (19) Cutler, M.; Leavy, J. F.; Fitzpatrick, R. L. Electronic Transport in Semimetallic Cerium Sulfide. *Phys. Rev.* **1964**, *133* (4A). <https://doi.org/10.1103/PhysRev.133.A1143>.
- (20) Heremans, J. P.; Jovovic, V.; Toberer, E. S.; Saramat, A.; Kurosaki, K.; Charoenphakdee, A.; Yamanaka, S.; Snyder, G. J. Enhancement of Thermoelectric Efficiency in PbTe by Distortion of the Electronic Density of States. *Science*. **2008**, *321* (5888), 554–557. <https://doi.org/10.1126/science.1159725>.
- (21) Szczech, J. R.; Higgins, J. M.; Jin, S. Enhancement of the Thermoelectric Properties in Nanoscale and Nanostructured Materials. *J. Mater. Chem.* **2011**, *21* (12), 4037–4055. <https://doi.org/10.1039/c0jm02755c>.
- (22) *High Entropy Alloys: Innovations, Advances, and Applications*; Srivatsan, T. S., Gupta, M., Eds.; CRS Press, 2020.
- (23) Levi, A. F. J. The Drude Model. In *Essential Classical Mechanics for Device Physics*; Morgan & Claypool Publishers, 2016. <https://doi.org/10.1088/978-1-6817-4413-1ch6>.
- (24) Levinsky, P. Synthesis, Characterization and Optimization of New Thermoelectric Materials, Université de Lorraine; Czech Technical University in Prague, 2018.
- (25) Scheepers, M. Seebeck Coefficient and Electrical Conductivity Measurements on Poly (3 , 4-Ethylenedioxythiophene) Poly (Styrenesulfonate) Films Treated with

- Sulfuric Acid, Eindhoven University of Technology, 2013.
- (26) Huang, C.; Qian, X.; Yang, R. Thermal Conductivity of Polymers and Polymer Nanocomposites. *Mater. Sci. Eng. R Reports* **2018**, *132*, 1–22. <https://doi.org/10.1016/j.mser.2018.06.002>.
 - (27) Pereira Goncalves, A.; Branco Lopes, E.; Rouleau, O.; Godart, C. Conducting Glasses as New Potential Thermoelectric Materials: The Cu-Ge-Te Case. *J. Mater. Chem.* **2010**, *20* (8), 1516–1521. <https://doi.org/10.1039/b908579c>.
 - (28) Alam, H.; Ramakrishna, S. A Review on the Enhancement of Figure of Merit from Bulk to Nano-Thermoelectric Materials. *Nano Energy* **2013**, *2* (2), 190–212. <https://doi.org/10.1016/j.nanoen.2012.10.005>.
 - (29) Sootsman, J. R.; Chung, D. Y.; Kanatzidis, M. G. New and Old Concepts in Thermoelectric Materials. *Angew. Chemie - Int. Ed.* **2009**, *48* (46), 8616–8639. <https://doi.org/10.1002/anie.200900598>.
 - (30) *CRC Handbook of Thermoelectrics*; Rowe, D. M., Ed.; CRS Press, 1995.
 - (31) Nolas, G. S.; Goldsmid, H. J. The Figure of Merit in Amorphous Thermoelectrics. *Phys. Status Solidi* **2002**, *194* (1), 271–276. [https://doi.org/10.1002/1521-396X\(200211\)194:1<271::AID-PSSA271>3.0.CO;2-T](https://doi.org/10.1002/1521-396X(200211)194:1<271::AID-PSSA271>3.0.CO;2-T).
 - (32) Cahill, D. G.; Watson, S. K.; Pohl, R. O. Lower Limit to the Thermal Conductivity of Disordered Crystals. *Phys. Rev. B* **1992**, *46* (10), 6131–6140. <https://doi.org/10.1103/PhysRevB.46.6131>.
 - (33) Nolas, G. S.; Kaeser, M.; IV, R. T. L.; Tritt, T. M. High Figure of Merit in Partially Filled Ytterbium Skutterudite Materials. *Appl. Phys. Lett.* **2000**, *77* (12), 1855–1857. <https://doi.org/10.1063/1.1311597>.
 - (34) Snyder, G. J.; Christensen, M.; Nishibori, E.; Caillat, T.; Iversen, B. O. B. Disordered Zinc in Zn₄Sb₃ with Phonon-Glass and Electron-Crystal Thermoelectric Properties. *Nat. Mater.* **2004**, *3* (7), 458–463. <https://doi.org/10.1038/nmat1154>.
 - (35) Liu, W.; Zhang, B.; Li, J. Effects of Sb Compensation on Microstructure, Thermoelectric Properties and Point Defect of CoSb₃ Compound. *J. Phys. D. Appl. Phys.* **2007**, *40* (21), 6784–6790. <https://doi.org/10.1088/0022-3727/40/21/044>.
 - (36) Parker, D.; Singh, D. J. High-Temperature Thermoelectric Performance of Heavily Doped PbSe. *Phys. Rev. B* **2010**, *82* (3), 035204. <https://doi.org/10.1103/PhysRevB.82.035204>.
 - (37) Kim, G. H.; Shao, L.; Zhang, K.; Pipe, K. P. Engineered Doping of Organic Semiconductors for Enhanced Thermoelectric Efficiency. *Nat. Mater.* **2013**, *12* (8), 719–723. <https://doi.org/10.1038/nmat3635>.

- (38) Mao, J.; Liu, Z.; Ren, Z. Size Effect in Thermoelectric Materials. *npj Quantum Mater.* **2016**, *1* (1), 1–9. <https://doi.org/10.1038/npjquantmats.2016.28>.
- (39) Madavali, B.; Kim, H. S.; Lee, K. H.; Hong, S. J. Enhanced Seebeck Coefficient by Energy Filtering in Bi-Sb-Te Based Composites with Dispersed Y2O3 Nanoparticles. *Intermetallics* **2017**, *82*, 68–75. <https://doi.org/10.1016/j.intermet.2016.11.002>.
- (40) Lin, Y.; Dresselhaus, M. S. Thermoelectric Properties of Superlattice Nanowires. *Phys. Rev. B* **2003**, *68* (7), 075304. <https://doi.org/10.1103/PhysRevB.68.075304>.
- (41) Enisa, O.-M.; Badnjević, A.; Kazlagic, A.; Hajlovac, M. Nanocomposites: A Brief Review. *Health Technol. (Berl)*. **2020**, *10* (1), 51–59. <https://doi.org/10.1007/s12553-019-00380-x>.
- (42) Okpala, C. C. Nanocomposites – An Overview. *Int. J. Eng. Res. Dev.* **2013**, *8* (11), 17–23.
- (43) Novak, B. M. Hybrid Nanocomposite Materials-Between Inorganic Glasses and Organic Polymers. *Adv. Mater.* **1993**, *5* (6), 422–433. <https://doi.org/10.1002/adma.19930050603>.
- (44) Du, F. P.; Cao, N. N.; Zhang, Y. F.; Fu, P.; Wu, Y. G.; Lin, Z. D.; Shi, R.; Amini, A.; Cheng, C. PEDOT:PSS/Graphene Quantum Dots Films with Enhanced Thermoelectric Properties via Strong Interfacial Interaction and Phase Separation. *Sci. Rep.* **2018**, *8*(1), 1–12. <https://doi.org/10.1038/s41598-018-24632-4>.
- (45) Wang, Y.; Wu, S.; Zhang, R.; Du, K.; Yin, Q.; Jiang, B.; Yin, Q.; Zhang, K. Effects of Carbon Nanomaterials Hybridization of Poly(3,4- Ethylenedioxythiophene): Poly (Styrene Sulfonate) on Thermoelectric Performance. *Nanotechnology* **2021**, *32* (44), 445705. <https://doi.org/10.1088/1361-6528/ac17c3>.
- (46) Zhang, L.; Harima, Y.; Imae, I. Highly Improved Thermoelectric Performances of PEDOT:PSS/SWCNT Composites by Solvent Treatment. *Org. Electron.* **2017**, *51*, 304–307. <https://doi.org/10.1016/j.orgel.2017.09.030>.
- (47) Sun, K.; Zhang, S.; Li, P.; Xia, Y.; Zhang, X.; Du, D.; Isikgor, F. H.; Ouyang, J. Review on Application of PEDOTs and PEDOT:PSS in Energy Conversion and Storage Devices. *J. Mater. Sci. Mater. Electron.* **2015**, *26* (7), 4438–4462. <https://doi.org/10.1007/s10854-015-2895-5>.
- (48) Crispin, X.; Marciniak, S.; Osikowicz, W.; Zotti, G.; Gon, A. W. D. V. A. N. D. E. R.; Louwet, F.; Fahlman, M.; Groenendaal, L.; Schryver, F. D. E.; Salaneck, W. R. Conductivity, Morphology, Interfacial Chemistry, and Stability of Poly(3,4-Ethylene Dioxythiophene)– Poly(Styrene Sulfonate): A Photoelectron Spectroscopy Study. *J. Polym. Sci. Part B Polym. Phys.* **2003**, *41* (21), 2561–2583. <https://doi.org/10.1002/polb.10659>.

- (49) Wang, H.; Ail, U.; Gabrielsson, R.; Berggren, M.; Crispin, X. Ionic Seebeck Effect in Conducting Polymers. *Adv. Energy Mater.* **2015**, *5* (11), 1500044. <https://doi.org/10.1002/aenm.201500044>.
- (50) Zotti, G.; Zecchin, S.; Schiavon, G.; Louwet, F.; Groenendaal, L.; Crispin, X.; Osikowicz, W.; Salaneck, W.; Fahlman, M. Electrochemical and XPS Studies toward the Role of Monomeric and Polymeric Sulfonate Counterions in the Synthesis, Composition, and Properties of Poly(3,4-Ethylenedioxythiophene). *Macromolecules* **2003**, *36* (9), 3337–3344. <https://doi.org/10.1021/ma021715k>.
- (51) Ouyang, L.; Musumeci, C.; Jafari, M. J.; Ederth, T.; Inganäs, O. Imaging the Phase Separation between PEDOT and Polyelectrolytes during Processing of Highly Conductive PEDOT:PSS Films. *ACS Appl. Mater. Interfaces* **2015**, *7* (35), 19764–19773. <https://doi.org/10.1021/acsami.5b05439>.
- (52) Kirchmeyer, S.; Reuter, K. Scientific Importance, Properties and Growing Applications of Poly(3,4-Ethylenedioxythiophene). *J. Mater. Chem.* **2005**, *15* (21), 2077–2088. <https://doi.org/10.1039/b417803n>.
- (53) Andrei, V.; Bethke, K.; Madzharova, F.; Beeg, S.; Knop-Gericke, A.; Kneipp, J.; Rademann, K. Size Dependence of Electrical Conductivity and Thermoelectric Enhancements in Spin-Coated PEDOT:PSS Single and Multiple Layers. *Adv. Electron. Mater.* **2017**, *3* (2), 1600473. <https://doi.org/10.1002/aelm.201600473>.
- (54) Palumbiny, C. M.; Heller, C.; Schaffer, C. J.; Körstgens, V.; Santoro, G.; Roth, S. V.; Müller-Buschbaum, P. Molecular Reorientation and Structural Changes in Cosolvent-Treated Highly Conductive PEDOT:PSS Electrodes for Flexible Indium Tin Oxide-Free Organic Electronics. *J. Phys. Chem. C* **2014**, *118* (25), 13598–13606. <https://doi.org/10.1021/jp501540y>.
- (55) Timpanaro, S.; Kemerink, M.; Touwslager, F. J.; De Kok, M. M.; Schrader, S. Morphology and Conductivity of PEDOT/PSS Films Studied by Scanning-Tunneling Microscopy. *Chem. Phys. Lett.* **2004**, *394* (4–6), 339–343. <https://doi.org/10.1016/j.cplett.2004.07.035>.
- (56) Nardes, A. M.; Kemerink, M.; Janssen, R. A. J.; Bastiaansen, J. A. M.; Kiggen, N. M. M.; Langeveld, B. M. W.; Van Breemen, A. J. J. M.; De Kok, M. M. Microscopic Understanding of the Anisotropic Conductivity of PEDOT:PSS Thin Films. *Adv. Mater.* **2007**, *19* (9), 1196–1200. <https://doi.org/10.1002/adma.200602575>.
- (57) Thomas, J. P.; Zhao, L.; McGillivray, D.; Leung, K. T. High-Efficiency Hybrid Solar Cells by Nanostructural Modification in PEDOT:PSS with Co-Solvent Addition. *J. Mater. Chem. A* **2014**, *2* (7), 2383–2389. <https://doi.org/10.1039/c3ta14590e>.
- (58) Takano, T.; Masunaga, H.; Fujiwara, A.; Okuzaki, H.; Sasaki, T. PEDOT Nanocrystal in Highly Conductive PEDOT:PSS Polymer Films. *Macromolecules* **2012**, *45* (9), 3859–3865. <https://doi.org/10.1021/ma300120g>.
- (59) Brédas, J. L.; Wudl, F.; Heeger, A. J. Polarons and Bipolarons in Doped

- Polythiophene: A Theoretical Investigation. *Solid State Commun.* **1987**, *63* (7), 577–580. [https://doi.org/10.1016/0038-1098\(87\)90856-8](https://doi.org/10.1016/0038-1098(87)90856-8).
- (60) Zozoulenko, I.; Singh, A.; Singh, S. K.; Gueskine, V.; Crispin, X.; Berggren, M. Polarons, Bipolarons, and Absorption Spectroscopy of PEDOT. *ACS Appl. Polym. Mater.* **2019**, *1* (1), 83–94. <https://doi.org/10.1021/acsapm.8b00061>.
- (61) Gangopadhyay, R.; Das, B.; Molla, M. R. How Does PEDOT Combine with PSS? Insights from Structural Studies. *RSC Adv.* **2014**, *4* (83), 43912–43920. <https://doi.org/10.1039/c4ra08666j>.
- (62) Sun, Y.; Li, H.; Hou, R.; Diao, M.; Liang, Y.; Huang, Z.; Humphrey, M. G.; Zhang, C. Realizing Saturable Absorption and Reverse Saturable Absorption in a PEDOT:PSS Film via Electrical Modulation. *ACS Appl. Mater. Interfaces* **2020**, *12* (43), 48982–48990. <https://doi.org/10.1021/acsami.0c14447>.
- (63) Aidun, C. K.; Triantafillopoulos, N. G. High-Speed Blade Coating. In *Liquid Film Coating*; Springer: Dordrecht, 1997; pp 637–672. https://doi.org/10.1007/978-94-011-5342-3_18.
- (64) Li, Y.; Meng, G. W.; Zhang, L. D.; Phillipp, F. Ordered Semiconductor ZnO Nanowire Arrays and Their Photoluminescence Properties. *Appl. Phys. Lett.* **2000**, *76* (15), 2011–2013. <https://doi.org/10.1063/1.126238>.
- (65) Könenkamp, R.; Boedecker, K.; Lux-Steiner, M. C.; Poschenrieder, M.; Zenia, F.; Levy-Clement, C.; Wagner, S. Thin Film Semiconductor Deposition on Free-Standing ZnO Columns. *Appl. Phys. Lett.* **2000**, *77* (16), 2575–2577. <https://doi.org/10.1063/1.1319187>.
- (66) Kong, Y. C.; Yu, D. P.; Zhang, B.; Fang, W.; Feng, S. Q. Ultraviolet-Emitting ZnO Nanowires Synthesized by a Physical Vapor Deposition Approach. *Appl. Phys. Lett.* **2001**, *78* (4), 407–409. <https://doi.org/10.1063/1.1342050>.
- (67) Pacholski, C.; Kornowski, A.; Weller, H. Self-Assembly of ZnO: From Nanodots to Nanorods. *Angew. Chem. Int. Ed.* **2002**, *41* (7), 1188–1191. [https://doi.org/10.1002/1521-3773\(20020402\)41:7<1188::AID-ANIE1188>3.0.CO;2-5](https://doi.org/10.1002/1521-3773(20020402)41:7<1188::AID-ANIE1188>3.0.CO;2-5).
- (68) Greene, L. E.; Law, M.; Goldberger, J.; Kim, F.; Johnson, J. C.; Zhang, Y.; Saykally, R. J.; Yang, P. Low-Temperature Wafer-Scale Production of ZnO Nanowire Arrays. *Angew. Chemie - Int. Ed.* **2003**, *42* (26), 3031–3034. <https://doi.org/10.1002/anie.200351461>.
- (69) Jiang, F.; Xiong, J.; Zhou, W.; Liu, C.; Wang, L.; Zhao, F.; Liu, H.; Xu, J. Use of Organic Solvent-Assisted Exfoliated MoS₂ for Optimizing the Thermoelectric Performance of Flexible PEDOT:PSS Thin Films. *J. Mater. Chem. A* **2016**, *4* (14), 5265–5273. <https://doi.org/10.1039/c6ta00305b>.
- (70) Tompkins Harland G.; Hilfiker James N. *Spectroscopic Ellipsometry: Practical*

Application to Thin Film Characterization; Momentum Press: New York, 2016.

- (71) Humlíček, J.; Nebojsa, A.; Hora, J.; Stráský, M.; Spousta, J.; Šikola, T. Ellipsometry and Transport Studies of Thin-Film Metal Nitrides. *Thin Solid Films* **1998**, *332* (1–2), 25–29. [https://doi.org/10.1016/S0040-6090\(98\)01014-1](https://doi.org/10.1016/S0040-6090(98)01014-1).
- (72) Chen, S.; Kühne, P.; Stanishev, V.; Knight, S.; Brooke, R.; Petsagkourakis, I.; Crispin, X.; Schubert, M.; Darakchieva, V.; Jonsson, M. P. On the Anomalous Optical Conductivity Dispersion of Electrically Conducting Polymers: Ultra-Wide Spectral Range Ellipsometry Combined with a Drude-Lorentz Model. *J. Mater. Chem. C* **2019**, *7* (15), 4350–4362. <https://doi.org/10.1039/c8tc06302h>.
- (73) Laskarakis, A.; Karagkiozaki, V.; Georgiou, D.; Gravalidis, C.; Logothetidis, S. Insights on the Optical Properties of Poly(3,4-Ethylenedioxythiophene): Poly(Styrenesulfonate) Formulations by Optical Metrology. *Materials (Basel)*. **2017**, *10* (8), 959. <https://doi.org/10.3390/ma10080959>.
- (74) Liu, Q.; Imamura, T.; Hiata, T.; Khatri, I.; Tang, Z.; Ishikawa, R.; Ueno, K.; Shirai, H. Optical Anisotropy in Solvent-Modified Poly(3,4-Ethylenedioxythiophene): Poly(Styrenesulfonic Acid) and Its Effect on the Photovoltaic Performance of Crystalline Silicon/Organic Heterojunction Solar Cells. *Appl. Phys. Lett.* **2013**, *102* (24), 243902. <https://doi.org/10.1063/1.4811355>.
- (75) Ino, T.; Hayashi, T.; Fukuda, T.; Ueno, K.; Shirai, H. Depth Profile Characterization of Spin-Coated Poly(3,4-Ethylenedioxythiophene): Poly(Styrene Sulfonic Acid) (PEDOT:PSS) Films by Spectroscopic Ellipsometry. *Phys. Status Solidi C* **2011**, *8* (10), 3025–3028. <https://doi.org/10.1002/pssc.201001218>.
- (76) Millán, C.; Santonja, C.; Domingo, M.; Luna, R.; Satorre, M. Á. An Experimental Test for Effective Medium Approximations (EMAs). *Astron. Astrophys.* **2019**, *628*, A63. <https://doi.org/10.1051/0004-6361/201935153>.
- (77) Garreau, S.; Louarn, G.; Buisson, J. P.; Froyer, G.; Lefrant, S. In Situ Spectroelectrochemical Raman Studies of Poly(3,4-Ethylenedioxythiophene) (PEDT). *Macromolecules* **1999**, *32* (20), 6807–6812. <https://doi.org/10.1021/ma9905674>.
- (78) Chiu, W. W.; Travaš-Sejdić, J.; Cooney, R. P.; Bowmaker, G. A. Studies of Dopant Effects in Poly(3,4-Ethylenedioxythiophene) Using Raman Spectroscopy. *J. Raman Spectrosc.* **2006**, *37* (12), 1354–1361. <https://doi.org/10.1002/jrs.1545>.
- (79) Schmidt, A. J.; Cheaito, R.; Chiesa, M. A Frequency-Domain Thermoreflectance Method for the Characterization of Thermal Properties. *Rev. Sci. Instrum.* **2009**, *80* (9), 094901. <https://doi.org/10.1063/1.3212673>.
- (80) Regner, K. T.; Majumdar, S.; Malen, J. A. Instrumentation of Broadband Frequency Domain Thermoreflectance for Measuring Thermal Conductivity Accumulation Functions. *Rev. Sci. Instrum.* **2013**, *84* (6), 064901. <https://doi.org/10.1063/1.4808055>.

- (81) Regner, K. T.; Sellan, D. P.; Su, Z.; Amon, C. H.; McGaughey, A. J. H.; Malen, J. A. Broadband Phonon Mean Free Path Contributions to Thermal Conductivity Measured Using Frequency Domain Thermoreflectance. *Nat. Commun.* **2013**, *4* (1), 1–7. <https://doi.org/10.1038/ncomms2630>.
- (82) Liu, J.; Wang, X.; Li, D.; Coates, N. E.; Segalman, R. A.; Cahill, D. G. Thermal Conductivity and Elastic Constants of PEDOT:PSS with High Electrical Conductivity. *Macromolecules* **2015**, *48* (3), 585–591. <https://doi.org/10.1021/ma502099t>.
- (83) van der Pauw, L. J. A Method of Measuring Specific Resistivity and Hall Effect of Discs of Arbitrary Shape. *Philips Res. Reports* **1958**, *13* (1), 1–9.
- (84) Andreas, E.; Stephan, K.; Wilfried, L.; Udo, M.; Knud, R. *PEDOT: Principles and Applications of an Intrinsically Conductive Polymer*, CRC Press, 2010.
- (85) Kim, N.; Petsagkourakis, I.; Chen, S.; Berggren, M.; Crispin, X.; Jonsson, M. P.; Zozoulenko, I. Electric Transport Properties in PEDOT Thin Films. In *Conjugated Polymers*; CRC Press, 2019; pp 45–128.
- (86) Pettersson, L. A. A.; Ghosh, S.; Inganäs, O. Optical Anisotropy in Thin Films of Poly(3,4-Ethylenedioxythiophene)–Poly(4-Styrenesulfonate). *Org. Electron.* **2002**, *3* (3–4), 143–148. [https://doi.org/10.1016/S1566-1199\(02\)00051-4](https://doi.org/10.1016/S1566-1199(02)00051-4).
- (87) Syrový, T.; Janicek, P.; Mistrik, J.; Palka, K.; Hawlova, P.; Kubac, L.; Gunde, M. K. Optical, Electrical and Morphological Study of PEDOT: PSS Single Layers Spiral-Bar Coated with Various Secondary Doping Solvents. *Synth. Met.* **2017**, *227*, 139–147. <https://doi.org/10.1016/j.synthmet.2017.04.006>.
- (88) Pettersson, L. A. A.; Roman, L. S.; Inganäs, O. Modeling Photocurrent Action Spectra of Photovoltaic Devices Based on Organic Thin Films. *J. Appl. Phys.* **1999**, *86* (1), 487. <https://doi.org/10.1063/1.370757>.
- (89) Isoniemi, T.; Tuukkanen, S.; Cameron, D. C.; Simonen, J.; Toppari, J. J. Measuring Optical Anisotropy in Poly(3,4-Ethylene Dioxythiophene):Poly(Styrene Sulfonate) Films with Added Graphene. *Org. Electron.* **2015**, *25*, 317–323. <https://doi.org/10.1016/j.orgel.2015.06.037>.
- (90) Mauger, S. A.; Moulé, A. J. Characterization of New Transparent Organic Electrode Materials. *Org. Electron.* **2011**, *12* (11), 1948–1956. <https://doi.org/10.1016/j.orgel.2011.08.008>.
- (91) *Spectroscopic Ellipsometry for Photovoltaics*; Fujiwara, H., Collins, R. W., Eds.; Springer: Switzerland, 2018; Vol. 1. <https://doi.org/10.1007/978-3-319-75377-5>.
- (92) Kim, E. G.; Brédas, J. L. Electronic Evolution of Poly(3,4-Ethylenedioxythiophene) (PEDOT): From the Isolated Chain to the Pristine and Heavily Doped Crystals. *J. Am. Chem. Soc.* **2008**, *130* (50), 16880–16889. <https://doi.org/10.1021/ja806389b>.

- (93) Campoy-Quiles, M.; Alonso, M. I.; Bradley, D. D. C.; Richter, L. J. Advanced Ellipsometric Characterization of Conjugated Polymer Films. *Adv. Funct. Mater.* **2014**, *24* (15), 2116–2134. <https://doi.org/10.1002/adfm.201303060>.
- (94) Stavytska-barba, M.; Kelley, A. M. Surface Enhanced Raman Study of the Interaction of PEDOT : PSS with Silver and Gold Nanoparticles. In *Conference on Lasers and Electro-Optics*; 2010. <https://doi.org/10.1364/QELS.2010.JThE15>.
- (95) Dkhissi, A.; Louwet, F.; Groenendaal, L.; Beljonne, D.; Lazzaroni, R.; Brédas, J. L. Theoretical Investigation of the Nature of the Ground State in the Low-Bandgap Conjugated Polymer, Poly(3,4-Ethylenedioxythiophene). *Chem. Phys. Lett.* **2002**, *359*(5–6), 466–472. [https://doi.org/10.1016/S0009-2614\(02\)00651-6](https://doi.org/10.1016/S0009-2614(02)00651-6).
- (96) Lenz, A.; Kariis, H.; Pohl, A.; Persson, P.; Ojamäe, L. The Electronic Structure and Reflectivity of PEDOT:PSS from Density Functional Theory. *Chem. Phys.* **2011**, *384* (1–3), 44–51. <https://doi.org/10.1016/J.CHEMPHYS.2011.05.003>.
- (97) Garreau, S.; Leclerc, M.; Errien, N.; Louarn, G. Planar-to-Nonplanar Conformational Transition in Thermochromic Polythiophenes: A Spectroscopic Study. *Macromolecules* **2003**, *36* (3), 692–697. <https://doi.org/10.1021/MA021358D>.
- (98) Gasiorowski, J.; Menon, R.; Hingerl, K.; Dachev, M.; Sariciftci, N. S. Surface Morphology, Optical Properties and Conductivity Changes of Poly(3,4-Ethylenedioxythiophene):Poly(Styrenesulfonate) by Using Additives. *Thin Solid Films* **2013**, *536*, 211–215. <https://doi.org/10.1016/J.TSF.2013.03.124>.
- (99) Heroux, L.; Moncada, J.; Dadmun, M. Controlling the Morphology of PEDOT:PSS Blend Films with Pre-Deposition Solution Composition and Deposition Technique. *ACS Appl. Polym. Mater.* **2021**, *4* (1), 36–43. <https://doi.org/10.1021/ACSAPM.1C00748>.
- (100) Coates, N. E.; Yee, S. K.; McCulloch, B.; See, K. C.; Majumdar, A.; Segalman, R. A.; Urban, J. J. Effect of Interfacial Properties on Polymer-Nanocrystal Thermoelectric Transport. *Adv. Mater.* **2013**, *25* (11), 1629–1633. <https://doi.org/10.1002/adma.201203915>.
- (101) Lin, Y.-J.; Tsai, C.-L.; Su, Y.-C.; Liu, D.-S. Carrier Transport Mechanism of Poly (3,4-Ethylenedioxythiophene) Doped with Poly (4-Styrenesulfonate) Films by Incorporating ZnO Nanoparticles. *Appl. Phys. Lett.* **2012**, *100* (25), 253302. <https://doi.org/10.1063/1.4730391>.
- (102) Bacon, M.; Bradley, S. J.; Nann, T. Graphene Quantum Dots. *Part. Part. Syst. Charact.* **2014**, *31* (4), 415–428. <https://doi.org/10.1002/ppsc.201300252>.
- (103) Kim, S. H. Control of the Charge Carrier Concentration and Hall Mobility in PEDOT:PSS Thermoelectric Films. *Bull. Korean Chem. Soc.* **2017**, *38* (12), 1460–1464. <https://doi.org/10.1002/bkcs.11327>.

- (104) Zhu, Z.; Liu, C.; Jiang, Q.; Shi, H.; Jiang, F.; Xu, J.; Xiong, J.; Liu, E. Optimizing the Thermoelectric Properties of PEDOT:PSS Films by Combining Organic Co-Solvents with Inorganic Base. *J. Mater. Sci. Mater. Electron.* **2015**, *26* (11), 8515–8521. <https://doi.org/10.1007/s10854-015-3523-0>.
- (105) Lee, S. H.; Park, H.; Kim, S.; Son, W.; Cheong, I. W.; Kim, J. H. Transparent and Flexible Organic Semiconductor Nanofilms with Enhanced Thermoelectric Efficiency. *J. Mater. Chem. A* **2014**, *2* (20), 7288–7294. <https://doi.org/10.1039/c4ta00700j>.
- (106) Semaltianos, N. G.; Logothetidis, S.; Hastas, N.; Perrie, W.; Romani, S.; Potter, R. J.; Dearden, G.; Watkins, K. G.; French, P.; Sharp, M. Modification of the Electrical Properties of PEDOT:PSS by the Incorporation of ZnO Nanoparticles Synthesized by Laser Ablation. *Chem. Phys. Lett.* **2010**, *484* (4–6), 283–289. <https://doi.org/10.1016/j.cplett.2009.11.054>.
- (107) Brus, L. E. Electron-Electron and Electron-Hole Interactions in Small Semiconductor Crystallites: The Size Dependence of the Lowest Excited Electronic State. *J. Chem. Phys.* **1984**, *80* (9), 4403–4409. <https://doi.org/10.1063/1.447218>.
- (108) Silambarasan, M.; Saravanan, S.; Soga, T. Raman and Photoluminescence Studies of Ag and Fe-Doped ZnO Nanoparticles. *Int. J. ChemTech Res.* **2015**, *7* (3), 1644–1650.
- (109) Yazawa, K.; Kendig, D.; Raad, P. E.; Komarov, P. L.; Shakouri, A. *Understanding the Thermoreflectance Coefficient for High Resolution Thermal Imaging of Microelectronic Devices*. <https://www.electronics-cooling.com/2013/03/understanding-the-thermoreflectance-coefficient-for-high-resolution-thermal-imaging-of-microelectronic-devices/>.

List of Abbreviations

PEDOT:PSS	poly(3,4-ethylenedioxythiophene) polystyrene sulfonate
TE	thermoelectric
GQDs	graphene quantum dots
TEGs	thermoelectric generators
STEGs	solar thermoelectric generators
RTGs	radioisotope thermoelectric generators
ZT	figure of merit
PF	power factor
DOS	density of states
PGEC	phonon-glass electron-crystal
IPA	isopropanol
ZnO NCs	ZnO nanocrystals
ZnO NWs	ZnO nanowires
PSSNa	poly(sodium-4-styrenesulfonate)
AFM	atomic force microscopy
SEM	scanning electron microscope
SE	spectroscopic ellipsometry
KK relation	Kramers-Kronig relation
EMA	effective medium approximation
BEMA	Bruggemann effective medium approximation
FDTR	frequency-domain thermoreflectance
CPs	critical points
BC	blade coating
DC	drop casting
MSE	mean squared error
ZnO/PEDOT:PSS	ZnO nanocrystals/PEDOT:PSS

List of Figures

Figure 1.1 TE parameters as a function of carrier concentration.....	2
Figure 1.2 Power generation efficiency as functions of temperature of the hot end and ZT_{ave}	4
Figure 1.3 Schematic of the Seebeck effect.	5
Figure 1.4 Schematic diagram of Drude model.	6
Figure 1.5 Heat flow in a uniform cylinder along its length direction.	8
Figure 1.6 Chemical structure of PEDOT:PSS with a doping level of about 0.33.....	11
Figure 1.7 Chemical structure of neutral and doped PEDOT units.	13
Figure 2.1 Schematic illustration of the drop casting process.	15
Figure 2.2 Photograph of a drop-cast PEDOT:PSS (AI 4083) film on a glass substrate.....	17
Figure 2.3 Schematic diagram of static dispense spin coating process.....	18
Figure 2.4 Complete fabrication process of PEDOT:PSS thin films.	18
Figure 2.5 Photograph of a blade-coated PEDOT:PSS (Aldrich 483095) thin film on a glass slide.	18
Figure 2.6 Sketch of blade coating process using a blade that is moving relatively to the stationary substrate.....	20
Figure 2.7 Schematic representation of a blade-coated PEDOT:PSS film with a thickness gradient along the length of a glass slide.	20
Figure 2.8 Thickness gradients of PEDOT:PSS films parallel to the long axis of glass slides.	21
Figure 2.9 Experimental set-up used for synthesizing ZnO nanocrystals.....	22
Figure 2.10 Schematic diagram of synthesizing oriented ZnO nanowires by hydrothermal method.	23
Figure 2.11 Schematic illustration of vacuum filtration apparatus.	23
Figure 2.12 Relative position of layers during the film transferring from the filter paper to the glass.	24
Figure 2.13 Photograph of DMSO-induced phase separated PEDOT:PSS films after complete drying.	26
Figure 2.14 Schematic shows 2-layer stack to get a suspended PEDOT thin film.	26
Figure 2.15 Suspended PEDOT thin film on a gasket.....	27
Figure 2.16 Optical micrograph of the surface of the suspended PEDOT thin film.....	27
Figure 3.1 Schematic displaying the basic principle of AFM.....	29
Figure 3.2 Topography image of a blade-coated PEDOT:PSS (AI 4083) thin film with a thickness of 55 nm.	30
Figure 3.3 Surface profile of a PEDOT:PSS (AI 4083) thin film with the thickness of 215nm.	31
Figure 3.4 A typical ellipsometry experimental setup.	32
Figure 3.5 Schematic diagram of ellipsometry measurement.	33
Figure 3.6 Raman spectrum of a blade-coated PEDOT:PSS (AI 4083) thin film with a	

thickness of 89 nm.	38
Figure 3.7 Optical principle of frequency-domain thermoreflectance.	40
Figure 3.8 A PEDOT:PSS film with a 60 nm gold layer for FDTR measurement.	41
Figure 3.9 Change in the phase lag of a 100 nm blade-coated PEDOT:PSS film with the frequency.	41
Figure 3.10 Schematic of a square film for the Van der Pauw measurement.	42
Figure 3.11 A custom setup for the measurement of sheet resistance, in the case of thin films.	43
Figure 3.12 PEDOT:PSS thin film for electrical conductivity measurement.	43
Figure 4.1 (a) Complex refractive index components for different films of PEDOT:PSS (Aldrich 483095). (b) Experimental spectra at five angles of incidence and their best fits using both isotropic and anisotropic models for the thinner ($d=930$ nm) drop-cast film.	48
Figure 4.2 Ellipsometric spectra at two angles of incidence for the thin blade-coated film of PEDOT:PSS (Aldrich 483095) and regression fits.	49
Figure 4.3 Raman spectrum of a drop-cast PEDOT:PSS (Aldrich 483095) film.	51
Figure 4.4 Graphical representation of the main modes of PEDOT according to Ref. ⁷⁷	53
Figure 4.5 Complex refractive index components for different films of PEDOT:PSS (AI 4083).	55
Figure 4.6 Optical functions of PEDOT:PSS modified with DMSO.	56
Figure 4.7 Main Raman band for the drop-cast PEDOT:PSS films before and after DMSO treatment.	57
Figure 5.1 Out-of-plane thermal conductivity of blade-coated PEDOT:PSS films measured by FDTR as a function of the film thickness.	61
Figure 5.2 Electrical conductivity of PEDOT:PSS (Aldrich 483095) films versus thickness.	62
Figure 5.3 Main peak position versus thickness in the Raman spectra of PEDOT:PSS films.	63
Figure 5.4 Topography images of PEDOT:PSS (AI 4083) films with different thicknesses.	64
Figure 5.5 Topography images of PEDOT:PSS (Aldrich 483095) films with different thicknesses.	65
Figure 5.6 Optical absorption coefficient spectrum of ZnO nanocrystals detected from 1/13 ZnO NCs/PEDOT:PSS hybrid film by ellipsometry.	66
Figure 5.7 SEM images of ZnO nanowire arrays synthesized by hydrothermal method.	67
Figure 5.8 Raman spectrum of ZnO nanowires.	68
Figure 5.9 Drude parameters and conductivity of ZnO/PEDOT:PSS (AI 4083) films versus ZnO fraction.	70
Figure 5.10 Absorption coefficient spectra of PEDOT:PSS (AI 4083) film (black) and 1/100 ZnO/PEDOT:PSS hybrid film (red).	71
Figure 5.11 Drude parameters of the in-plane optical response and corresponding	

conductivity of ZnO/PEDOT:PSS (Aldrich 483095) films versus ZnO fraction.	72
Figure 5.12 Amplitude of the generalized Lorentzian versus ZnO fraction in the ellipsometry fitting of ZnO/PEDOT:PSS (Aldrich 483095) films.....	72
Figure 5.13 Thermal conductivity of blade-coated ZnO/PEDOT:PSS hybrid thin films measured by FDTR as a function of ZnO fraction.	73
Figure 5.14 Electrical conductivity of ZnO/PEDOT:PSS films versus ZnO fraction.....	74
Figure 5.15 Raman spectra of ZnO/PEDOT:PSS films.....	75
Figure 5.16 Main peak linewidth versus ZnO fraction.	76
Figure 5.17 Topography images of ZnO/PEDOT:PSS (AI 4083) films.....	78
Figure 5.18 Topography images of ZnO/PEDOT:PSS (Aldrich 483095) films.....	79
Figure 5.19 Complex refractive index of GQDs/PEDOT:PSS (AI 4083) films.....	81
Figure 5.20 Complex refractive index of GQDs/PEDOT:PSS (Aldrich 483095) films.....	82
Figure 5.21 Drude parameters and conductivity of GQDs/PEDOT:PSS (AI 4083) films versus GQDs fraction.....	83
Figure 5.22 Thermal conductivity of blade-coated GQDs/PEDOT:PSS hybrid thin films measured by FDTR as a function of GQDs fraction.	85
Figure 5.23 Electrical conductivity of GQDs/PEDOT:PSS films versus GQDs fraction.	86
Figure 5.24 Raman spectra of GQDs/PEDOT:PSS films.....	87
Figure 5.25 Main peak linewidth versus GQDs fraction.	88
Figure 5.26 Topography images of GQDs/PEDOT:PSS (AI 4083) films.....	89
Figure 5.27 Topography images of GQDs/PEDOT:PSS (Aldrich 483095) films.....	90

List of Tables

Table 2.1 Reagents and equipment in Chapter 2	16
Table 2.2 Blade-coating parameters of ZnO NCs/PEDOT:PSS and GQDs/PEDOT:PSS hybrid films	25
Table 3.1 Summary of vibrational modes in the Raman spectrum of a PEDOT:PSS film (89 nm) at 785 nm excitation wavelength according to Ref. ^{77,78}	38
Table 3.2 Parameters in FDTR fitting process.....	41
Table 4.1 Parameters determined from ellipsometry and Raman spectra for selected samples studied in this work.....	50
Table 5.1 Thicknesses of ZnO/PEDOT:PSS (AI 4083) films	69
Table 5.2 Thicknesses of ZnO/PEDOT:PSS (Aldrich 483095) films	69
Table 5.3 Ellipsometry results of GQDs/PEDOT:PSS (AI 4083) films based on BEMA model.....	80
Table 5.4 Ellipsometry results of GQDs/PEDOT:PSS (Aldrich 483095) films based on BEMA model	80
Table 5.5 Ellipsometry results of GQDs/PEDOT:PSS (AI 4083) films based on Drude model.....	84

Publications

- (1) "Advanced optical characterization of PEDOT:PSS by combining spectroscopic ellipsometry and Raman scattering." **Minghua Kong** et al. In preparation (2022).
- (2) "Optical properties and thermal conductivity of graphene quantum dots/PEDOT:PSS hybrid thin films." **Minghua Kong** et al. In preparation (2022).
- (3) "A detailed study of tuning thermal conductivity of PEDOT: PSS thin films." **Minghua Kong** et al. In preparation (2022).
- (4) "Effect of vacuum annealing on the properties of one step thermally evaporated Sb_2S_3 thin films for photovoltaic applications." E. Gnenna, N. Khemiri, **M. Kong**, M. I. Alonso and M. Kanzari. European Physical Journal - Applied Physics 96(2): 20301 (2021). DOI: <https://doi.org/10.1051/epjap/2021210101>
- (5) "Influence of Nb-doping on the local structure and thermoelectric properties of transparent TiO_2 : Nb thin films." J.M. Ribeiro, F.C. Correia, A. Kuzmin, I. Jonane, **M. Kong**, A.R. Goñi, J.S. Reparaz, A. Kalinko, E. Welter, C.J. Tavares. Journal of Alloys and Compounds 838 (2020). DOI: <https://doi.org/10.1016/j.jallcom.2020.155561>.

Conference Presentations

- (1) "A detailed study of the optical properties of GQDs/PEDOT:PSS hybrid thin films." **Minghua Kong**, Miquel Garriga, Juan Sebastián Reparaz, Maria Isabel Alonso. 9th International Conference on Spectroscopic Ellipsometry (ICSE), Online, 2022.
- (2) "Optical and thermoelectric properties of ZnO/PEDOT:PSS hybrid thin films." **Minghua Kong**, Mariano Campoy-Quiles, Maria Isabel Alonso, and Juan Sebastián Reparaz. 2021 Spring Meeting of the European Materials Research Society (E-MRS), Online, 2021.
- (3) "A detailed study of the optical and thermoelectric properties of PEDOT:PSS thin films." **Minghua Kong**, Luis Alberto Pérez, Osnat Zapata, Mariano Campoy-Quiles, Agustín Mihi, Juan Sebastián Reparaz, and Maria Isabel Alonso. 8th ICSE, Barcelona (Spain), 2019.

Acknowledgements

Firstly, I am extremely grateful to Maria Isabel Alonso and Juan Sebastián Reparaz for their supervision during my PhD. I would like to thank them for their patience. Isabel always gave me timely and powerful help whenever I wanted to discuss something. Isabel, you are the woman scientist that I want to be. Sebas, thank you for giving me the chance to work with you. I sincerely appreciate all your guidance and help during my PhD study. Dear Isabel and Sebas, no matter where I am, I wish you health and all the best! Keep in touch.

Secondly, I gratefully acknowledge the financial support from China Scholarship Council. Thirdly, I would like to express my gratitude to Miquel Garriga for his great help in spectroscopic ellipsometry. I'd also like to take this opportunity to thank Mariano Campoy Quiles for all his suggestions for my research. I want to thank Agustín Mihi for his help in FTIR measurements and for giving me the chance to learn nanoimprint lithography. I also thank Alejandro Goñi for answering my questions about Raman spectroscopy.

Special thanks to Bernhard Döring for correcting some contents of this thesis on his paternity leave, and for all his help during my PhD. I sincerely thank Osnat Zapata Arteaga: he shared his fabrication experience with me without any reservation.

Thanks to dear señorita, Denise Estrada, who always encouraged me. To my best friend, Yanfang Dong. We shared our life regularly and gave mental support to each other.

Thanks to all the friendly guys in NANOPTO group, Pau Molet, Aleksandr Perevedentsev, Luis Alberto Pérez, Leonardo Scarabelli, Jose Mendoza, Ylli Conti, Eulalia Pujades, Martí Gibert, José Jurado, Albert Harillo, Miquel Casademont, Ivan Álvarez, Adrián Francisco, Xavier Rodriguez, Enrique Pascual...

I would like to thank my Chinese friends in ICMAB and ICN2, Kai Xu, Jinhui Hu, Wenhai Wang, Suhong Zhang, Yajie Zhang, Ying Liu, Peng Xiao, Jinghai Li et al. We spent our holidays and celebrated Chinese festivals together. The pleasure moments with all of you are memorable.

Finally, I want to say sorry to my parents. As your only child, I regret that I could not accompany you in the important Chinese festivals these years. Happily, we will all meet soon.